

A Carbon Molecular Sieve-based Catalyst with Encapsulated Ruthenium  
Nanoparticles for Bio-oil Stabilization and Upgrading

By

Copyright 2012

Alexander Mironenko

Submitted to the graduate degree program in Chemical Engineering and the Graduate Faculty of  
the University of Kansas in partial fulfillment of the requirements for the degree of Master of  
Science.

---

Chairperson Dr. Bala Subramaniam

---

Dr. R.V. Chaudhari, Committee Member

---

Dr. Shenqiang Ren, Committee Member

Date Defended: 06/06/2012

The Thesis Committee for Alexander Mironenko

certifies that this is the approved version of the following thesis:

A Carbon Molecular Sieve-based Catalyst with Encapsulated Ruthenium  
Nanoparticles for Bio-oil Stabilization and Upgrading

---

Chairperson Dr. Bala Subramaniam

Date Approved: 06/11/2012

## ABSTRACT

Pyrolysis oil derived from biomass (bio-oil) is regarded as a potential substitute for petroleum crude for producing environmentally friendly fuels of the future. However, pyrolysis oil upgrading still remains an issue due to its complex composition, low stability, high oxygen and water contents, and low hydrogen-to-carbon ratio. Although hydrogenation was proposed as a promising technology to improve properties of pyrolysis oil, attempts to synthesize a selective and active hydrogenation catalyst have so far been unsuccessful. A major challenge is in obtaining bio-oils with stable composition that can be processed further to fuels in biorefineries.

This work proposes a novel design for bio-oil stabilization catalyst with molecular sieve properties. This material consists of ruthenium nanoparticles encapsulated in an ultramicroporous carbon framework much like “berries-in-a-muffin”. The hypothesis is that the most reactive bio-oil molecules (aldehydes and ketones below 5 Å that cause oligomerization) will be able to enter the pores and be hydrogenated by the ruthenium catalyst to non-reactive molecules, while other bio-oil components will not be able to access the pores and participate in chemical reactions on active sites. The stabilized bio-oil would then be ready for further hydroprocessing to produce fuels.

Multistep synthesis of a carbon molecular sieve containing ruthenium nanoparticles was successfully accomplished. Transmission electron microscopy revealed that metal nanoparticles are less than 3 nm in diameter and uniformly distributed within catalyst pellets. Carbon dioxide adsorption at 273 K coupled with nitrogen adsorption at 77 K indicated that carbon porous structure is made up of ultramicropores with the total pore volume of 0.18 cm<sup>3</sup>/g and surface area of 646 m<sup>2</sup>/g. 75% of the pore volume consists of pores less than 8 Å. Adsorption of probe molecules measured by means of a tapered element oscillating microbalance (TEOM) confirmed that the catalyst possesses molecular sieve properties acting as a 5Å-molecular sieve. Slit-like pores of the carbon framework are accessible to bio-oil model compounds with minimum dimensions of 3.4-4.1 Å, such as furfural, acetaldehyde, acetone, and anisole. Water molecules as well as molecules of cyclohexanone and tetrahydrofuran (minimum dimension of 5.3 Å) are unable to adsorb on catalyst pores effectively. Estimated polarizabilities of model compounds confirm that the observed adsorption behavior is explained solely by the molecular sieve effect and does not follow from differences in interaction of the probe molecules with the carbon support. The observed catalyst pore cutoff size of 5 Å is shown to correspond to an estimated molecular size distribution in corn cob-derived bio-oil, allowing desired molecular size selectivity.

This work suggests potential applications of a developed molecular sieve-based catalytic system including selective hydrogenation of light aldehydes and ketones involved in bio-oil stability issue, and selective reforming of low molecular weight oxygenates in bio-oil yielding *in situ* hydrogen.

## ACKNOWLEDGEMENTS

To my research advisor, Dr. Bala Subramaniam, for his encouragement, support, and guidance in developing research ideas;

To thesis committee members, Dr. R.V. Chaudhari and Dr. Shenqiang Ren, for their valuable feedback and pieces of advice;

To Dr. Anand Ramanathan, Dr. Juan Bravo, Dr. Kirk Snively, Dr. Swarup Maiti, Dr. Haijun Wan for priceless learning experience;

To CEBC students and colleagues Meng Li, Arely Torres, Xin Jin, Madhav Ghanta, Zhuanzhuan Xie, Qing Pan, Wenjuan Yan for their support and wonderful moments;

To Claudia Bode for encouragement and help with poster and presentation design;

To Dr. Darryl Fahey for his feedback on presentations and speeches;

To Jim Bosse for tremendous help with thesis and poster figures;

To Alan Walker for technical help;

To Dr. David Moore and Dr. Prem Thapa for performing TEM analyses;

To my parents for their love and support;

To U.S. Department of State for the Fulbright Scholarship that made this work possible

## TABLE OF CONTENTS

<b>Abstract</b>	iii
<b>Acknowledgements</b>	iv
<b>Table of Contents</b>	v
<b>List of Tables</b>	viii
<b>List of Figures</b>	ix
<b>List of Notations</b>	xi
<b>Chapter 1 Literature Survey and Catalyst Concept Development</b>	1
1.1 Introduction	1
1.2 Small Molecules of Oxygenates and Their Role in Bio-Oil Upgrading/Instability	3
1.3 Concept of a Molecular Sieve-based Catalyst	4
1.4 Choice of a Molecular Sieve. Carbon Molecular Sieves vs. Zeolites	6
1.5 Molecular Size Distribution in Bio-oil	7
1.6 Carbon Molecular Sieves	10
1.7 Ruthenium as a Metal Catalyzing Hydrogenation of Carbonyl Compounds	14
1.8 Objectives of this work	15
<b>Chapter 2 Methods of Catalyst Synthesis and Characterization</b>	16
2.1 Catalyst Preparation Procedure	17
2.1.1 Ruthenium Precursor and Reduction Procedure	17
2.1.2 Initial Polymerization and Cross-linking of Furfuryl Alcohol	19
2.1.3 Carbonization of the Polymer Composite	20
2.2 Methods of Catalyst Characterization	21
2.2.1 Transmission Electron Microscopy	21

2.2.2 N <sub>2</sub> and CO <sub>2</sub> Sorption	22
2.2.3 Temperature-Programmed Reduction (TPR) and Chemisorption	23
2.2.4 Preliminary Hydrogenation Experiments	24
2.2.5 Tapered Element Oscillating Microbalance (TEOM)	25
<b>Chapter 3 Synthesis and Characterization of the First Generation of the Catalyst</b>	<b>28</b>
3.1 Synthesis of Plain CMS	28
3.2 Synthesis of CMS with Encapsulated Ruthenium Nanoparticles	31
3.3 Characterization of Catalyst Structure	34
3.4 Preliminary Hydrogenation Studies	37
3.5 Catalyst Modification by means of Thermal Treatment at 1000°C	41
<b>Chapter 4 Synthesis and Characterization of the Second Generation of the Catalyst</b>	<b>45</b>
4.1 Synthesis of the Second Generation Catalyst	45
4.2 Characterization of Catalyst Structure	46
4.3 Testing Molecular Sieve Effect	55
4.3.1 Choice of Probe Molecules	55
4.3.2 Choice of Adsorption Temperature	57
4.3.3 Setting and Determination of Adsorbate Concentrations	57
4.3.4 Procedure of Analysis	63
4.3.5 Data Analysis	66
4.4 Determination of ruthenium content in RuCMS800-2 catalyst	74
4.5 Chemisorption Measurements	74
4.6 Brief Remarks About the Third Generation of the Catalyst	83

<b>Chapter 5 Conclusions and Path Forward</b>	81
<b>References</b>	86
<b>Appendix A</b>	90
<b>Appendix B</b>	97
<b>Appendix C</b>	97
<b>Appendix D</b>	99
<b>Appendix E</b>	103
<b>Appendix F</b>	104
<b>Appendix G</b>	106
<b>Appendix H</b>	112
<b>Appendix I</b>	113

## LIST OF TABLES

Table 1-1: Estimated molecular size distribution in corn cob-derived bio-oil	11
Table 3-1: Pore structure characteristics of plain CMS	30
Table 3-2: Characteristics of pore structure of RuCMS800-1	35
Table 4-1: Characteristics of pore structure of RuCMS800-2	50
Table 4-2: Characteristics of pore structure of RuCMS1000-2	53
Table 4-3: Model compounds chosen for testing molecular sieve effect	56
Table 4-4: Conditions in the saturator with respect to model compounds used	58
Table 4-5: Properties of adsorbates and calculated micropore liquid densities (Dubinin's approach)	69
Table 4-6: Densities calculated from PRSV model versus densities estimated on the basis of Dubinin's approach	69
Table 4-7: Polarizabilities, minimal dimensions, and adsorption capacities for various probe molecules	72
Table 4-8: Chemisorption results	76



## LIST OF FIGURES

Figure 2-1: Reduction of ruthenium acetylacetonate (III) by furfuryl alcohol	18
Figure 2-2 : TEOM scheme	26
Figure 3-1: Pore size distribution (PSD) of plain CMS materials (without Ru incorporation)	29
Figure 3-2: Temperature program for the cross-linking stage	32
Figure 3-3: Temperature program for additional thermal treatment	33
Figure 3-4: Temperature program for the carbonization step	33
Figure 3-5: N <sub>2</sub> pore size distribution of RuCMS800-1	34
Figure 3-6: TEM micrograph of RuCMS800-1	36
Figure 3-7: Temperature-programmed reduction (TPR) profile for RuCMS800-1	37
Figure 3-8: Pressure profiles for hydrogenation in a batch reactor	39
Figure 3-9: N <sub>2</sub> pore size distributions for RuCMS800-1 and RuCMS1000-1	42
Figure 4-1: Comparison of pore size distributions of RuCMS800-1 and RuCMS800-2	46
Figure 4-2: Comparison of pore size distributions of RuCMS800-2 and RuCMS1000-2	47
Figure 4-3: TEM micrographs of RuCMS800-2	48
Figure 4-4: Pore size distribution of RuCMS800-2	50
Figure 4-5: N <sub>2</sub> adsorption isotherm for RuCMS800-2	51
Figure 4-6: CO <sub>2</sub> adsorption isotherm for RuCMS800-2	51
Figure 4-7: CO <sub>2</sub> pore size distribution of RuCMS800-2 obtained using GCMC method	52
Figure 4-8: Pore size distribution of RuCMS1000-2	53
Figure 4-9. CO <sub>2</sub> adsorption-desorption isotherms for RuCMS1000-2	54
Figure 4-10: Flow dilution scheme	59

Figure 4-11: Algorithm for setting and calculation of adsorbate concentrations	60
Figure 4-12: Adsorption isotherms for RuCMS800-2	66
Figure 4-13: Adsorption isotherms for RuCMS1000-2	67
Figure 4-14: Adsorption isotherms for RuCMS800-2 (volume units)	70
Figure 4-15: Adsorption isotherms for RuCMS1000-2 (volume units)	71
Figure 4-16: Pore size distribution of RuCMS900-3	80
Figure C-1: Acetic acid calibration plot	97
Figure C-2: Chromatogram of products of acetic acid hydrogenation on RuCMS800-1 catalyst	98
Figure E-1: Example of TEOM raw data obtained for sorption of acetaldehyde on RuCMS800-2 at concentrations 1-24.4 vol. %	103
Figure E-2: Example of TEOM raw data obtained for sorption of acetaldehyde on quartz at concentrations 1-24.4 vol. %	104

## LIST OF NOTATIONS

### Chemisorption

$A_m$  – ruthenium surface area observed by H<sub>2</sub> chemisorption, m<sup>2</sup>/g

$V_m$  – gas adsorbed at monolayer, moles/g

$N_A$  – Avogadro number

$(H/Ru)$  – H:Ru ratio assumed to be unity

$d_s$  – ruthenium surface density, 16.31 metal atoms per nm<sup>2</sup>

$MD$  – ruthenium dispersion, %

$A_w$  – ruthenium atomic weight equal to 101.070 g/mol

$W\%$  - ruthenium percentage in the sample

$D_a$  – average ruthenium particle diameter, nm

$F$  – shape factor

$d_m$  – ruthenium density equal to 12.2 g/cm<sup>3</sup>

## TEOM

$\Delta m$  – TEOM mass change, g

$K$  – spring constant of the tapered element

$f_0$  – the natural oscillating frequency at time “0”

$f_1$  – the natural oscillating frequency at time “1”

$F_{total}^d$  – desired total TEOM inlet flow, cc/min

$T_{sat}^0$  – temperature of liquid in a saturator at the beginning of the experiment, °C

$P_{sat}^0$  – vapor pressure of a compound inside saturator at the beginning of the experiment, kPa

$C_{TEOM}^d$  – desired concentration of a compound in TEOM, mol. %

$F_c^d$  – desired flow rate of a pure compound in a saturator outlet flow, cc/min

$F_{He,total}^d$  – desired total flow rate of Helium, cc/min

$F_{s-out}^d$  – desired saturator outlet flow rate, cc/min

$F_{s-in}^d$  – desired saturator inlet flow rate, cc/min

$F_{dil}^d$  – desired diluent flow rate, cc/min

$F_{s-in}^s$  – set saturator inlet flow rate, cc/min

$F_{dil}^s$  – set diluent flow rate, cc/min

$T_{sat}^a$  – actual temperature of a liquid inside saturator, °C

$P_{sat}^a$  – actual vapor pressure of a compound inside saturator, kPa

$C_{sat}^a$  – actual concentration of a compound in a vapor phase inside the saturator, mol. %

$F_c^a$  – Actual flow rate of a pure compound in a saturator outlet flow, cc/min

$F_{total}^a$  – Total actual TEOM inlet flow rate, cc/min

$C_{TEOM}^a$  – actual calculated concentration of a compound in gas phase in TEOM, %

$T_{sat}^{i+1}$  – temperature of liquid inside a saturator at the end of a single TEOM measurement, °C

$P_{sat}^{i+1}$  – vapor pressure of a compound inside saturator at the end of a single TEOM measurement, kPa

$F_{s-in}^{s,i}$  – set saturator inlet flow rate at the beginning of a single TEOM measurement, cc/min

$F_{dil}^{s,i}$  – set dilutant flow rate at the beginning of a single TEOM measurement, cc/min

$F_{s-in}^{d,i}$  – desired saturator inlet flow rate at the beginning of a single TEOM measurement, cc/min

$F_{dil}^{d,i}$  – desired dilutant flow rate at the beginning of a single TEOM measurement, cc/min

$P_{sat}^i$  – vapor pressure of a compound inside saturator at the beginning of a single TEOM measurement, kPa

$T_{sat}^i$  – temperature of liquid inside a saturator at the beginning of a single TEOM measurement, °C

## Density calculations for TEOM

$T_{cp}$  – critical temperature of adsorbate, °C

$T_{bp}$  – boiling point of adsorbate, °C

$P_{cp}$  – critical pressure of adsorbate, kPa

$\rho_D$  – density of adsorbate inside the pores in an adsorbed state, kg/m<sup>3</sup>

$\rho_{bp}$  – density of liquid adsorbate at boiling point, kg/m<sup>3</sup>

$\rho_{cp}$  – critical density of adsorbate, kg/m<sup>3</sup>

$T_{TEOM}$  – adsorption temperature, °C

$M$  – molar weight of adsorbate, kg/mol

## Chapter 1. Literature Survey and Catalyst Concept Development

### 1.1.Introduction

In the 21<sup>st</sup> century the world faces serious energy challenge. Petroleum supply is expected to decrease due to depletion of non-renewable oil reserves. On the other hand, oil demand on burgeoning markets of BRIC countries is growing rapidly [1]. Increasing discrepancy between oil supply and demand is becoming a driving force for diversification of the feedstock base for fuel production, manifested by an upward trend in the use of renewable feedstock [2].

The only renewable source of hydrocarbons known to humanity is biomass [3]. Biomass is referred to as a biological material from living, or recently living, organisms. In fact, biomass is solar energy consumed by plants throughout their lifetime and stored in organic matter. Since solar light beam will be unaltered in the next one billion year [4], biomass is regarded as a promising energy source that can be potentially converted into conventional fuels.

Biomass derived from plants involves a variety of classes of compounds, including carbohydrates, gums, resins, terpenes, terpenoids, waxes, etc. Among all biomass constituents, two species are the most abundant and regarded as primary energy holders: cellulose and lignin [5]. Both compounds are highly cross-linked solid polymers of low density that need to be broken apart for subsequent fuel production.

Three groups of processes have been proposed to cleave large molecules of cellulose and lignin and convert them into fuels. The first group includes various modifications of a gasification process to transform biomass into a mixture of carbon monoxide and hydrogen, followed by synthesis of hydrocarbons in Fisher-Tropsch process. Despite apparent product

flexibility, gasification requires high temperatures and yields large amounts of tar [6]. As an alternative, enzymatic hydrolysis can be used to break apart cellulose molecules to monosaccharides followed by their fermentation to ethanol. The third group of processes involves biomass pyrolysis yielding so-called bio-oil with high yield – up to 78 wt. % [7]. The main advantage of biomass pyrolysis is that, in contrast to multistep processes of gasification and fermentation, it allows production of a liquid product with relatively high energy density (more than 20 times higher than energy density of biomass) [8] in one step without any use of an expensive catalyst. Pyrolysis bio-oil is regarded as a potential substitute for petroleum crude in conventional oil refineries [5].

Bio-oil produced by means of biomass pyrolysis primarily consists of oxygen-containing species [7]: water; low-molecular carboxylic acids, such as acetic acid; aldehydes, such as hydroxyacetaldehyde; ketones; furan-derived compounds; aromatics such as guaiacol derivatives, etc. High-molecular species are also present: they include carbohydrates (levoglucosan) and pyrolytic lignin. The complex nature of pyrolysis oil makes it thermodynamically unstable [9]. More hydrophobic compounds, such as pyrolytic lignin, tend to form separate phases even after minor alteration of solution properties [10]. Reactive low molecular weight oxygenates – aldehydes and ketones – are prone to oligomerization, resulting in increase in oil viscosity during storage [11]. <sup>13</sup>C NMR spectroscopy indicates that bio-oil contains significant amounts of aromatic carbon, constituting 30-50 wt. % of total carbon [12]. High bio-oil aromaticity manifests itself in the low H:C ratio compared to that of petroleum (1.3-1.5 [13] versus 1.4-2.0 [14]), leading to high coke yields in hydrotreatment and catalytic cracking processes [15].

Several methods have been proposed to improve bio-oil stability and make it more suitable for conventional processes of fuel production. Addition of up to 10 wt. % of methanol to bio-oil



is known to inhibit chemical reactions involved in the aging process [9]. Bio-oil hydrogenation is regarded as a promising technology for pyrolysis oil stabilization and upgrading [9]. However, attempts to develop an active and selective catalyst have been unsuccessful due to rapid catalyst deactivation, extremely high coke yield (8-21 wt.%) and large hydrogen consumption [16]. The majority of research in this area has been focused on designing a catalyst which would account for differences in reaction pathways of pyrolysis oil species. This work exploits a completely different approach by taking into account dissimilarities in molecular sizes of bio-oil components.

## **1.2. Small Molecules of Oxygenates and Their Role in Bio-Oil Upgrading/Instability**

Our novel concept in developing an effective catalyst for bio-oil stabilization and upgrading is based on an observation that “small” oxygenate molecules in bio-oil have significant effects in biooil aging and upgrading processes.

Specifically, it has been recently shown that small oxygenates (low molecular weight aldehydes, and ketones) are involved in chemical reactions that lead to bio-oil instability. The studies found [17] that the content of aldehydes and ketones in bio-oil decreased from 11.28% to 9.32 % after 10 weeks of storage, and the content of low molecular weight aromatic derivatives of lignin was reduced from 6.24 to 4.20%. Meanwhile, the amounts of phenolic hydroxyl and methoxyl groups in pyrolytic lignin fraction decreased from 11.2 wt% (control) to 8.0 wt% (10 weeks) and 11.9 wt. % (control) to 8.6 wt. % (10 weeks), respectively, suggesting their involvement in chemical reactions. After 10 weeks, the average molecular weight of pyrolytic lignin also increased from 872 to 1161 g/mol, and its yield increased from 13.2 to 24.3%. Based on these numbers, the researchers concluded that low molecular weight oxygenates were being

consumed in oligomerization reactions with pyrolytic lignin upon storage. Therefore, low molecular weight aldehydes and ketones are primary participants in bio-oil instability mechanism.

Regarding bio-oil upgrading in hydrodeoxygenation process, we note that the role of light oxygenates is also unique. In contrast to majority of middle molecular weight O-containing compounds, which are being transformed to liquid hydrocarbons and coke upon hydrodeoxygenation, light oxygenates does not yield liquid products suitable as transportation fuels. For example, complete deoxygenation of hydroxyacetaldehyde ( $\text{HOCH}_2\text{CHO}$ ) and hydroxyacetone ( $\text{HOCH}_2\text{C}(\text{O})\text{CH}_3$ ), known to be abundant components of bio-oil [7], will result in formation of gases, ethane and propane, respectively. Therefore, the hydrodeoxygenation of hydroxyacetaldehyde, hydroxyacetone, and similar molecules does not result in liquid fuel production, unless reactants are polymerized in a prior step. Thus, alternative conversion route for low molecular weight compounds must be utilized in order to prevent excessive formation of low value gases.

In order to take into account special roles of low molecular weight compounds in bio-oil aging and upgrading, we believe that a catalyst must be developed such that it distinguishes between molecules of bio-oil based not only on their reactivity, but also on their size. In other words, the catalyst must be able to selectively convert small molecules versus bigger molecules.

### **1.3. Concept of a Molecular Sieve-Based Catalyst**

We believe that molecular size selectivity can be achieved by using a molecular sieve as a part of the catalyst. We hypothesize that if a molecular sieve is placed between a mixture of bio-oil components and an active site, molecular separation can be implemented before reactants reach a metallic site of a catalyst and adsorb on it. Given an appropriate size of the pores of a

molecular sieve, small molecules of aldehydes and ketones will be able to enter the pores, reach catalytic sites and be transformed, whereas bigger molecules will not fit into the pores of the sieve.

Targeting molecules of a particular size in bio-oil can be beneficial in both improving bio-oil stability characteristics and introducing an alternative route for conversion of low molecular weight compounds in hydrodeoxygenation process.

To solve the bio-oil instability issue, we propose hydrogenation of small molecular weight aldehydes and ketones that will remove carbonyl compounds involved in oligomerization reactions inhibiting bio-oil aging process. Besides removal of reactive compounds, selective hydrogenation of aldehydes and ketones will also yield alcohols known to improve bio-oil stability characteristics [9]. The use of a molecular sieve will prevent hydrogenation of molecules bigger than the pore size, and therefore avoid unwanted hydrogen consumption.

As an alternative route to convert light oxygenates into valuable products, we propose their reforming that would yield either syngas – a mixture of carbon monoxide and hydrogen – or pure hydrogen. According to reported calculations [18], in reforming of certain oxygenates, such as methanol, ethanol, acetone, and hydroxyacetaldehyde, equilibrium yield of hydrogen at 750 °C is 85.2 – 87.1%. If the water-gas-shift reaction is taken into account, hydrogen yield can be as high as 97.5%. Moreover, experimental studies suggest that high temperatures are not required for reforming reactions to occur with high conversion. Reforming of ethanol, hydroxyacetaldehyde, acetol, and several other O-containing compounds showed complete conversion of the feedstock even at 400°C on the Ni/Al<sub>2</sub>O<sub>3</sub> catalyst [18]. In the case of hydroxyacetaldehyde, the hydrogen yield exceeded 80% at 350°C and no coke formation occurred. Another examples of light oxygenates yielding hydrogen in reforming include glycerol [19] (at 350°C complete conversion

to syngas on Pt/SiO<sub>2</sub> with no catalyst deactivation during 40 h run), acetic acid [20] (at 400°C complete conversion on Ni/Al<sub>2</sub>O<sub>3</sub> with 90% selectivity to hydrogen), and 1,2-propanediol [21].

It is important to note that in both hydrogenation and reforming of bio-oil, the use of a molecular sieve will prevent access of pyrolytic lignin and sugars to active metallic sites. Sugars and pyrolytic lignin are known as coke precursors; for example, guaiacol, a monomer of pyrolytic lignin, is known to form coke on noble metal catalysts and deactivate them in the hydrodeoxygenation process at temperatures as low as 100°C [22]. Also, due to the high aromaticity of pyrolytic lignin, it can become a “hydrogen scavenger” in deoxygenation process, since it is known that reduction of aromatic rings require enormous amounts of hydrogen. We believe that the use of a molecular sieve in a catalyst design will help avoid the disadvantages associated with pyrolytic lignin, making the overall bio-oil upgrading process more effective.

#### **1.4. Choice of a Molecular Sieve. Carbon Molecular Sieves vs. Zeolites**

To design a molecular sieve-based catalyst effective in selective hydrogenation/reforming of light oxygenates in bio-oil, optimum cutoff size of pores as well as their shape must be considered. It is evident that the optimum pore size will be determined by the molecular size distribution in the bio-oil containing various classes of compounds. At the same time, the choice of a material for the molecular sieve will dictate the range of possible pore sizes and shapes. There are two widely used options for molecular sieves – zeolites and carbon molecular sieves.

Although zeolites have been used extensively in research on bio-oil upgrading and are considered promising catalysts, they contain strong acidic sites that are known to initiate polymerization of unsaturated compounds leading to coke formation [23]. As an example, for acetaldehyde, acetone, butanone, and acetic acid upgraded over HZSM-5 at 400°C, significant

amounts of coke formed on the catalyst after 4-6 hours on stream. Coke content in the catalyst was 1.75-4.74%, which resulted in decrease of catalyst activity [24]. Upgrading of bio-oil at 450°C also resulted in formation of coke with the yield of 18.1% [25].

As opposed to zeolites, carbon supports, including carbon molecular sieves, do not contain strong acidic sites, and therefore they initiate coking reactions to a much lesser extent. Hence the coke yield is lower when carbon is used as a support for a noble metal-containing catalyst [26]. Moreover, carbon is much more stable in aqueous environment than zeolite. Therefore, we believe that carbon is a better material to develop a molecular sieve in terms of both coke minimization as well as stability.

### **1.5. Molecular Size Distribution in Bio-Oil**

Knowledge of the molecular size distribution in bio-oil is essential to determine the pore size of the molecular sieve required to allow separation between low molecular weight aldehydes and ketones versus the rest of bio-oil. To estimate molecular size distribution, the bio-oil composition must be known along with characteristic sizes of molecules. It is important to note that the characteristic size of a particular compound determining its accessibility through the pores of a molecular sieve to the imbedded catalyst sites is dependent on the shape of the pores. For zeolites, pores have a cylindrical or ring-like shape [27] and therefore the characteristic size of molecules is a diameter. For carbon molecular sieves, pores have a slit-like shape, and the characteristic size is a minimum dimension of a molecule [28].

For calculations of a molecular size distribution, we used published data [7] on the content of 80 components identified in corn cob bio-oil by means of gas chromatography. The complete list of compounds can be found in Appendix A.

Since it is an apparently tedious procedure to calculate minimum dimensions for all 80 compounds, we used heuristic approach for estimations of molecular sizes. Based on the sparse data on molecular sizes available in literature [29], we assume that in molecules containing methyl groups and/or unbranched alkyl groups, the minimum dimension is determined by thickness of that group equal to 4.0 Å. Assuming that the presence of the alkyl group is a key factor determining minimum dimension of simple molecules, we assigned each of 80 compounds to one of the following groups:

- A. Molecules with conjugated double bonds without methyl functional groups ( $\pi$ -electron system);
- B. Molecules containing methyl/alkyl groups, as well as -CH<sub>2</sub>- groups;
- C. Sugars

Minimum dimension of group A molecules was determined by thickness of  $\pi$ -electron system (as in furfural, phenol, and hydroquinone) and was assumed to be equal to minimum size of benzene molecule – 3.3 Å. For group B molecules thickness was set to 4.0 Å – the thickness of methyl group. Corresponding size assignments can be found in Appendix A.

It is important to note that this induction-based method of molecular size estimates is not very accurate since molecular sizes are also dependent on steric limitations within a molecule, interactions between functional groups, and bond lengths. Nevertheless, for our purposes, this is not a serious limitation since we consider molecules in only three size groups: less than 4 Å, 4-5 Å, and greater than 5 Å. Molecules from Group A occur in the group “less than 4Å”, and the group B molecules occur in the group “4-5 Å”. Molecules in the group “greater than 5 Å” include sugars (due to their complex cyclic structure), unidentified compounds (explained in the next paragraph), pyrolytic lignin, and water. Explanation for inclusion of the last three items will be given below.

The group of unidentified compounds is likely to contain non-volatile (the boiling point of acetosyringone – one of the heaviest compounds identified in bio-oil – is well above 340 °C), high molecular weight, and hence high molecular size molecules. Despite this, there is still a probability that some unidentified molecules such as polycyclic aromatic hydrocarbons (PAH) could have minimum dimension below 5 Å. However, the PAH content in bio-oil is typically low [30]. In addition, PAHs and other high molecular weight compounds are likely to have high polarizability that will result in strong interaction between such molecules and the non-polar surface of the carbon molecular sieve [27]. Such a strong interaction will cause a “sieving effect” based on differences in effective diffusivities rather than in shape. Based on this reasoning and also due to lack of information on the nature of unidentified compounds, we assigned all of the unidentified molecules to the size group “greater than 5 Å”.

Regarding the pyrolytic lignin fraction, it is known from SANS studies that its molecules have an average size of 13-15 Å at least for sawdust-derived bio-oil [31], and therefore the fraction was also assigned to the size group “greater than 5 Å”.

Assignment of water to the group “greater than 5 Å” was based on the fact that adsorption of water on carbon micropores is very low at concentrations up to 40 mol. % in a vapor phase due to so-called cluster-mediated micropore filling [32].

Calculated size distribution of identified components in corn cob bio-oil is presented in the Table 1-1.

Based on the molecular size distribution, we can conclude that in order to distinguish between low molecular weight oxygenates – aldehydes, ketones, and aromatics – on one hand, and pyrolytic lignin and sugars on the other hand, a carbon molecular sieve must have a cut-off pore size of 5 Å. It is important to note that at this point it is unclear what optimum size of CMS pores is, and it is possible that catalyst with 7 Å pores will be effective as well. Despite this

ambiguity, we made a decision to synthesize the catalyst with cutoff pore size of 5 Å, mainly due to the fact that 5 Å pore cutoff size can be easily tested in gas phase adsorption experiments without use of complex high molecular weight compounds.

Since low molecular weight aldehydes and ketones (in contrast to pyrolytic lignin, sugars, and water molecules), will be able to easily access the 5 Å pores, we expect hydrogenation/reforming of those carbonyl compounds to be very effective, and also that the catalyst deactivation will be inhibited.

## **1.6. Carbon Molecular Sieves**

Carbon molecular sieves (CMS) are referred to as carbon-based materials that have an ability to separate molecules on the basis of their size and shape. In contrast to zeolites – the more commonly used molecular sieves – carbon-based molecular sieves have highly disordered structure consisting of graphitic carbon microdomains embedded into amorphous carbon. Such structural disorder gives rise to porosity and microporosity, resulting in molecular sieve properties of the material. As opposed to zeolites, long range ordering in CMS is disadvantageous, since ultramicroporosity decreases as structure becomes more uniform [28].



Table 1-1: Estimated molecular size distribution in corn cob-derived bio-oil

Group of components	Content in bio-oil, wt. % on wet basis
<b>&lt; 4 Å</b>	
Furaldehydes	0.7
phenol, vinylphenol, hydroquinone, hydroxybenzaldehyde	2.2
<b>Total &lt;4 Å</b>	<b>2.9</b>
<b>4-5 Å</b>	
Acids	6.2
aldehydes and ketones	12.0
guaiacols, phenols, and syringols	3.6
Furans	1.6
Pyrans	0.9
<b>Total 4-5 Å</b>	<b>24.3</b>
<b>&gt;5 Å</b>	
Sugars	2.3
Unidentified	29.9
pyrolytic lignin	8.5
Water	32.2
<b>Total &gt; 5 Å</b>	<b>72.9</b>

CMS materials are prepared by controlled pyrolysis of both synthetic and natural precursors that generate carbon in 25-50% or more mass yields on the basis of the original mass of the precursor. Synthetic precursors include a variety of polymers that decompose thermally to light gases and carbon. Although any carbon-containing material can be used to obtain carbon, not all organic substances are capable of forming a carbon molecular sieve with desired structure and yield. In order to preserve the chaotic structure of the carbon material from “collapsing” into graphitic structure, high degree of cross-linking must occur between molecules of a precursor upon thermal treatment. Thus, cross-linking will stabilize low temperature features of the resulting char, resulting in relatively high ultramicroporosity and stability.

Cross-linking occurs in so-called “non-graphitizing” polymers and is enhanced by the presence of heteroatoms and the excess of hydrogen in polymer. Examples of precursors with such characteristics include polyacrylonitrile (PAN) which generates HCN as a side-product and pyrolyzed polyacrylonitrile (PPAN) upon thermal treatment, polyvinylidene chloride (PVDC) which produces HCl and pyrolyzed PVDC (PPVDC), and polyfurfuryl alcohol (PFA) which leads to pyrolyzed PFA (PPFA) as well as carbon dioxide, water, and methane in various yields depending upon the conditions employed.

CMS materials possess microporosity of 5-10 Å size range, which may vary significantly with a precursor used and preparation conditions employed. When polyfurfuryl alcohol is used as a precursor, the typical range of pore sizes obtained lies between 3.8 – 4.8 Å [33]. Polyacrylonitrile-derived carbon molecular sieves have pore sizes of 3.0 – 5.2 Å [34], whereas polyvinylidene chloride enables synthesis of molecular sieves with larger pores – of 6 – 8 Å [28]. Since we found that a carbon molecular sieve with a 5 Å molecular size cutoff is most suitable for the desired separation of molecules in bio-oil, we chose polyfurfuryl alcohol as a precursor to synthesize a CMS-based catalyst.

PFA is a thermosetting polymer that is derived from the acid-catalyzed condensation of furfuryl alcohol. Upon heating under inert conditions, the polymer reacts to form water, methane, carbon dioxide, carbon monoxide, and hydrogen. During thermal treatment, ample crosslinking occurs between the developing unsaturated chains. The surface areas of PFA-derived CMS vary with heat treatment, but for material prepared between 500 and 800°C, they are generally in the range of 450-500 m<sup>2</sup>/g.

In order to use a polyfurfuryl alcohol-derived molecular sieve as a hydrogenation/reforming catalyst, active metal nanoparticles must be incorporated into the carbon framework. Synthesis of such hybrid molecular sieve-catalyst systems and their selectivity in hydrogenation reactions has been reported [35-37]. Foley et al. provided data on the synthesis, characterization, and properties of novel shape-selective, thermally stable catalysts consisting of platinum nanoparticles entrapped in a carbon molecular sieve framework [38]. Alkene hydrogenation test reactions at different temperatures showed that the catalyst was particularly active for hydrogenation of molecules of small cross-section area, such as ethylene and propylene, as opposed to hydrogenation of butylene and isobutylene, which have higher cross-section diameters. Methyl chloride BET adsorption measurements revealed the presence of micropores in 0.4-0.5 nm diameter range, which were believed to provide the shape selectivity and explain the observed differences in hydrogenation activity. To further elucidate the catalyst structure, HRTEM images were obtained, showing that platinum particle size distribution is within 2-4 nm range. Such a significant difference in micropore and nanoparticle sizes ensures the platinum particles are trapped in the carbon framework and are immobile, resulting in high thermal stability of the catalyst nanoparticles against sintering. Preparation steps of characterized and tested catalyst included reduction of platinum acetylacetonate by furfuryl alcohol to form platinum nanoparticles stabilized by Triton X-100 used as a surfactant; subsequent furfuryl

alcohol polymerization with an acid catalyst (p-toluenesulfonic acid); ultrasonication followed by pyrolysis at 800° C for eight hours.

However, carbon molecular sieves have not previously been tested for biomass applications.

### **1.7. Ruthenium as a Metal Catalyzing Hydrogenation of Carbonyl Compounds**

It is known that ruthenium is the most active catalyst for hydrogenation of aliphatic carbonyl compounds particularly in presence of water [39]. In particular, it has been shown that the homogeneous ruthenium catalyst  $\text{RuCl}_2(\text{PPh}_3)_3$  is active in hydrogenation of two model compounds that constitute a significant fraction of pyrolysis oil – hydroxyacetaldehyde and acetol. Batch reactor studies under mild conditions (temperature 50-90 °C, pressure 20-40 bar) showed that the catalyst is remarkably active in hydroxyaldehyde conversion, providing conversion over 60 % after 30 min experiment run. However, under the same conditions  $\text{RuCl}_2(\text{PPh}_3)_3$  was much less active in acetol hydrogenation, resulting in only 10 % conversion after 16.5 hours. Nevertheless, as the authors suggested, higher conversion levels can be reached by implementing the reaction parameter optimization. Besides homogeneous ruthenium catalyst, a heterogeneous catalyst consisting of ruthenium supported on carbon showed activity for the hydrogenation of aldehydes in bio-oil at temperatures as low as 80°C [40]. Therefore, ruthenium-based catalyst has a potential to be utilized in pyrolysis oil stabilization process by facilitating hydrogenation of the reactive carbonyl compounds.

## 1.8. Objectives of This Work

The objective of this project is to design a CMS-based ruthenium catalyst for bio-oil upgrading. Catalyst development is aimed to achieve the following goals:

- Catalyst preparation goal. To develop a technique to prepare a carbon molecular sieve with entrapped ruthenium nanoparticles from furfuryl alcohol and ruthenium acetylacetonate (III);
- Catalyst characterization goal. To ensure that the synthesized catalyst possesses desired properties:
  - Uniformly distributed pores of the carbon support lie within ultramicropore range (5-7 Å), as established by carbon dioxide DFT adsorption method;
  - Ruthenium nanoparticles are of the size of several nanometers, based on transmission electron microscopy data;
  - Surface of metallic nanoparticles is accessible to reactants and hydrogen, based on hydrogen chemisorption data;
- Testing molecular sieve properties of the support. To measure accessibilities of catalyst micropores to model compounds of pyrolysis oil (acetaldehyde, acetone, anisole, furfural, tetrahydrofuran, cyclohexanone, water), based on adsorption isotherms obtained by tapered element oscillating microbalance (TEOM).

## Chapter 2. Methods of Catalyst Synthesis and Characterization

The preparation procedure of a carbon molecular sieve-based ruthenium catalyst was based on synthesis of a carbon molecular sieve with entrapped platinum nanoparticles published elsewhere [35]. Ruthenium acetylacetonate was used as a ruthenium precursor, and furfuryl alcohol was chosen as a reducing agent and a carbon molecular sieve (CMS) precursor. We have synthesized several portions of the catalyst modifying certain steps of the original synthesis procedure in order to make the technique more efficient and obtain a material that meets the following criteria:

1. Narrow micropore size distribution with majority of pores below 5-8 Å in size, with mesopores and macropores being virtually non-existent in the material to avoid their influence on molecular sieve properties;
2. Ruthenium nanoparticles (< 5 nm in size) are uniformly imbedded/distributed within catalyst pellets;

To elucidate the structure of the synthesized catalyst, we utilized a variety of methods. Mesoporosity of the material was investigated using N<sub>2</sub> adsorption at 77 K, and micropore size distribution (criterion #1) was deduced from CO<sub>2</sub> adsorption data. Sizes and distribution of ruthenium nanoparticles (criteria #2) were determined by means of transmission electron microscopy. Also, preliminary liquid-phase hydrogenation experiments in a batch reactor involving model compounds have been carried out. Below, we provide theoretical description and equipment-related peculiarities of synthesis steps first, followed by description of parameters and instruments used for catalyst characterization. Subsequently, we describe the preparation and characterization of each synthesized portion of the catalyst in detail.

## **2.1. Catalyst preparation procedure**

Preparation procedure of a carbon molecular sieve with encapsulated metal nanoparticles includes four crucial steps [35]: reduction of a ruthenium precursor, polymerization of polyfurfuryl alcohol (PFA), cross-linking of PFA, and carbonization of the composite. The overall schematic is shown in Appendix B.

### **2.1.1. Ruthenium Precursor and Reduction Procedure**

A class of compounds that are likely to be compatible with FA is acetylacetonates. Acetylacetonates of transition metals are known as metallic precursors in water-free syntheses [41], since their molecules carry no charge and therefore are soluble in non-aqueous, non-polar organic solvents, such as FA. Acetylacetonates can also be reduced by FA; platinum acetylacetonate was reported to yield colloidal solution of platinum nanoparticles in FA solution in presence of a surfactant in reflux mode [35]. For this reason, we chose ruthenium acetylacetonate (III) as a ruthenium precursor.

The goal of the reduction step is to obtain a colloidal solution of ruthenium nanoparticles dispersed in furfuryl alcohol (FA). During this step, the ruthenium precursor is reduced to yield metallic ruthenium nanoparticles that are prevented from coagulation by a surfactant. To avoid hydration and oxidation reactions, the reduction step was carried out in a water- and oxygen-free environment, namely, in an organic solvent under nitrogen atmosphere. Furfuryl alcohol, which is chosen as the CMS precursor (see Section 1.6), is also an excellent organic solvent. Moreover, furfuryl alcohol possesses reducing properties, and hence can act as a reductant for the ruthenium precursor as well.

Reduction of the ruthenium precursor by furfuryl alcohol in a reflux mode is likely to occur according to the following reaction:

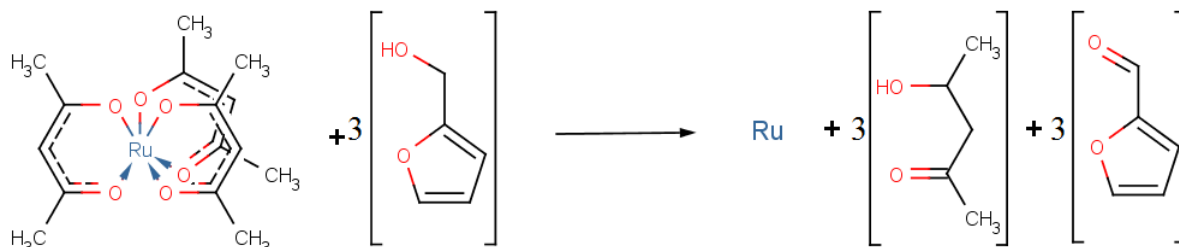


Figure 2-1: Reduction of ruthenium acetylacetonate (III) by furfuryl alcohol.

To maintain reflux mode and ensure inert atmosphere, we performed the reduction step in a 3-neck flask with a top neck connected to a condenser filled with circulating tap water. One neck was connected to a Schlenk line, and another side neck was used for a thermocouple to control temperature of a reaction mixture. The thermocouple was placed in a glass case, inserted through a bored hole in a rubber stopper and immersed into the liquid. Two manifolds of a Schlenk line were connected to a nitrogen and vacuum source, respectively. Heating of the mixture in the flask was implemented by a heating tape (0.5 x 4 ft; maximum heating power of 313 W at 120 V and 2.6 A) wrapped around the flask. The heating tape was plugged into a voltage controller to allow fine adjustment of inlet heat flow in the flask and control the temperature of the mixture. For safety reasons, the voltage controller was connected with the outlet via circuit breaker.

Precisely weighed amounts of furfuryl alcohol and ruthenium acetylacetonate (III) were loaded into the flask while stirring with a magnetic stirrer. Triton X-100, the organic surfactant, was also added to the flask to protect the ruthenium nanoparticles formed from coagulation and sedimentation. After the reactants were loaded, the flask was isolated from the atmosphere using



stopcocks in the Schlenk line, vacuumed, and pressurized with nitrogen to atmospheric pressure. To ensure an inert atmosphere, nitrogen was constantly flowed through the flask throughout the experiment, exiting the flask through the condenser. To isolate the system from atmospheric oxygen, the inlet of the nitrogen manifold of the Schlenk line and the effluent gas from the condenser were connected to bubblers filled with mineral oil.

After ensuring inert conditions in the flask, the voltage on the heating tape was set to a value sufficient to reach the boiling point of the mixture and create a reflux inside the flask. Upon completion of the preparation step, the product is a colloidal solution of ruthenium nanoparticles in FA.

### **2.1.2. Initial Polymerization and Cross-linking of Furfuryl Alcohol**

In order to transform colloidal solution of ruthenium nanoparticles to a polymer composite suitable for subsequent carbonization, FA needs to be polymerized. Polymerization of FA typically occurs in the presence of an acid catalyst soluble in non-polar organic solvents. Typically, phosphoric acid and p-toluenesulfonic acid are used as polymerization catalysts[37, 38]. However, it was reported that the use of p-toluenesulfonic acid leads to sulfur poisoning, and oxalic acid is more advantageous in terms of ensuring high activity of the catalyst [35, 42]. For this reason, we used oxalic acid as the polymerization catalyst.

After the reduction step was complete and the mixture inside the 3-neck flask was cooled to ambient temperature, oxalic acid was added to the flask to initiate polymerization of furfuryl alcohol. CMS-based ruthenium catalysts were prepared using oxalic acid in two different forms – as a saturated aqueous solution, as suggested in a published synthesis procedure [35], and as a

powder. Discussion on the most preferable form of oxalic acid is given in sections dedicated to particular syntheses below.

We carried out polymerization at room temperature for 24 hours, constantly stirring the mixture with the magnetic stirrer under nitrogen atmosphere. As we discovered in our preliminary synthesis of a plain carbon molecular sieve (see further), it is crucial not to heat the mixture at the polymerization step above ambient temperature. Polymerization at elevated temperatures leads to cross-linking of polymer and formation of a material insoluble in any solvent. As a result, the product is difficult to be retrieved from the flask. For this reason, we performed the polymerization of furfuryl alcohol in two steps. The first step was conducted in the 3-neck flask at ambient conditions to polymerize FA to the extent that the polymer product is still soluble in solvents. The second step involved complete polymerization and cross-linking of a polymer, and was performed at elevated temperatures in a tube furnace. Between two polymerization steps, the reaction mixture was dissolved in acetone, placed in a conical flask, sonicated for 1 h, and poured into evaporating dishes. Evaporating dishes were then placed inside a tube furnace (Carbolite Type 3216) with programmed temperature. Complete polymerization and cross-linking was performed with flowing nitrogen flowing through the furnace to avoid undesired oxidation of the sample by air. Synthesized polyfurfuryl alcohol-based composite was ground to less than 0.85 mm particles to be used in the carbonization stage.

### **2.1.3. Carbonization of the Polymer Composite**

The purpose of the carbonization stage is to form ultramicroporous carbon structure by thermal decomposition of poly(furfuryl alcohol). Upon heating, polyfurfuryl alcohol reacts to form low molecular weight products, such as  $\text{CO}_2$ ,  $\text{H}_2\text{O}$ , and  $\text{H}_2$ , and ample cross-linking occurs between the developing unsaturated chains [43]. Furfuryl alcohol typically undergoes thermal

decomposition in the range of temperatures of 500-1000 °C. A highly chaotic structure consisting of amorphous carbon and aromatic microdomains is formed at low temperatures of 200-500 °C, leading to a relatively large average pore size. As PFA is carbonized at higher temperatures and/or for a longer period of heat-treatment, the aromatic microdomains became larger in size accompanied by the formation of a slightly more ordered structure in the short range. As the carbonization process proceeds, aromatic microdomains continue to grow and rearrange to more ordered structures; concurrently, the size of micropores resulting from the packing of aromatic microdomains decreases [43]. Since low carbonization temperatures lead to underdeveloped pore structure and high temperatures/long soaking times cause reduction of pore size, an optimum temperature and soaking time must be chosen to form the desired ultramicroporous structure. Published data suggest that a carbon molecular sieve obtained at 800°C has maximum capacity for CO<sub>2</sub> adsorption [44]. For this reason, synthesized PFA-based ruthenium-containing composite was carbonized at 800°C. The carbonization step was carried out in a Carbolite Type 3216 tube furnace under nitrogen atmosphere.

## **2.2. Methods of Catalyst Characterization**

### **2.2.1. Transmission Electron Microscopy**

TEM micrographs were acquired using FEI TECNAI Field Emission Transmission Electron Microscope equipped with the GATEN Camera. TIA Software and ImageJ were used for data processing. Samples were prepared by grinding the catalyst to particles less than 30 µm in size and dispersing them onto a lazy carbon film supported on 300 mesh copper grids manufactured by TEDPELLA. Detailed description of transmission electron microscopy can be found elsewhere [45].

### 2.2.2. N<sub>2</sub> and CO<sub>2</sub> Sorption

Surface areas and pore size distributions were obtained via volumetric gas absorption measurements using Micromeritics Gemini unit (preliminary measurements of N<sub>2</sub> adsorption and pore size distribution by means of BJH model) and Quantachrome Instruments NOVA 2200 Multi-Station AnyGas Sorption Analyzer (Standard Model Version 11.03). Prior to the measurements with the Micromeritics instrument, samples were dried at 120°C in helium flow. Prior to measurements on the Quantachrome apparatus, samples were degassed in vacuum (<1 Torr) at 200°C.

The amounts of absorbed gases were recorded at various pressures at 77 K for nitrogen and 273 K for CO<sub>2</sub>. The resulting absorption isotherms were used to deduce pore size distributions using theoretical DFT models of pores. It has been shown that the DFT method for pore size distribution gives the most accurate results compared to classical macroscopic methods (BET, BJH, Howarth-Kawazoe), which tend to underestimate the pore size in the pore diameter range <10 nm up to 30% [46]. In the DFT method, complex mathematical modeling of gas-solid and gas-gas (gas-liquid) interactions along with geometrical considerations (pore geometry) lead to realistic density profiles for the confined fluid as a function of temperature and pressure. From these density profiles, the amount adsorbed can be derived. Gas-solid interactions are “calibrated” against real isotherm data of non-porous material. Gas-gas-liquid interactions are “calibrated” against physical property data e.g. boiling points. For pore size analysis, a “kernel” is created which consists of up to 100 theoretical, individual pore isotherms. This “shopping list” is used by the software to match the experimental isotherm under test [47].

There are two variations of the DFT method: non-local DFT (NLDFE) and quenched solid DFT (QSDFT). Current implementations of NLDFE for carbon materials are based on a model

of independent, slit-shaped pores with ideal, graphitic walls. Such a model has a significant drawback if applied to disordered carbons with highly heterogeneous surfaces; it causes artifacts in the estimated pore size distributions. Whereas NLDFT was found to be reliable for characterizing ordered silicas and zeolites, a more recent QSDFT method is more effective for characterizing carbons with heterogeneous surfaces and disordered pore structures [48]. Compared to classical NLDFT (nonlocal density functional theory), the QSDFT model takes into account the carbon surface heterogeneity and significantly improves the method for calculating adsorption isotherms [46]. For this reason, we used QSDFT modeling for data reduction of N<sub>2</sub> isotherms. For CO<sub>2</sub> isotherms, however, QSDFT method was not available, and we performed calculations of pore size distribution using NLDFT and Grand Canonical Monte Carlo (GCMC) approaches.

### 2.2.3. Temperature-Programmed Reduction (TPR) and Chemisorption

Temperature-programmed reduction and chemisorption were carried out in a flow mode using Micromeritics AutoChem 2910. 10.3% H<sub>2</sub> in Ar was used in experiments. Change of hydrogen concentration was registered by TCD detector. For chemisorption, H<sub>2</sub>-containing gas was introduced by a pre-calibrated loop in series. After each introduction, non-adsorbed hydrogen gave a peak in TCD signal with an area proportional to hydrogen content. Thus, given loop volume, initial hydrogen concentration, and hydrogen calibration curve, the volume of irreversibly chemisorbed hydrogen can be calculated. Metal surface area was calculated as follows:

$$A_m = \frac{V_m \times N_A}{(H/Ru) \times d_s} \quad (2 - 1)$$

Metal dispersion was calculated as

$$MD = \frac{V_m \times A_w \times 10^4}{W\% \times (H/Ru)} \quad (2 - 2)$$

Average particle diameter was obtained using the following formula:

$$D_a = \frac{10^4 \times F}{A_m \times d_m} \quad (2 - 3)$$

#### **2.2.4. Preliminary Hydrogenation Experiments**

The goal of preliminary hydrogenation experiments was to get “yes/no” answer regarding activity of the CMS-based catalyst with respect to certain model compounds. In preliminary hydrogenation experiments, a 30 mL batch reactor was used. 10 wt. % aqueous solutions of substrates (20 g of H<sub>2</sub>O plus 2 g of a reactant) and the catalyst (approx. 0.5 g) were loaded into the reactor and were constantly stirred using a magnetic stirrer. Heating of the reactor was implemented by means of a heating tape. Heating power was controlled by a PID controller using input from the thermocouple placed inside the reactor. After reactants and catalyst were loaded, the reactor was closed, purged with nitrogen, checked for leaks and heated to the desired temperature. Then the reactor was immediately pressurized with hydrogen till the desired pressure is reached. The time of hydrogen introduction was considered as the beginning of the reaction. During the batch reaction, the reactor pressure was constantly monitored and recorded. Following the desired reaction time, the stirrer was stopped to signal the end of the batch reaction. Then the reactor was cooled down naturally, and the liquid fraction was filtered and characterized by means of gas chromatography (Agilent Technologies 7890A). Rough estimates

of the substrate conversion were based on 2-point calibration of the GC with respect to each reactant and assuming the total liquid volume to be constant.

### 2.2.5. Tapered Element Oscillating Microbalance (TEOM)

Tapered Element Oscillating Microbalance (TEOM) [49] is a method of analysis that allows registration of mass change of a sample exposed to adsorbate-containing gas phase versus time. Underlying principle of the mass registration in TEOM is a mechanical resonance. The crucial part of the apparatus – tapered element (TE) – contains a sample and oscillates with a certain resonance frequency dependent on the mass. The carrier gas containing an adsorbate enters the top part of the tapered element, proceeds downward through the hollow section and then passes through the packed bed, where it comes into intimate contact with the solid samples. A purge gas passes down around the tapered element to direct the carrier gas stream as it exits from the tapered element. As weight of the sample changes due to adsorption/desorption, it appears as a shift in the frequency. simply comparing the measured natural oscillating frequency to the one recorded at the beginning of the experiment, accurate and time-resolved mass change values can be obtained, according to the following equation [49]:

$$\Delta m = K \left[ \frac{1}{f_1^2} - \frac{1}{f_0^2} \right] \quad (2 - 4)$$

where  $\Delta m$  is the mass change,  $K$  is the spring constant of the tapered element,  $f_0$  is the natural oscillating frequency at time “0”, and  $f_1$  is the natural oscillating frequency at time “1”. Tapered element provides excellent sensitivity, allowing mass changes as little as 1  $\mu\text{g}$  to be detected [49].

A schematic diagram of a TEOM is shown in Figure 2-2.

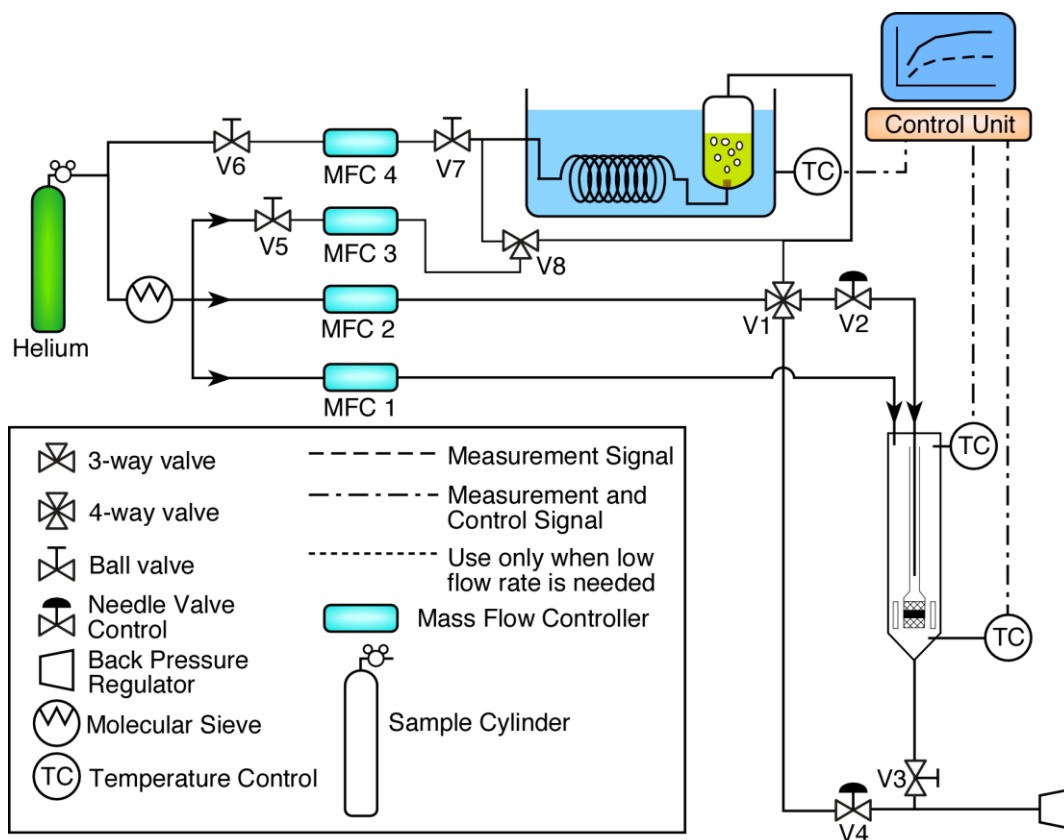


Figure 2-2. TEOM scheme [49]

Inside the TEOM, there are two heating zones for the specific need of temperature control. One (preheating zone) controls the gas-stream temperature upstream of the tapered element while the other (main heating zone) controls the temperature in the tapered element and the packed bed. The top of the tapered element is fixed, so that the whole element can oscillate in a clamped-free mode [49].

The TEOM scheme involves two separate gas lines to allow instantaneous switch between them for sample introduction. The first line delivers pure carrier gas (helium) to the tapered element and is connected with the MFC 2 flow controller. The second line delivers a mixture of adsorbate and the carrier gas and is connected with the saturator and flow controllers MFC 3 and MFC 4. In a default mode, the pure carrier gas from the first line enters the tapered element. The



valve V1 is used to introduce a sample-containing gas from the second line into the tapered element. Flow controllers MFC 2, MFC 3, MFC 4 are set in such a way as to maintain a similar gas flow rate in both lines, so that switching between lines does not alter measurement results significantly. In our experiments, the flow rate of 100 cc/min was used.

Liquid probe compounds are transferred into gas phase using a saturator. Saturator consists of a steel tank containing a sample with an inlet on the bottom and an outlet on the top. Helium flows upward through a layer of a liquid sample and gets saturated with its vapors. A 50  $\mu\text{m}$  porous filter mounted to the bottom creates multiple bubbles, facilitating mass transfer between liquid and gas phases. The saturator is immersed into a water-antifreeze bath. Constant temperature of the bath is controlled with an error of 0.1  $^{\circ}\text{C}$ . In addition, the temperature of the liquid sample is measured precisely with an immersed thermocouple.

## Chapter 3. Synthesis and Characterization of the First Generation of the Catalyst

### 3.1. Synthesis of Plain CMS

First, the synthesis of the plain carbon molecular sieve (i.e., without addition of ruthenium acetylacetonate) was performed to optimize the crucial method for forming CMS materials.

6.8485 g of furfuryl alcohol and 3.2461 g of Triton X-100 were added into three-neck flask while stirring with a magnetic stirrer. Voltage on the heating tape was set equal to 80 V and was constant throughout the experiment. Set voltage was equivalent to the heating power  $\frac{U^2}{R} =$

$$\frac{U^2 I_{max}}{U_{max}} = \frac{80^2 \times 2.6}{120} = 139 \text{ W. Feedback for temperature control was not used.}$$

While stirring, the mixture was heated to 180°C, which was slightly higher than the FA boiling point. After the temperature was reached, reduction of ruthenium acetylacetonate was initiated in reflux mode for 24 hours in an inert atmosphere of nitrogen constantly flowing through the flask. After 24 hours, we found that overheating did not occur and the voltage setting was appropriate for performing the synthesis in reflux mode. The mixture was cooled down naturally to the room temperature.

For FA polymerization, 2.1544 g of oxalic acid powder was dissolved in 3.3005 g of water, and the resulting aqueous solution was added to the flask while stirring. Polymerization was performed at room temperature for 24 hours. Following the polymerization step, we found that the flask contained a homogeneous brown liquid. Assuming that polymerization was not complete, we carried out an additional polymerization step by heating the mixture to 80 °C and maintaining it for 20 hours under nitrogen atmosphere. As a result, a dark solid material was formed, which was insoluble in acetone, toluene, and chloroform. Obviously, “overpolymerization” had occurred leading to the formation of highly crosslinked polymer

insoluble in solvents. On the one hand, we need to synthesize the polymer with high degree of crosslinking in order to obtain a carbon material with high ultramicroporosity from it. However, excessive crosslinking must be avoided since it creates difficulties with transferring the sample from the flask to an evaporating dish for subsequent carbonization. As a solution to this issue, we decided to perform the FA polymerization in two steps: to perform polymerization at ambient conditions inside the flask and to complete the polymer crosslinking at elevated temperatures in an evaporating dish.

The incompletely polymerized material was withdrawn from the flask and placed inside a tube furnace for additional thermal treatment. The heating program was as follows: 5°/min, 50°C for 2 hours, 5°/min, 110°C for 16 hours, 5°/min, 200°C for 6 hours. Then the material was heated to 800°C at 3°/min and maintained at 800°C for 4 hours. The product was ground to 64-106 μm particles and characterized by means of CO<sub>2</sub> and N<sub>2</sub> adsorption. Pore size distribution obtained using DFT method is shown in Figure 3-1, and calculated pore volumes and surface areas are presented in Table 3-1.

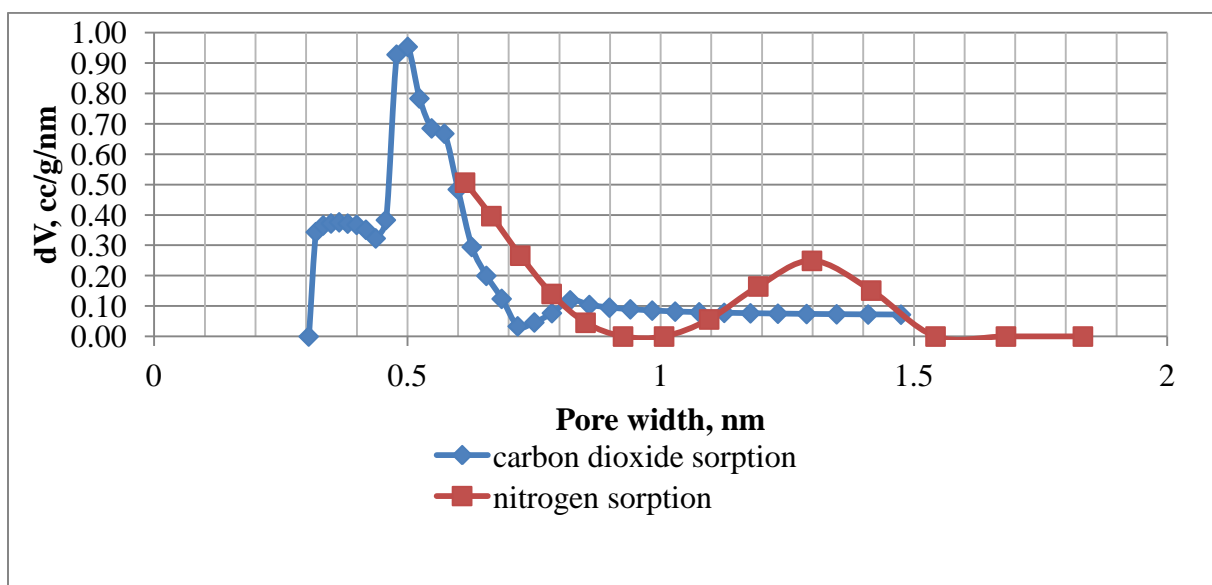


Figure 3-1: Pore size distribution (PSD) of plain CMS materials (without Ru incorporation).

Table 3-1: Pore structure characteristics of plain CMS

	CO <sub>2</sub> adsorption	N <sub>2</sub> adsorption
Surface area, m <sup>2</sup> /g	882	645
Total pore volume, cc/g	0.243	0.220
Mode value of pore size distribution, Å	5.01	6.4

The data obtained from CO<sub>2</sub> and N<sub>2</sub> adsorption measurements clearly indicate the absence of mesopores (>2 nm) in the material. According to CO<sub>2</sub>-based PSD, a majority of the micropore volume lies in ultramicropore region below 7 Å with a mode value of 5 Å and accounts for relatively high surface area of the material (882 m<sup>2</sup>/g). Surprisingly, the N<sub>2</sub> adsorption data also showed high surface area of the CMS material in contrast to published literature data [50]. Typically, surface area values for CMS obtained from N<sub>2</sub> adsorption measurements are 40-50 m<sup>2</sup>/g due to extremely slow diffusion of nitrogen molecules within micropores at the analysis temperature (77 K). We believe that the presence of 1.0-1.5 nm pores (see Figure 3-1) considerably facilitates accessibility of micropores for N<sub>2</sub> molecules [50]. The pores in this size range occupy approximately ¼ of the total ultramicropore volume obtained via CO<sub>2</sub> adsorption measurements and account for ca. 100 m<sup>2</sup>/g of total surface area. We attribute the underlying reason for the formation of 1 – 1.5 nm pores in our particular case to partial gasification of carbon by water added with oxalic acid to the mixture at the polymerization stage and trapped within the polymer upon our attempt to perform polymerization at elevated temperature rather than at ambient conditions.

Despite bimodal pore size distribution, we conclude that we successfully synthesized a carbon molecular sieve with well-developed ultramicroporous structure. This allowed us to proceed to the synthesis of a carbon molecular sieve with embedded ruthenium nanoparticles.

### **3.2. Synthesis of CMS with Encapsulated Ruthenium Nanoparticles**

In the synthesis of the ruthenium-containing catalyst, we used the same procedure as in synthesis of the plain carbon molecular sieve, except that ruthenium acetylacetonate (III) was added along with furfuryl alcohol and Triton X-100 into the flask. However, for the mixture containing ruthenium acetylacetonate, the same heating power (139 W) caused significant overheating after 6 hours of reduction with the temperature in the flask exceeding 200 °C. The possible explanation for such difference in heating regimes is that during synthesis of the catalyst-containing CMS material, the FA is being consumed in the reduction reaction (Figure 2-1), as opposed to synthesis of pure CMS. Despite the high volatility of the products formed in the reduction reaction (b.p. of acetylacetone is 140 °C; furfural : 162 °C versus 170°C for FA), they are likely to remain entirely in a gas phase in the flask at observed temperatures of 180-200°C and therefore do not reduce the boiling point of the liquid mixture. Instead, after the consumption of the majority of furfuryl alcohol, the only liquid compound remaining in the flask is Triton X-100 with the boiling point of 270°C, as well as possible minor amounts of FA oligomers. As a result of lack of components boiling below 180°C in the flask, the temperature started to increase above 180°C. Such overheat can lead to unwanted decomposition and oligomerization reactions, and to avoid this, the heating power was reduced.

We took into account the possibility of overheat during reflux phase and started the new catalyst synthesis procedure with a reduced heating power of 66 W at the end of the experiment. To perform the synthesis, we added 6.5004 g of FA, 6.4914 g of Triton X-100, and 0.3777 g of

Ru(acac)<sub>3</sub> to the flask and refluxed the mixture for 14 hours. The temperature in the flask was maintained in the range of 180-200°C. After completion of the reduction and cooling the mixture, we added 10.90 g of saturated aqueous solution (8.26 wt. %) of oxalic acid [(COOH)<sub>2</sub> • 2H<sub>2</sub>O functioning as the FA polymerization catalyst] to the flask along with 7.2030 g of additional FA. Polymerization was performed under an inert atmosphere (N<sub>2</sub>) for 24 hours at ambient temperature.

Upon completion, the polymer-containing mixture was dissolved in acetone and transferred to a beaker for subsequent ultrasonication, which was done at ambient temperature for 2 hours. Then the solution was transferred into an evaporating dish and placed inside a tube furnace for thermal treatment under nitrogen atmosphere. The temperature program used was based on one published elsewhere [35] and is as follows:

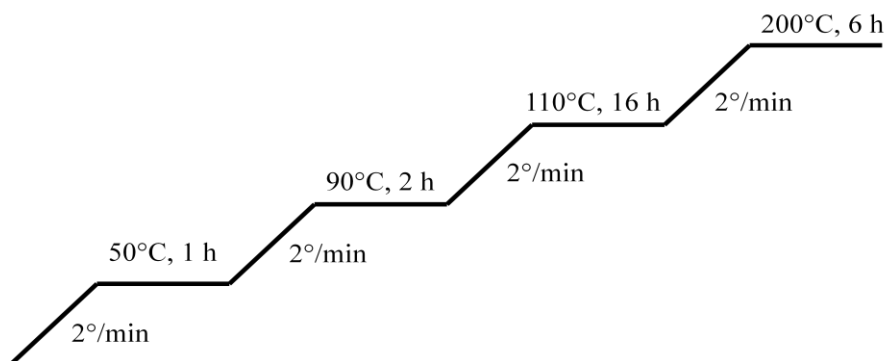


Figure 3-2: Temperature program for the cross-linking stage

The purpose of the first step of heating with the final temperature of 50°C was to evaporate acetone used for dissolution of the original polymer-containing mixture (b.p. 56°C). Then 90°C was maintained for 2 h in order to evaporate water from the mixture (b.p. 100°C). At 110°C polymer molecules start to cross-link. During the final treatment at 200°C for 6 h, oxalic acid present in the mixture was decomposed (decomposition temperature of 130-160°C [51]) the remaining furfuryl alcohol was evaporated (b.p. 170°C), and the final crosslinking occurred.

Instead of a brittle product that would be easy to grind, we obtained a resin-like composite (weight 13.2134 g). To make the product more suitable for grinding, we introduced an additional thermal treatment step as follows:

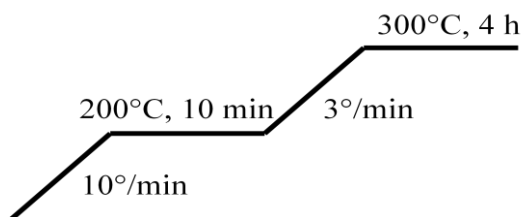


Figure 3-3: Temperature program for additional thermal treatment

The product was brittle and was ground to the particles less than 850  $\mu\text{m}$  in size.

Carbonization of the composite was carried out using the following temperature program:

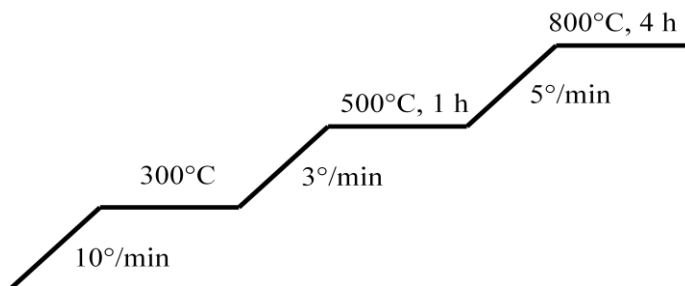


Figure 3-4: Temperature program for the carbonization step

The final carbonization temperature was chosen based on literature data [44] showing that a carbon molecular sieve obtained at final soak temperature of 800°C has the highest pore volume.

The weight of the final product (ruthenium-containing carbon molecular sieve) was 4.0601 g, and its carbon yield was estimated as follows:

$$C\% = \frac{m(\text{product})}{m(\text{FA}) \times \frac{\text{Total molar weight of C in FA}}{\text{Molar weight (FA)}}} \times 100\% = \frac{4.0601}{13.7034 \times \frac{60}{98}} \times 100\% = \mathbf{48.4\%} \quad (3 - 1)$$

This value exceeds the reported data [50]. Assuming losses of ruthenium were negligible, the calculated amount of ruthenium in the catalyst was **2.3 %**. The catalyst is denoted as RuCMS800-1.

### 3.3. Characterization of Catalyst Structure

We investigated the porous structure of the catalyst only by means of N<sub>2</sub> adsorption, since CO<sub>2</sub> adsorption apparatus was not available at that time. Consequently, nitrogen adsorption data could only give information on whether or not mesopores were present in the material without any information on micropores. For calculation of mesopore size distribution, we used BJH model. The obtained size distribution of pores is shown in Figure 3-5. Corresponding pore volume and surface area can be found in Table 3-2.

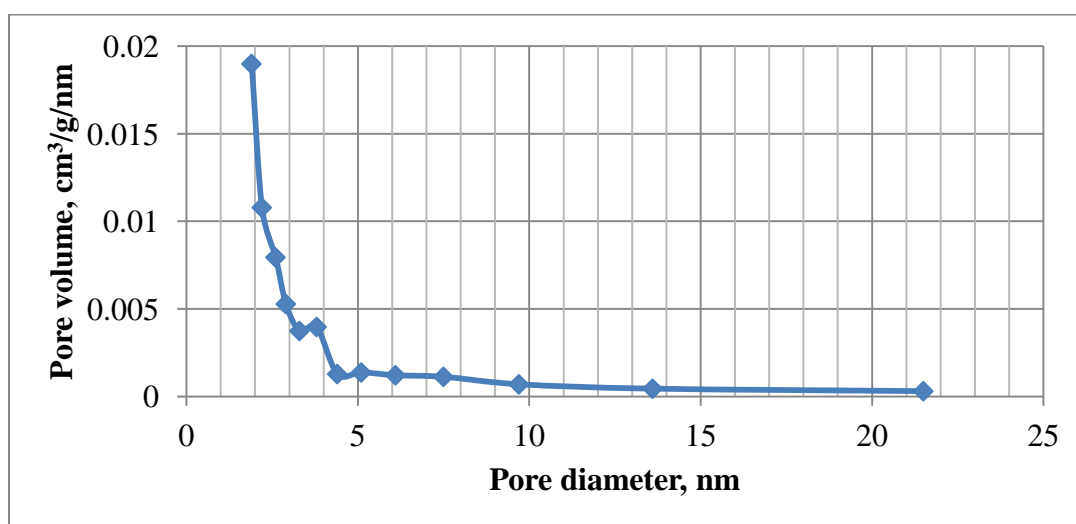


Figure 3-5: N<sub>2</sub> pore size distribution of RuCMS800-1



Table 3-2: Characteristics of pore structure of RuCMS800-1

	N <sub>2</sub> adsorption
BET Surface area, m <sup>2</sup> /g	78
Volume of pores 1.7 – 300 nm, cc/g	0.033

Based on data shown on Figure 3-5 and Table 3-2, we conclude that the volume of mesopores (> 2 nm in size) in RuCMS800-1 is very low. As a result, diffusion limitations within micropores, if they are present in the material, prevent access of nitrogen molecules to the smallest pores at 77 K leading to observed low surface area (78 m<sup>2</sup>/g) volume in agreement with published data [35]. Although presence of mesopores in the catalyst can be beneficial in terms of facilitating diffusion, our goal is to synthesize the material containing micropores only, in order to investigate molecular sieving effects, minimizing interference from larger pores. From this point of view, RuCMS800-1 is more advantageous material compared to plain CMS.

In order to shed light on the state and nature of ruthenium in the catalyst, we investigated the material by means of transmission electron microscopy. To prove the presence of ruthenium in a particular TEM scanned area, EDX method was employed. One of obtained micrographs is depicted in Figure 3-6.

As it is seen in Figure 3-6, plenty of ruthenium nanoparticles less than 5 nm (white dots) are distinguishable. Some bigger particles, up to 20 nm, are also present. The majority of particles less than 3-5 nm is in agreement with reported data on synthesis of platinum-incorporated CMS [35, 38]. Based on the micrograph, it is also important to note that sintering did not occur in spite of extremely high temperatures used during carbonization stage (800°C). It is a clear indication of the fact that, if micropores are present in the material, the metallic nanoparticles are likely to

be bigger than the pores, and therefore cannot migrate at elevated temperatures that would lead to sintering.

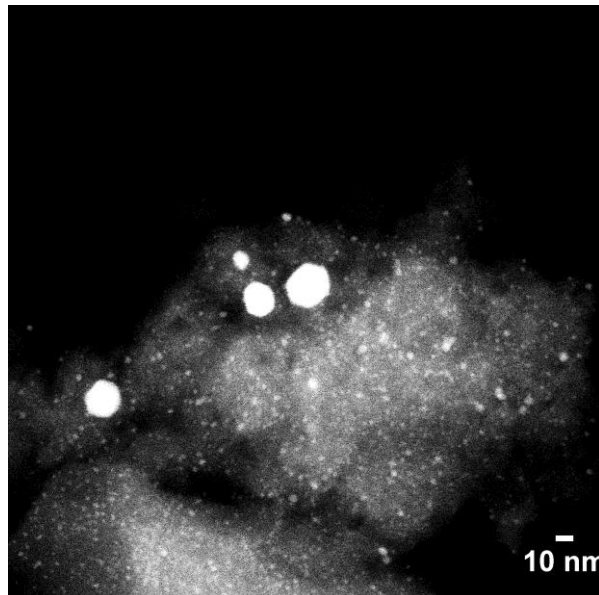


Figure 3-6: TEM micrograph of RuCMS800-1

To further elucidate the nature of ruthenium in the catalyst, we performed temperature programmed reduction (TPR). As shown in Figure 3-7, a peak at ca. 90°C, which is characteristic of ruthenium in an oxidized form [52], is observed indicating the presence of ruthenium oxides in the sample. Since catalyst synthesis was performed in reductive medium under inert atmosphere, the only possible explanation of formation of oxides is due to exposure of the sample to air, which caused partial oxidation of surfaces of ruthenium nanoparticles. Based on this observation, we can conclude that the catalyst needs to be reduced in hydrogen at mild conditions (120°C) before being used in chemical reactions.

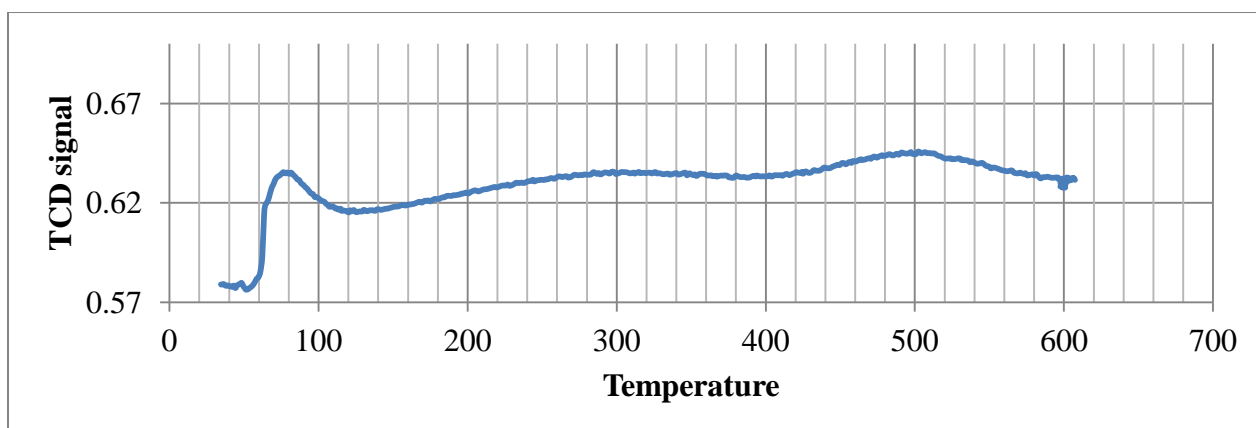


Figure 3-7: Temperature-programmed reduction (TPR) profile for RuCMS800-1

Based on the catalyst characterization data, we conclude that we successfully synthesized a material that meets the following desired criteria mentioned in Chapter 2:

- Ruthenium nanoparticles are uniformly distributed within catalyst pellets (with exceptions);
- Ruthenium nanoparticles are less than 5 nm in size (with exceptions);
- Macropores are absent in the material; mesopore volume is very low.

### 3.4. Preliminary Hydrogenation Studies

Our initial hypothesis was that the Ru-CMS materials can be used for selective hydrogenation of acetic acid and carbonyl compounds in bio-oil. Ruthenium is regarded as the most effective catalyst for hydrogenation of carboxylic acids, aldehydes and ketones [19], but its main disadvantage is that it also catalyzes hydrogenation of aromatic rings [39]. Although the characteristic size of adsorbates for slit-like pores of CMS is a minimum dimension of a molecule (see Section 1.5), and the minimum dimensions of many aromatic compounds and carbonyl compounds are similar (see Appendix A), it was not clear to us how the ultramicropores

are oriented within the material with respect to ruthenium nanoparticles and whether their orientation may pose additional steric hindrances interfering with the adsorption of reactants on ruthenium active sites. In addition, some literature data suggest [28] that in some cases molecular shape selectivity in CMS can be controlled by molecule diameter rather than minimum dimension, as for adsorption of benzene (diameter 5.3 Å) and carbon tetrachloride (diameter 6-7 Å) versus alpha-pyrene (diameter 8 Å) on polyvinylidene chloride-derived CMS. To test whether our catalyst can selectively hydrogenate carbonyl compounds and acids versus aromatics, we carried out liquid phase hydrogenation in a batch reactor and used acetic acid and guaiacol as model compounds. Our goal of preliminary hydrogenation studies was to see if molecular sieve framework of the catalyst is able to inhibit hydrogenation of guaiacol.

The experimental method is described in Section 2.2.4. To perform acetic acid hydrogenation, we dissolved 2.1091 g of acid in ca. 21.0 g of water to obtain 9.3 wt. % solution, which was then loaded into a 30 mL batch reactor along with 0.5111 g of the catalyst. Hydrogenation was carried out for 3 hours at 180 °C. The process temperature was chosen based on reported catalyst screening studies of acetic acid hydrogenation [53], which showed that at 175°C and 750 psi Ru(5%)/C catalyst was effective, providing 74% selectivity to ethanol at 17% conversion of reactant and LHSV 4 h<sup>-1</sup>. Upon hydrogen introduction, the initial pressure inside the reactor was 1193 psi. Pressure profile in the experiment is shown in Figure 3-8.

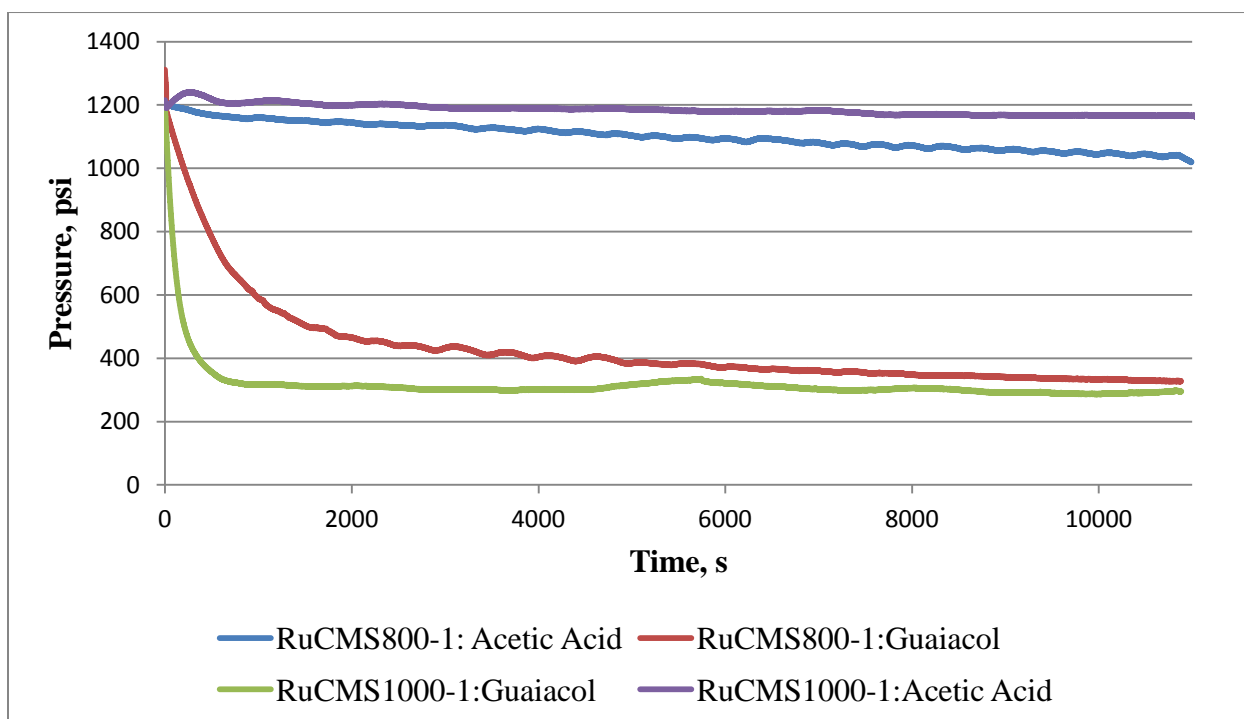


Figure 3-8. Pressure profiles for hydrogenation in a batch reactor

Upon completion of the experiment, gas products were analyzed with GC and showed almost exclusive presence of methane (quantification was not performed due to preliminary character of hydrogenation experiments). Liquid product was collected from the reactor, filtered to remove particles of the catalyst, and then the filter with the catalyst was washed with 9 ml of distilled water. All liquid fractions were combined, mixed, and analyzed by means of gas chromatography. Then area of acetic acid peak was compared to GC results for two acetic acid calibration standards. Calibration curve is shown in Figure C-1 of Appendix C. Based on calibration data, concentration of acetic acid in the aqueous solution was 4.3% and the acetic acid conversion was 34% (see Appendix C for calculations), a promising result. However, it is likely that the most of acetic acid was converted to methane, since the ethanol peak was very small (GC chromatogram is shown in Figure C-2 of Appendix C).

To test the catalyst for guaiacol hydrogenation activity, 0.5076 g of the catalyst, 2.1233 g of guaiacol and 19.883 g of water were loaded into the reactor to get the guaiacol fraction to be approximately 10 % (9.6 wt. %) in the reaction mixture. Hydrogenation was performed at similar conditions as for acetic acid – 180°C for 3 hours. After addition of hydrogen at the beginning of the reaction, initial overall pressure was 1311 psi. Upon completion of the experiment, the liquid product was collected from the reactor and filtered to remove particles of the catalyst. The reactor and the filter were rinsed with 18.5 g of acetone to dissolve the remaining guaiacol adsorbed on reactor walls and on the filter. Then the liquid product dissolved in acetone was analyzed with gas chromatography followed by analysis of calibration solutions of guaiacol dissolved in acetone. Guaiacol conversion was approximately 80 %.

Based on the estimated guaiacol conversion and the hydrogen pressure profile, we conclude that, contrary to our initial hypothesis, the catalyst is much more active for guaiacol hydrogenation than for acetic hydrogenation. In other words, the CMS catalyst was not effective for the separation of guaiacol and acetic acid. The high guaiacol conversion was likely due to the fact that hydrogenation of aromatic rings in the presence of ruthenium progresses much easier than hydrogenation of a carboxyl group. For example, benzene can be hydrogenated with 100% conversion at the temperature as low as 40°C with 87% conversion [54] unlike acetic acid, whose conversion is less than 30% at 175 °C [53].

Since the carbon molecular sieve was not effective in the separation of guaiacol and acetic acid, we also performed glucose hydrogenation to see if CMS is able to prevent access of much bulkier molecules. We dissolved 2.37 g of glucose in 21.35 g of water yielding 10% solution and then loaded the mixture into the batch reactor along with 0.4994 g of the catalyst. The reactor temperature was chosen to be 140°C, lower than 180°C used in hydrogenation of guaiacol and acetic acid, in order to prevent thermal decomposition of glucose [55]. The hydrogenation was

carried out for 2 hours with initial H<sub>2</sub> pressure of 876 psi. The composition of the reaction mixture was analyzed with HPLC before and after reaction. The glucose conversion was found to be 80% with sorbitol being the only product. Hence, the CMS was unable to prevent access of glucose molecules to active sites.

Thus, the hydrogenation experiments revealed that carbon molecular sieve framework of RuCMS800-1 did not show any molecular sieving with respect to acetic acid, guaiacol, and glucose. Assuming that the pore size of carbon support was not small enough to allow such separation, we decided to carry out additional treatment of the catalyst to reduce its pores.

### **3.5. Catalyst Modification by Means of Thermal Treatment at 1000°C**

It is known that increase in final soak temperature during catalyst synthesis results in shrinkage of pores of the carbon material [50]. In order to achieve pore size reduction, we used already synthesized RuCMS800-1 catalyst sample. We heated the catalyst to 800°C with the rate of 10°/min and then increased the temperature to 1000°C with the rate of 5°/min and soaking time of 4 hours. The newly synthesized catalyst was denoted as RuCMS1000-1. We carried out hydrogenation of guaiacol using this catalyst and similar conditions as described above. Weight of guaiacol was 2.0979 g and weight of water – 19.7465 g, which was equivalent to 9.6 % fraction of guaiacol in the mixture. 0.5011 g of the catalyst RuCMS1000-1 was loaded into the reactor. Hydrogenation was carried out at 180°C for 3 hours, and reaction products were dissolved in acetone and analyzed in a similar way as described earlier. Contrary to expectations, the RuCMS1000-1 also showed high guaiacol conversion with the hydrogen pressure decreasing at a much higher rate than for RuCMS800-1 catalyst as seen in Figure 3-8. This indicates that the RuCMS1000-1 is more active than RuCMS800-1 for guaiacol hydrogenation. Clearly, instead of being shrunk, the pores became larger in size and more accessible to guaiacol

molecules. The pore size distribution for RuCMS1000-1 in comparison to RuCMS800-1, shown in Figure 3-9, confirms this.

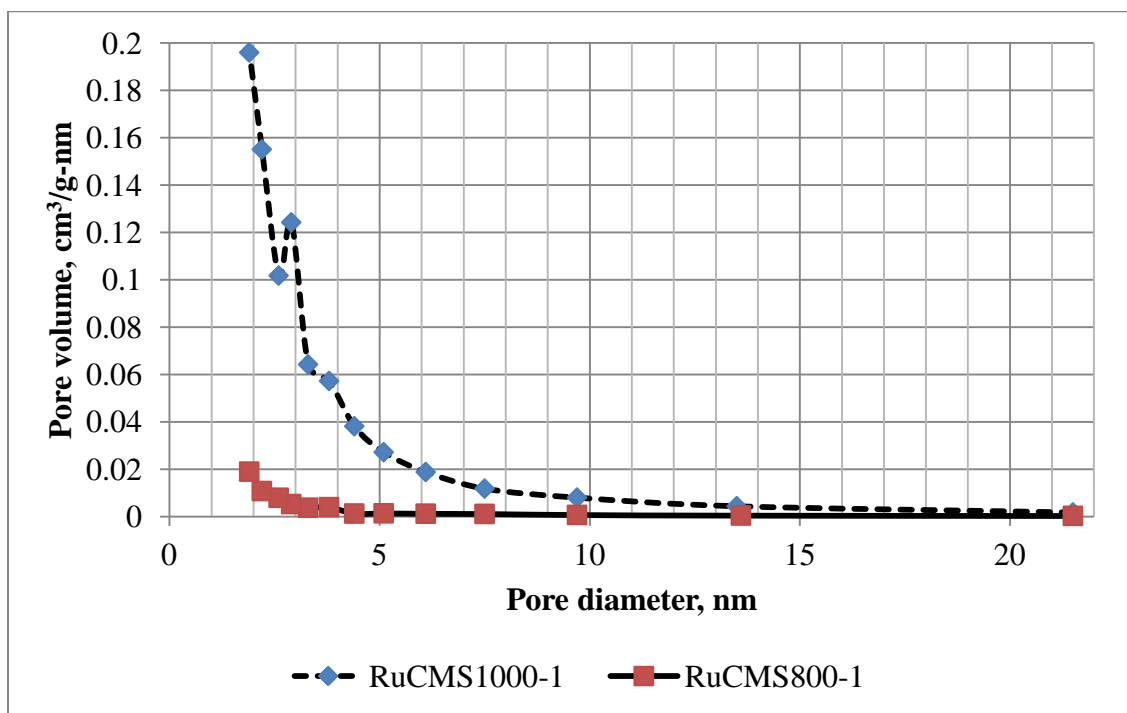


Figure 3-9. N<sub>2</sub> pore size distributions for RuCMS800-1 and RuCMS1000-1

The pore size distribution reveals that the thermal treatment at 1000°C increased the mesoporosity, resulting in increase of catalyst surface area from 78 to 773 m<sup>2</sup>/g (mostly in the mesopores – the volume of pores between 1.7 nm and 300 nm increased from 0.03 to 0.43 cc/g). Apparently, the presence of mesopores in the material facilitated diffusion of guaiacol molecules resulting in much higher catalyst activity. In order to explain the appearance of mesopores during 1000°C treatment (not previously described in literature), we recall that in our case we treated an already synthesized sample, which was exposed to air before thermal treatment. We hypothesize that oxygen adsorption (from air) in micropores caused the formation of mesopores. Upon thermal treatment at 1000°C, the trapped oxygen trapped in the pores oxidized part of carbon support to CO<sub>2</sub> and created cavities in the size range of mesopores. Supporting this hypothesis,



the weight of the catalyst sample was found to decrease approximately two-fold (from 1.0196 g to 0.5200 g) following the thermal treatment at 1000°C.

It is interesting to note that, although the catalyst became much active in guaiacol hydrogenation after thermal treatment, its activity in acetic acid hydrogenation was likely to diminish, as comparison of pressure profiles of RuCMS800-1 and RuCMS1000-1 suggests (Figure 3-8). We assume that this difference was due to different limiting stages in those two processes. Hydrogenation of aromatics, including hydrogenation of guaiacol, on Ru catalyst is a fast reaction, and therefore it is likely that overall hydrogenation process was limited by diffusion of guaiacol within carbon micropores. When mesoporosity is introduced, it facilitated diffusion and hence accelerated hydrogenation. Acetic acid hydrogenation, on the other hand, is a slow reaction, and is likely to be kinetically limited in both cases. As a result, the overall process rate was unaffected by presence or absence of mesopores within the carbon support. Decrease in hydrogen consumption during acetic acid hydrogenation after treatment of the catalyst at 1000°C could be explained as ruthenium nanoparticles, regardless of presence or absence of mesopores, are still accessible to molecules of reactants through ultramicropores. Treatment at 1000°C caused ultramicropores to shrink and therefore reduced micropore volume accessible to reactants. As a result, ruthenium nanoparticles became less accessible to acetic acid molecules and the catalyst activity decreased. Our subsequent adsorption studies of the catalyst obtained at 1000°C support this hypothesis, as we showed that 1000°C treatment reduces accessible pore volume.

Formation of mesopores within carbon support after thermal treatment suggests that the catalyst must be used with caution in high temperature processes unless its prior degasation has been conducted. On the other hand, formation of mesopores after heating of the catalyst sample

exposed to air can become a cheap way to introduce mesoporosity in the catalyst and remove diffusion limitations within catalyst pellets.

Summing up, the results on hydrogenation of model compounds using RuCMS800-1 catalyst suggested that carbon support does not have shape selectivity with respect to acetic acid, guaiacol, and glucose. The possible reason for lack of selectivity is two-fold. On one hand, ultramicroporous structure of the carbon support can be underdeveloped or pores can be too wide to cause shape selectivity. On the other hand, similarities in structures of guaiacol, acetic acid and glucose can exist, making them adsorbing and diffusing within ultramicropores in the similar manner. Regarding the latter cause, we modeled molecular structure of those compounds using MARVIN software and found that guaiacol, acetic acid and the aldehyde form of glucose have similar values of minimum dimension (thickness) – about 4.0-4.1 Å, which is equal to the thickness of methyl functional group (see Section 1.5). The slit-like shape of CMS ultramicropores suggests adsorption and diffusion controlled by minimum dimension of adsorbates.

To determine the real cause of observed lack of hydrogenation selectivity and elucidate pore structure and molecular sieve properties of carbon support, we formulated the following steps in research to be taken:

- Synthesis of a new portion of the catalyst
- CO<sub>2</sub> adsorption in addition to N<sub>2</sub> adsorption to shed light on pore size distribution in ultramicropore range inaccessible for N<sub>2</sub> molecules at 77 K
- Adsorption studies involving model molecules of different size using tapered element oscillating microbalance (TEOM) to obtain evidence or prove absence of molecular sieve effect of the support.

These steps and their results are described in detail in the next section.

## Chapter 4. Synthesis and Characterization of the Second Generation of the Catalyst

### 4.1. Synthesis of the Second Generation Catalyst

To prepare a second version of the Ru-CMS catalyst, we added 13.6008 g of furfuryl alcohol, 13.636 g of Triton X-100 and 0.8004 g of ruthenium acetylacetonate into the three-neck flask. Reduction of ruthenium precursor was conducted in a reflux mode for 24 hours in an inert atmosphere of nitrogen, as described earlier.

For polymerization step, an aqueous solution of oxalic acid (used as polymerization catalyst) was prepared by dissolving 2.6668 g of oxalic acid dihydrate in 20.5208 g of water to obtain a 8.26 wt. % solution (saturated solution). The acid solution was then added to the mixture from the reduction stage onwards along with 15.0027 g of furfuryl alcohol. Polymerization and the following ultrasonication were performed in a manner described earlier.

To evaporate acetone and water from the catalyst precursor-containing solution in a controlled manner and avoid splashing of the mixture during thermal treatment in a tube furnace, we added one more step to our catalyst preparation procedure – solvent evaporation under vacuum. The solution was transferred into evaporating dishes and then placed into the vacuum oven. Acetone and water were evaporated at a pressure of 100 Torr and ambient temperature. Then the polymer (viscous black liquid) was placed inside the tube furnace for the second stage of polymerization. The first stage of thermal treatment at 110 °C was performed following the program shown in Figure 3-2. Then, unlike the first synthesis, temperature was increased directly to 300°C at a rate of 2°/min and was kept for 6 hours. Since the obtained solid product was not brittle enough to be ground, additional thermal treatment at 300°C was required at the same conditions. It is important to note that, in order to avoid undesired air adsorption in micropores

of CMS, carbonization at 800 and 1000°C was performed in parallel using the same precursor in contrast to the first generation catalyst carbonized successively. In addition, prior to carbonization all polymer composites were vacuumed at 50°C (100 Torr) for one hour to remove adsorbed air molecules.

After carbonization, the catalyst was ground and sieved to obtain fractions of particle sizes 64-105 and 20-32  $\mu\text{m}$ . The former was used for  $\text{CO}_2$  and  $\text{N}_2$  adsorption studies, and the latter – for TEOM adsorption and TEM analysis.

#### 4.2.Characterization of Catalyst Structure

We measured mesopore size distribution and pore volume by means of the same method we used for characterization of RuCMS800-1 sample –  $\text{N}_2$  adsorption at 77 K with BJH calculations. Pore size distribution of RuCMS800-2 in comparison with RuCMS800-1 is shown in Figure 4-1.

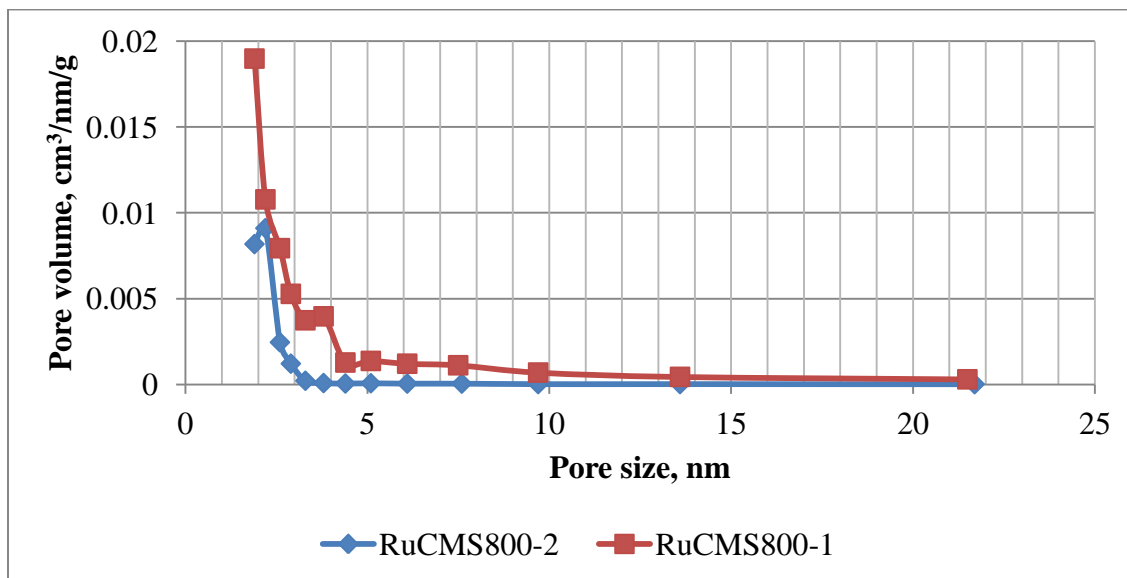


Figure 4-1: Comparison of pore size distributions of RuCMS800-1 and RuCMS800-2

We infer from Figure 4-1 that the second version of the catalyst has less mesoporosity compared to RuCMS800-1 catalyst. Cumulative volume of pores in the 1.7-300 nm range measured by N<sub>2</sub> adsorption for RuCMS800-2 is 0.0076 m<sup>3</sup>/g and BET surface area is 49 m<sup>2</sup>/g, which is lower than the corresponding values of 0.0328 m<sup>3</sup>/g and 78 m<sup>2</sup>/g measured for the first version of the catalyst.

In Figure 4-2 pore size distribution for RuCMS1000-2 in comparison to RuCMS800-2 is shown.

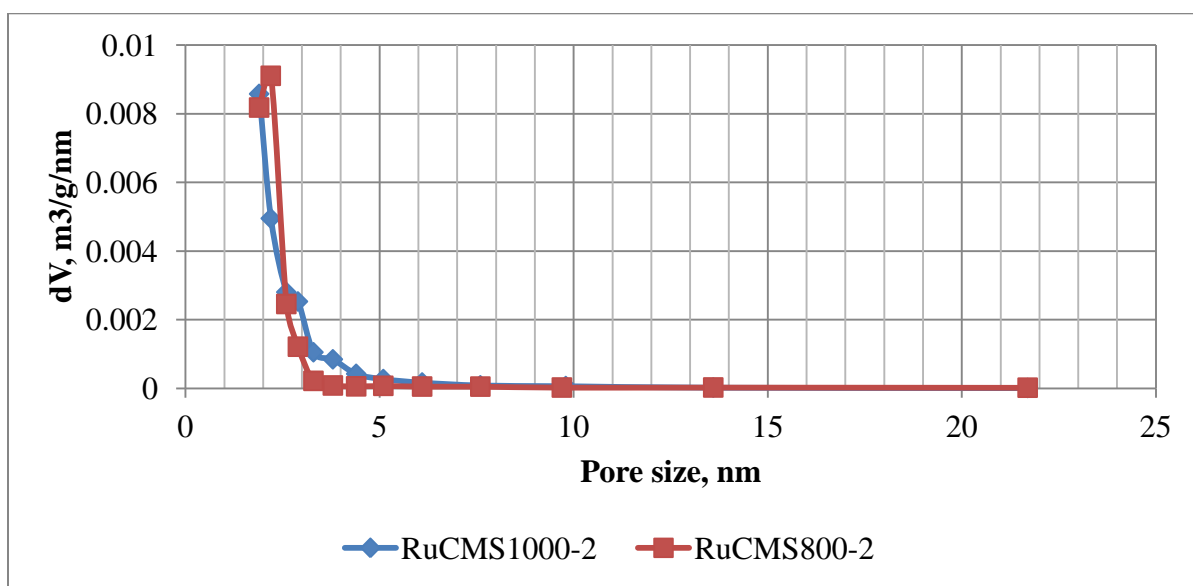


Figure 4-2: Comparison of pore size distributions of RuCMS800-2 and RuCMS1000-2.

We see that the distribution of mesopores in RuCMS1000-2 does not differ significantly from that of RuCMS800-2. Hence, the one-step carbonization of polymer composite at 1000°C did not cause formation of mesopores as opposed to synthesis of RuCMS1000-1 obtained by two-step carbonization at 800°C and 1000°C with intermediate product being exposed to air. It supports our hypothesis that the adsorption of air in the ultramicropores could be the main cause in the development of mesoporosity upon heating to 1000°C.

TEM micrographs shown in Figure 4-3 reveal that ruthenium nanoparticles are uniformly distributed within a catalyst particle and majority of them have a diameter less than 3 nm. Compared to TEM micrographs obtained for RuCMS800-1 (Figure 3-6), large particles up to 20 nm are not observed. The possible cause for formation of such large ruthenium particles was sintering of smaller particles at high temperatures due to their migration within mesopores. In RuCMS800-2, the catalyst mesoporous structure is much less developed than in RuCMS800-1, and therefore we believe that particle migration is less likely to occur. If we assume that majority of pores are in ultramicropore range (proven later by characterization data), the 1-3 nm ruthenium particles will not fit into pores smaller than 1 nm and therefore become trapped in a carbon ultramicroporous structure.

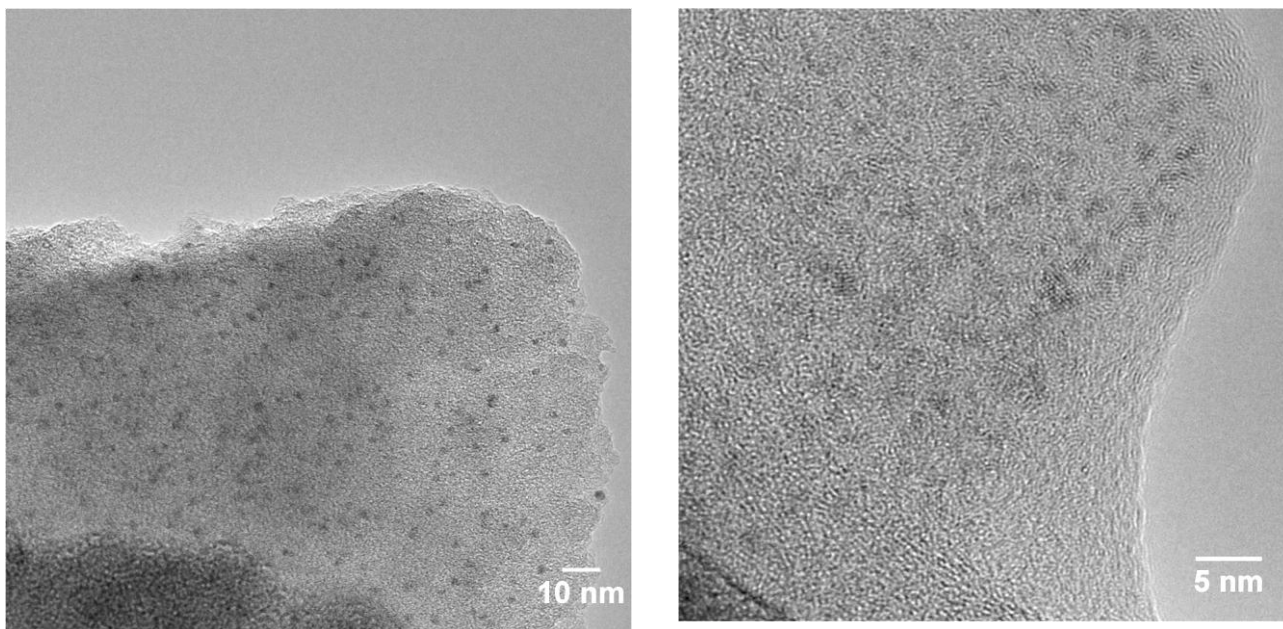


Figure 4-3: TEM micrographs of RuCMS800-2

It is important to note that the majority of ruthenium nanoparticles are located within carbon porous framework rather than on the surface of catalyst pellets as a result of the preparation procedure, in which the precursor of the catalyst was the colloidal solution of ruthenium nanoparticles homogenized by means of ultrasonication.

Summing up, N<sub>2</sub> and CO<sub>2</sub> absorption data reveal that the catalyst contains negligible volume in mesopores, and TEM micrographs show desired size distribution of metal nanoparticles. In addition, some features of TEM micrographs can be interpreted as evidence of microporous structure of the material. On the right part of Figure 4-3 it can be seen that the edge of the catalyst particle is made up of randomly positioned slits that are likely to be graphite 2D layers. As pointed out in Section 1.6, the ultramicropores of CMS are a consequence of the lack of order in carbon structure, and therefore the observed disorder suggests that ultramicroporous structure responsible for molecular sieve effect is also present.

To further elucidate the ultramicroporous structure of the carbon support, we characterized RuCMS800-2 by CO<sub>2</sub> adsorption at 273 K along with N<sub>2</sub> adsorption at 77 K and deduced pore size distribution by means of NLDFT and QSDFT models of slit pores, respectively. Pore size distribution for RuCMS800-2 is shown in Figure 4-4. The surface area and the pore volume are shown in Table 4-1.

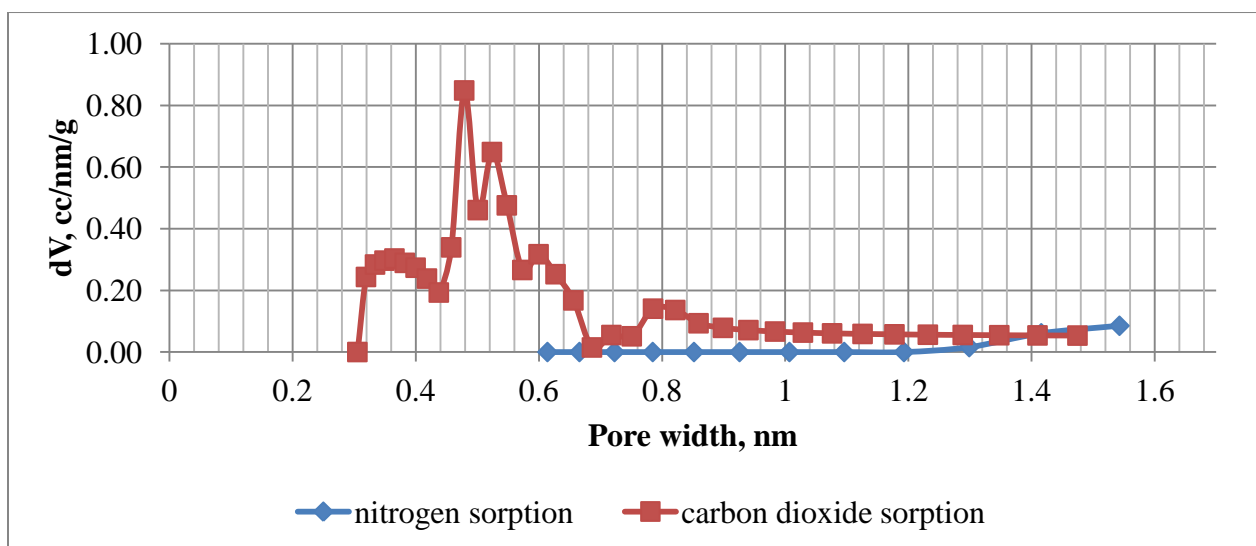


Figure 4-4: Pore size distribution of RuCMS800-2

Table 4-1: Characteristics of pore structure of RuCMS800-2

RuCMS800-2	CO <sub>2</sub> adsorption	N <sub>2</sub> adsorption
Surface area, m <sup>2</sup> /g	646.1	26.6
Total pore volume, cc/g	0.18	0.02
Mode value of pore size distribution, Å	4.79	15.43

Based on CO<sub>2</sub> adsorption data, we conclude that RuCMS800-2 catalyst has well-developed ultramicroporous structure with pores less than 8.2 Å in size constituting 78% of the total pore volume. Total pore volume is 0.18 cc/g. High surface area of the material is in agreement with published data on poly(furfuryl alcohol)-derived CMS [28]. Pore size distribution based on nitrogen adsorption at 77 K using QSDFT model displayed absence of pores larger than 1.54 nm for RuCMS800-2. Ultralow pore volume obtained with N<sub>2</sub> adsorption (0.02 cc/g versus 0.18 cc/g for CO<sub>2</sub> adsorption) may be explained by non-equilibrium adsorption due to extremely slow activated diffusion of N<sub>2</sub> molecules within micropores at 77 K, in accordance with the literature



[28]. This result is apparent if we look at N<sub>2</sub> adsorption-desorption curves in Figure 4-5. Desorption curve goes upward despite the decrease in relative pressure, since equilibrium was not reached at lower N<sub>2</sub> pressures and the material keeps adsorbing gas being away from equilibrium. CO<sub>2</sub> adsorption-desorption isotherms (Figure 4-6) do not show hysteresis, since the ultramicropores are easily accessible to the CO<sub>2</sub> molecules which also diffuse at higher rates in ultramicropores at the adsorption temperature of 273 K.

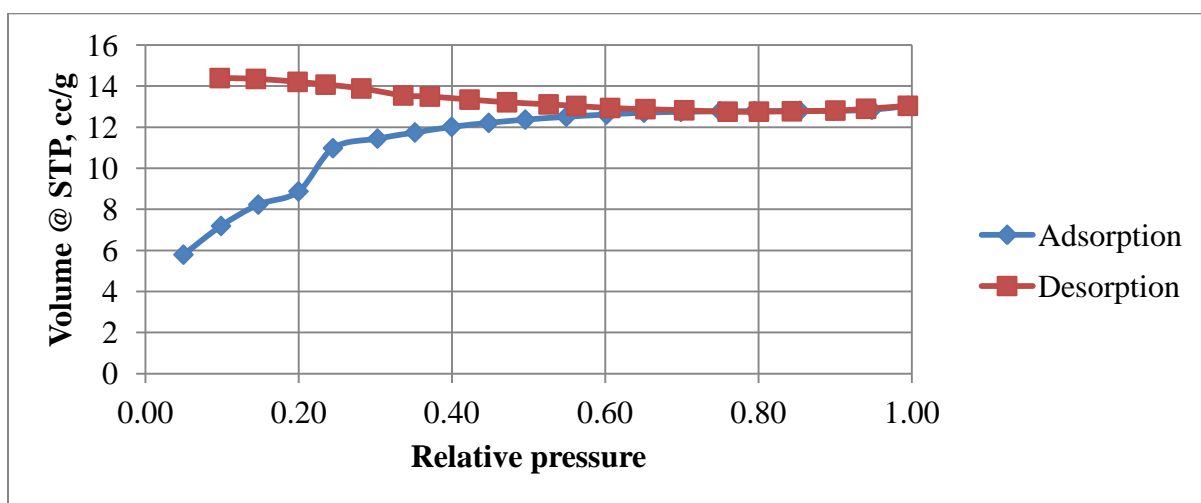


Figure 4-5: N<sub>2</sub> adsorption isotherm for RuCMS800-2

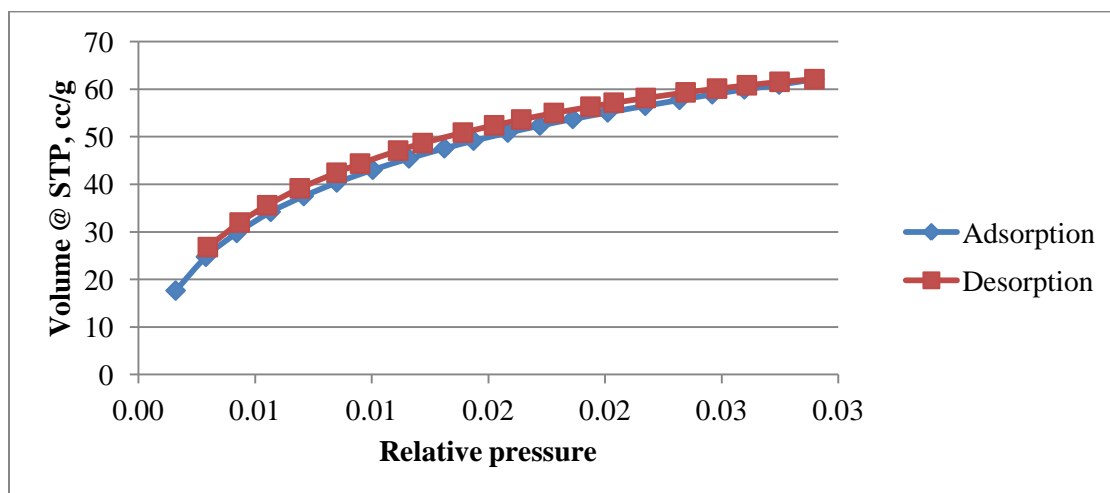


Figure 4-6: CO<sub>2</sub> adsorption isotherm for RuCMS800-2

If we examine the pore size distribution for RuCMS800-2 obtained using NLDFT method, we notice minima at distribution for 4.5 Å, 5.8 Å and 7 Å pores. Such minima are known to be artifacts of the NLDFT calculations and arise due to the heterogeneity of carbon pore walls [46]. As it was noted in Section 2.2.2, QSDFT is a more preferable method for accurate description of the heterogeneous porous structure of carbon. However, the QSDFT method is not available for reduction of CO<sub>2</sub> adsorption data, and the most accurate method available to obtain pore size distribution based on CO<sub>2</sub> adsorption is NLDFT. To validate the results obtained by NLDFT, we calculated pore size distribution using another available model – GCMC. The result is shown in Figure 4-7.

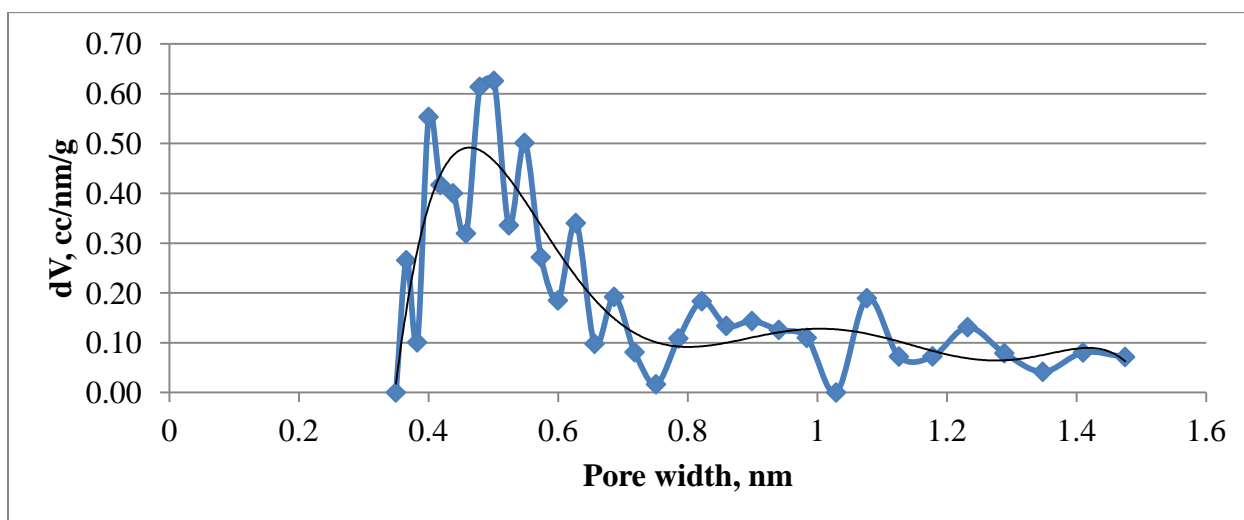


Figure 4-7: CO<sub>2</sub> pore size distribution of RuCMS800-2 obtained using GCMC method

Despite the fact that the pore size distribution obtained using GCMC shows even more artifacts than NLDFT, the general result is the same – that pores less than 7 Å constitute a majority of the pore volume, and the mode value of distribution is approximately 5 Å.

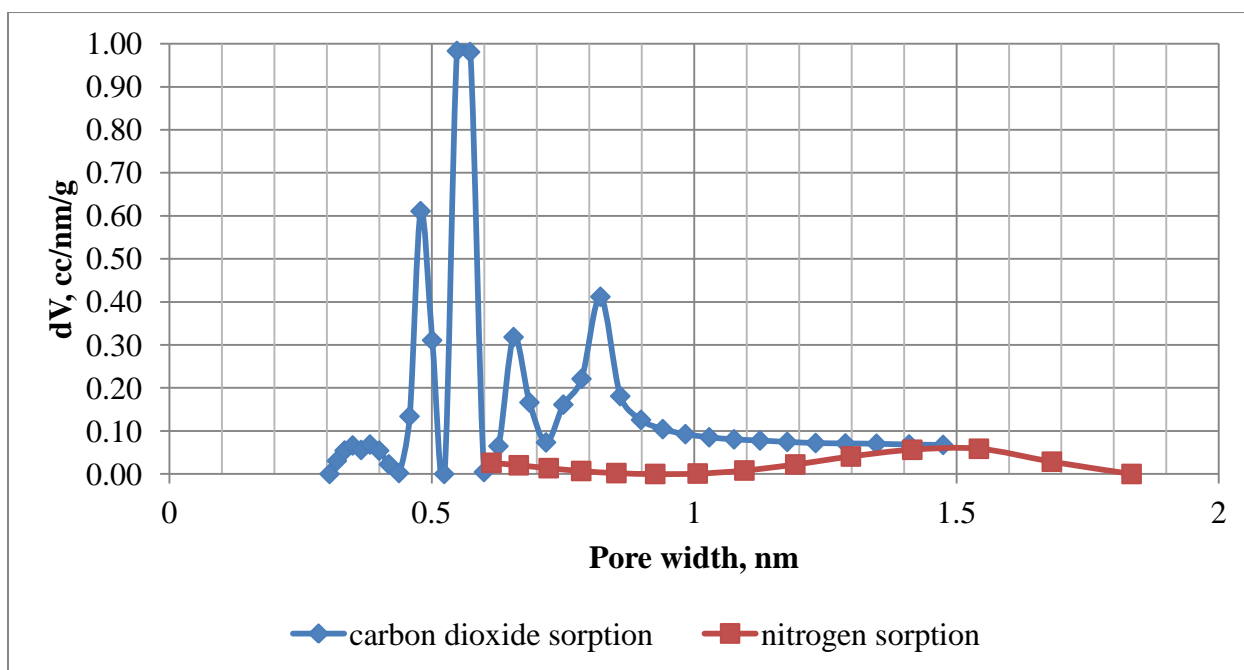


Figure 4-8: Pore size distribution of RuCMS1000-2

Table 4-2: Characteristics of pore structure of RuCMS1000-2

RuCMS1000-2	CO <sub>2</sub> adsorption	N <sub>2</sub> adsorption
Surface area, m <sup>2</sup> /g	529.4	63.2
Total pore volume, cc/g	0.18	0.034
Mode of pore size distribution, Å	5.48	15.43

CO<sub>2</sub> and N<sub>2</sub> adsorption results for RuCMS1000-2 are compared in Figure 4-8 and Table 4-2. Thermal treatment at 1000°C did not change the ultramicroporous character of structure of the support significantly. Compared to the observed distribution for RuCMS800-2, RuCMS1000-2 demonstrates slightly higher volume of pores in the range 8-10 Å and more prominent minima in distribution, suggesting high heterogeneity of pores. RuCMS1000-2 also has slightly higher volume of mesopores and lower total surface area. Although pore size distributions indicate increase in pore sizes with increase of final carbonization temperature from 800°C to 1000°C,

CO<sub>2</sub> adsorption-desorption isotherms show interesting behavior (Figure 4-9). Figure indicates remarkable hysteresis during adsorption-desorption; desorption is much less effective than adsorption. Although hysteresis often indicates capillary condensation in meso- and macropores, this is not the case for our material, since mesopore volume is small and “invisible” for CO<sub>2</sub> at the given pressures (below 1 atm). Another possible explanation of low pressure hysteresis is the activated passage of molecules through pre-existing constrictions into wider cavities [56]. This interpretation seems reasonable for our catalytic system, if we hypothesize that, in spite of slightly higher ultramicropore sizes of RuCMS1000-2 versus RuCMS800-2, RuCMS1000-2 has narrower pore openings. As a result, stronger interaction between CO<sub>2</sub> molecules and pore walls in a proximity of pore openings create a “jam” that hinders desorption. The observed hysteresis suggests that pores of the catalyst have bottle-like structure.

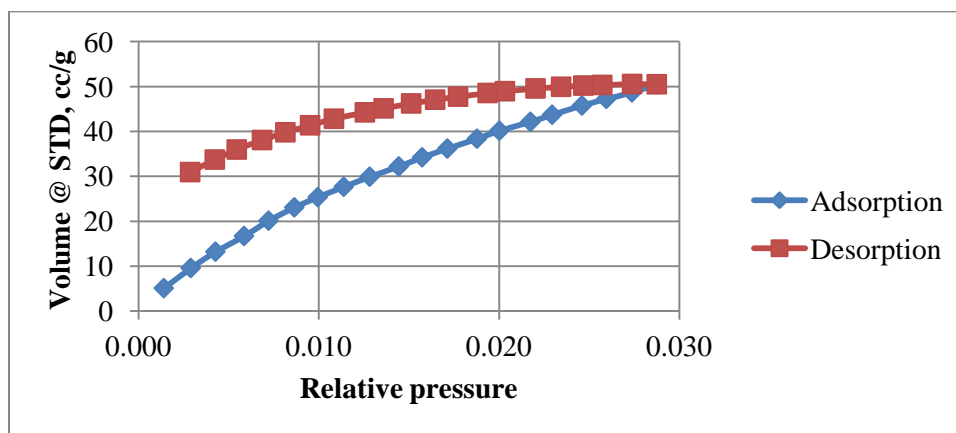


Figure 4-9: CO<sub>2</sub> adsorption-desorption isotherms for RuCMS1000-2

From CO<sub>2</sub> and N<sub>2</sub> adsorption data for RuCMS800-2 and RuCMS1000-2 catalysts, we conclude that both materials have desired ultramicroporous structure with pores surrounding ruthenium nanoparticles much smaller (<0.7 nm) than nanoparticles diameters (1-3 nm).

Large diameter of metal nanoparticles prevents them from migrating within ultramicropores and undergoing sintering. Thus, the catalyst structure is stable and sintering does not occur upon heating at 800 °C during the last stage of catalyst preparation. The proposed “berries-in-a-muffin” structure is visible in Figure 4-3, in which ruthenium crystallites (dark spots) are likely to be surrounded by graphite slits.

### **4.3. Testing Molecular Sieve Effect**

Molecular sieving properties of a material are typically investigated by sorption of molecules of different size from gas phase [28]. The material with prominent sieving properties has a well-developed ultramicroporous structure, capable of absorbing only molecules smaller than a certain cutoff size. As a result, adsorption studies clearly demonstrate remarkable differences in uptake of small molecules versus large ones, inaccessible to the pores.

#### **4.3.1. Choice of Probe Molecules**

To determine whether the synthesized CMS-based ruthenium catalyst demonstrates molecular sieving properties, we performed adsorption measurements involving model compounds. Probe molecules were chosen on the basis of the following criteria:

- A. They represent classes of compounds constituting pyrolysis bio-oil: aldehydes, ketones, furanes, oxygen-containing aromatics, etc.;
- B. They are sufficiently volatile to have a vapor pressure greater than  $0.01P_{\text{atm}}$  at temperatures below 60°C, so that a saturator heated by a water bath can be used;

- C. Probe molecules contain double bonds and are reducible by hydrogen, so that adsorption data can be coupled with their hydrogenation studies.

Table 4-3 represents the compounds chosen for adsorption studies of the CMS-based catalysts. The method of calculation of minimum dimensions is described later.

Table 4-3: Model compounds chosen for testing molecular sieve effect

Compound	Boiling point, °C	Minimum dimension, Å	Analog in bio-oil
Acetaldehyde	20.2	4.13	hydroxyacetaldehyde
Acetone	56	4.09	hydroxyacetone
Anisole	154	4.09	guaiacol
Furfural	162	3.4	furans
Water	100	Water clusters	Water
Tetrahydrofuran	66	5.29	-
Cyclohexanone	155.6	5.38	-

Although analogs of tetrahydrofuran (THF) and cyclohexanone are not present in pyrolysis bio-oil, their choice as probe molecules was dictated by their relatively large size. In addition, their corresponding analogs may form in hydrogenation of furans and aromatics during bio-oil upgrading.

Minimum dimensions of model compounds shown in Table 4-3 were first estimated using heuristic approach (see Section 1.5), and then were verified by a more elaborate procedure. In the

method, a set of conformers for each substance was modeled using MARVIN software. Then minimum dimensions of conformers were determined, and the lowest value was assumed to be a minimum dimension of a probe molecule.

#### **4.3.2. Choice of Adsorption Temperature**

The lower bound of possible adsorption temperature values is dictated by a method to bring liquid model compounds to gas phase. In our experiments, we used a saturator heated by a water bath with the limit temperature of 60°C to evaporate liquid compounds. Consequently, adsorption temperature should not be lower than 60-70°C to avoid undesired condensation of vapors inside an adsorption apparatus. The upper bound of the temperature interval is dictated by thermal stability of molecules used, since the possible occurrence of decomposition and polymerization reactions at higher temperatures will complicate the analysis and interpretation of its results. In addition, adsorption temperature must be high enough to allow hydrogenation reactions in presence of hydrogen, so that adsorption and hydrogenation data will be obtained in similar conditions and can be compared. Hydrogenation of carbonyl groups and aromatic rings on ruthenium catalysts typically occurs at 100-150°C [39]. Accounting for these considerations, we chose the temperature in adsorption studies to be 120°C.

#### **4.3.3. Setting and Determination of Adsorbate Concentrations**

Temperatures in the bath were chosen based on volatilities of compounds used. The temperatures were typically set below +60°C to minimize evaporation of water from the bath. Temperatures used in the saturator are shown in Table 4-4. Corresponding vapor pressures are

calculated using HYSYS software and PRSV Equation of State. PRSV model was chosen over more commonly used Peng-Robinson model due to more accurate predictions of low vapor pressures [57]. Saturator temperatures were chosen to ensure that the concentration of a compound in gas phase lies in a range 2-25 vol. %. Liquid-phase equilibrium inside the saturator was assumed.

Table 4-4: Conditions in the saturator with respect to model compounds used

Compound	Temperature, °C	Vapor pressure, kPa
Acetaldehyde	-15	21.29
Acetone	20	24.78
THF	20	17.26
Furfural	60	1.633
Anisole	60	3.446
Water	60	19.9
Cyclohexanone	60	3.043

Desired concentrations of adsorbates were obtained by dilution of the saturator outlet flow with pure carrier gas, as shown in Figure 4-10. Here, the flows of a gas passing through the saturator and a dilutant are adjusted by flow controllers MFC4 and MFC3, respectively.



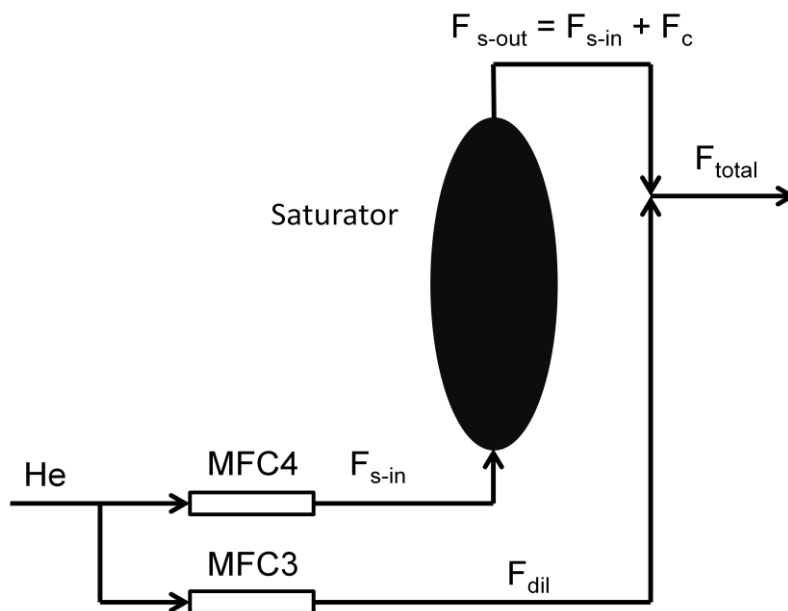


Figure 4-10: Flow dilution scheme

If temperature of liquid and hence its vapor pressure inside the saturator is known, a flow rate of a dilutant can be easily calculated and set using the flow controller MFC3. However, effect of change in the flow passing through the saturator on the temperature must be taken into account. As we mentioned before, the total flow rate in both TEOM gas lines must be equal to 100 cc/min all the time throughout a sorption measurement, regardless of adsorbate concentrations. It means that, in order to obtain desired adsorbate concentrations in gas phase, the helium flow through the saturator needs to vary along with the diluting flow. Consequently, the change in the flow will alter the temperature inside the saturator, giving different vapor pressure. To account for this temperature, we developed the algorithm aimed at correct setting of MFC3 and MFC4 flow rates and accurate prediction of adsorbate concentrations in gas phase. The algorithm is depicted in Figure 4-11.

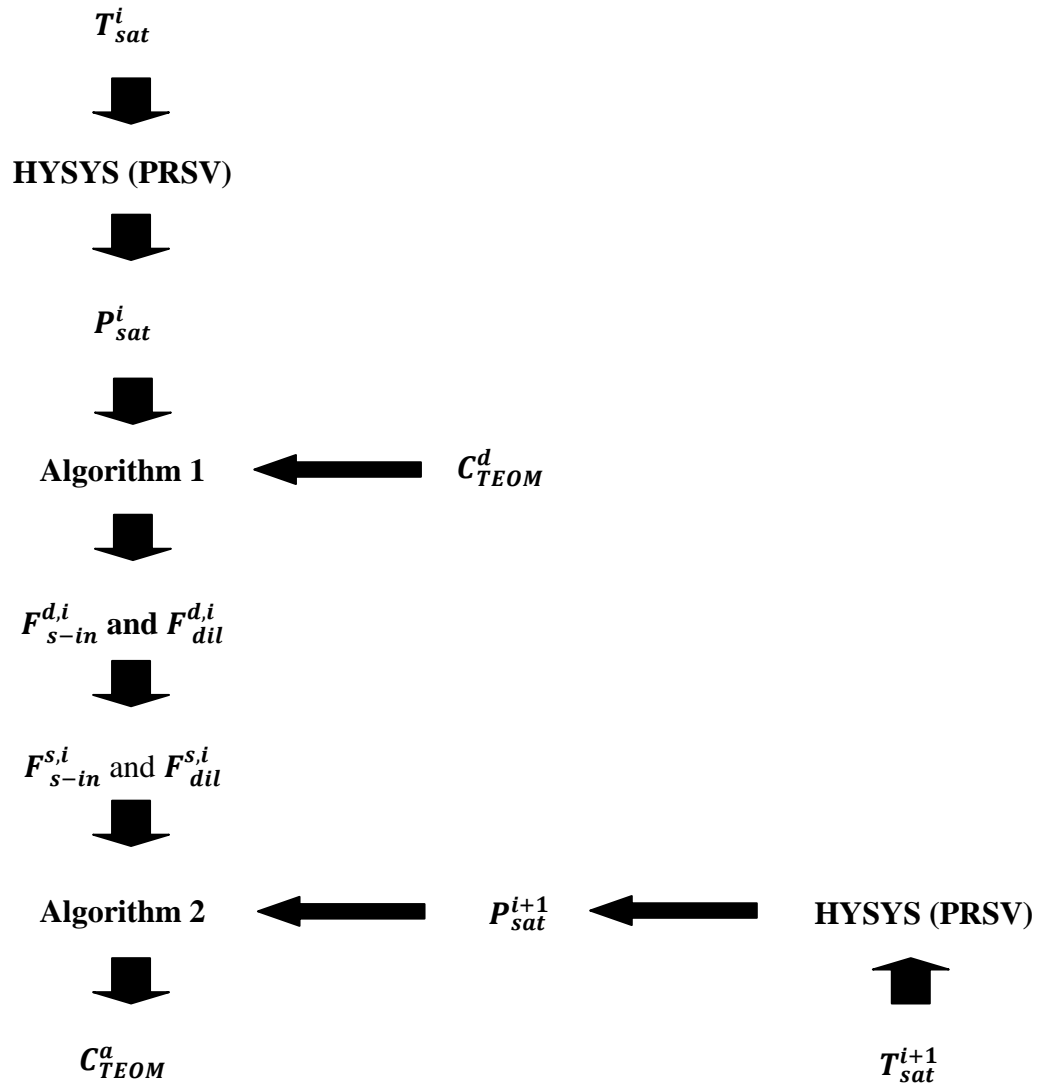


Figure 4-11: Algorithm for setting and calculation of adsorbate concentrations

We denote desired concentration of an adsorbate in gas phase as  $C_{TEOM}^d$ . At a particular time moment the temperature inside the saturator is  $T_{sat}^i$ , corresponding to the vapor pressure  $P_{sat}^i$ . In order to calculate correct MFC3 and MFC4 flow rates to reach the desired adsorbate concentration, we suggest application of the Algorithm 1, involving the steps shown below:

1. Calculation of the desired flow rate of pure adsorbate:

$$F_c^d = \frac{C_{TEOM}^d}{100\%} \times F_{total}^d \quad (4 - 1)$$

2. Calculation of the desired total *helium* flow rate:

$$F_{He,total}^d = F_{total}^d - F_c^d \quad (4 - 2)$$

3. Calculation of the current concentration of an adsorbate in gas phase inside saturator:

$$C_{sat}^i = \frac{P_{sat}^i}{101.3 \text{ kPa}} \times 100\% \quad (4 - 3)$$

4. Calculation of the desired saturator outlet flow rate:

$$F_{s-out}^d = \frac{F_c^d}{\frac{C_{sat}^i}{100\%}}; \quad (4 - 4)$$

5. Calculation of the desired saturator inlet flow rate (to be set by MFC 4 controller):

$$F_{s-in}^d = F_{s-out}^d - F_c^d \quad (4 - 5)$$

6. Calculation of the desired dilutant flow rate (to be set by MFC 3 controller):

$$F_{dil}^d = F_{He,total}^d - F_{s-in}^d \quad (4 - 6)$$

It is important to note that, if we set the flow rates equal to calculated values to obtain a certain concentration of an adsorbate, the temperature inside the saturator will be different from that used in calculations. Therefore, correction of the obtained concentration needs to be made. Assume that, after setting the gas flows, the temperature becomes  $T_{sat}^{i+1}$  with the corresponding vapor pressure denoted as  $P_{sat}^{i+1}$ . Then Algorithm 2 can be used to solve the reverse task – to determine a real concentration of an adsorbate in gas phase. The steps of the Algorithm are shown below:

1. Calculation of an actual adsorbate concentration in gas phase inside the saturator:

$$C_{sat}^{i+1} \times 100\% \quad (4 - 7)$$

2. Calculation of the actual flow rate of pure adsorbate:

$$F_c^a = \frac{C_{sat}^{i+1}}{100\%} \times \frac{F_{s-in}^s}{1 - F_{s-in}^s} \quad (4 - 8)$$

3. Calculation of the actual total flow rate:

$$F_{total}^a = F_c^a + F_{s-in}^s + F_{dil}^s \quad (4 - 9)$$

4. Calculation of the actual concentration of adsorbate in gas phase inside TEOM:

$$C_{TEOM}^a = \frac{F_c^a}{F_{total}^a} \times 100\% \quad (4 - 10)$$

Calculated values of  $C_{TEOM}^a$  were used to obtain adsorption isotherms.

#### 4.3.4. Procedure of Analysis

Precisely weighted amount of a catalyst sample (approximately 6.5 mg) was loaded into the tapered element and placed between two pieces of quartz wool. Small amount of the sample was required to form a thin layer, thus minimizing concentration gradients within the sample bed. After isolation of the sample and TEOM lines, flow rates of carrier gas and purge gas (helium was used) were set by pre-calibrated flow controllers MFC 1 and MFC 2 equal to 100 cc/min and 50 cc/min, respectively. Temperatures of TEOM preheating zone and main heating zone were equal to 200°C. After 1 hour, temperature of the main heating zone was lowered to the temperature of analysis – 120°C. The saturator was filled with liquid model compound at room temperature (in case of acetaldehyde, the saturator was cooled in a freezer prior to loading) and immersed into a water-antifreeze bath. Water bath temperature was set different for each compound, as shown in Table 4-4. All gas lines of TEOM were heated by heating tapes wrapped around them to avoid sample condensation, when the saturator was operated at temperatures above ambient, i.e. in case of cyclohexanone, furfural, anisole, and water. Temperatures of the lines were set equal to 80-100°C.

Adsorption studies at different concentrations of a particular adsorbate were performed in a single run. Concentration was increased stepwise starting with the lowest value of 1% and was

kept constant until equilibrium at a particular step is attained. Gas flow rates were calculated following the algorithm described above (Figure 4-11). Tables of flow values with respect to each compound are shown in Appendix D.

A model compound was introduced into the tapered element for analysis only after the baseline became stable and at least 30 min after any alteration of the MFC4 flow to ensure attainment of vapor-gas equilibrium inside the saturator. Adsorption of a compound at a particular gas concentration was assumed to be complete when the baseline did not change with time. It is important to note that for some compounds, such as acetone and anisole, baseline kept changing even after 10 hours of the experiment, indicating that equilibrium was not reached. In those cases, quasi-equilibrium state was assumed, if a mass of the sample changed by less than  $10^{-5}$  g after 2000 s. Upon attainment of sorption equilibrium, temperature of the saturator contents was recorded to be used in calculation of actual adsorbate concentration in gas phase using Algorithm 2. Calculated adsorbate concentrations are shown in Appendix D.

It is important to note that, upon increase of adsorbate concentration in a single experiment run, the flow rate through the saturator (MFC3) varied as well. As a result, equilibrium between gas and liquid phase in the saturator was disturbed. Consequently, the desired values of adsorbate concentrations in gas phase were not achieved immediately, except for 1% concentration. To avoid influence of disturbed vapor-phase equilibrium on time-resolved adsorption measurements, we have not used data obtained at concentrations greater than 1 % to study adsorption kinetics. Instead, adsorption data obtained at those concentrations were used to obtain adsorption isotherms, since long times to attain equilibrium between the sample and an adsorbate ensure equilibrium in saturator.

As an example, a mass change profile for adsorption of acetaldehyde on RuCMS800-2 sample is shown in Figure E-1 of Appendix. Concentration of acetaldehyde varied from 1% to 24%.

It is well known [49] that the mass change registered by TEOM is not solely an effect of adsorption on sample pores. The mass change may also result from adsorption of a compound on outer surface of sample particles, on tapered element itself, and also may be caused by differences in carrier gas densities at different adsorbate concentrations. To account for these effects, for each adsorbate we carried out blank experiments involving non-porous quartz particles. To ensure that the outer particle surface is approximately the same as the surface of tested catalyst particles, quartz and catalyst particles used in TEOM were prepared having the same size – 20-32  $\mu\text{m}$ . In addition, difference in densities of quartz and a CMS material was taken into account to guarantee that the volume of a quartz bed inside the tapered element is equal to the volume of a tested sample. The density of PFA-derived carbon molecular sieves is approximately 1.5  $\text{g}/\text{cm}^3$ [28] versus 2.203  $\text{g}/\text{cm}^3$  for quartz. Accounting for density differences, the amount of quartz equivalent to 6.4 mg of RuCMS800-2 is  $6.4 \times \frac{2.203}{1.5} = 9.4$  mg.

Obtained “mass versus time” dependence for adsorption of acetaldehyde on quartz is shown in Figure E-2 of Appendix. One can see that side effects cause significant change in mass that may distort the real adsorption data. To eliminate this influence, quartz adsorption profiles were subtracted from catalyst adsorption data. The resulting curves were used to obtain equilibrium isotherms. As an example, adsorption isotherms of acetone and acetaldehyde on quartz particles and the samples RuCMS800-2 and RuCMS1000-2 are shown in Appendix F. Adsorption versus time profiles for various components are shown in Appendix G.

All equilibrium adsorption values obtained in TEOM measurements were normalized to account for minor variations in sample loadings (see Appendix H).

#### 4.3.5. Data Analysis

Adsorption isotherms for RuCMS800-2 and RuCMS1000-2 catalysts normalized to the sample weight of 10 mg are shown in Figure 4-12 and Figure 4-13, respectively.

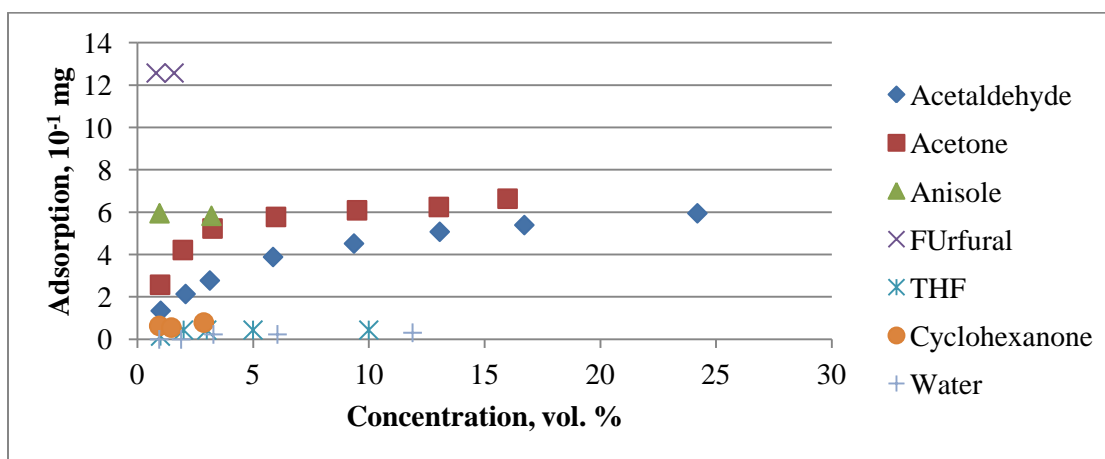


Figure 4-12: Adsorption isotherms for RuCMS800-2; temperature 120 °C, pressure 1 atm, normalized sample weight 10 mg, particle size 20-32 μm



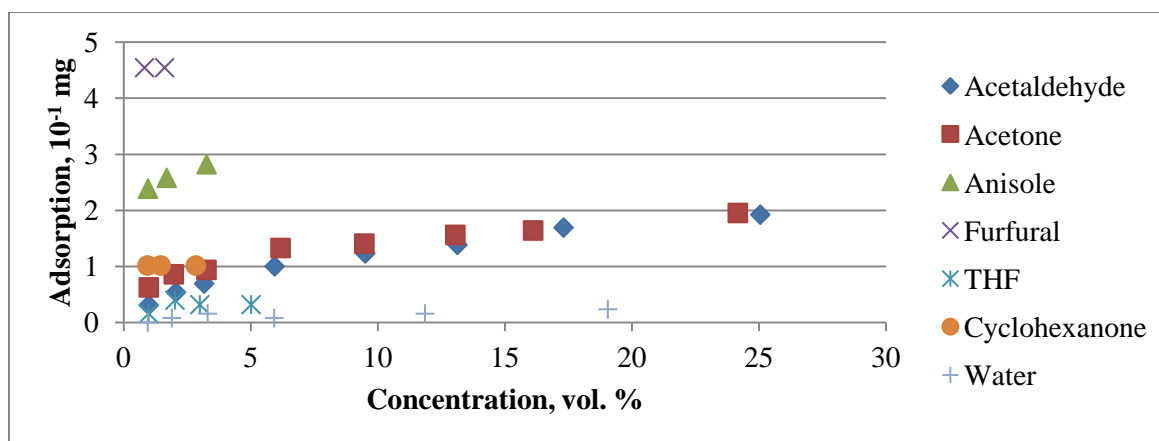


Figure 4-13: Adsorption isotherms for RuCMS1000-2; temperature 120 °C, pressure 1 atm, normalized sample weight 10 mg, particle size 20-32 μm

Adsorption isotherms indicate that there are significant differences in uptake of various compounds on the tested catalysts. Although these differences may certainly follow from limited accessibility of pores to certain compounds, i.e., molecular sieve effect, other factors that can lead to the same result must be taken into consideration. Seemingly, three factors can influence compound intake:

- 4.1. Different accessibility of pores with respect to various compounds;
- 4.2. Differences in adsorbate-adsorbent interactions;
- 4.3. Differences in adsorbate-adsorbate interactions within pores expressed as differences in densities.

In order to prove that it is the molecular sieve effect that explains this adsorption behavior, factors 2 and 3 must be ruled out or their influence at least must be taken into account.

To eliminate the effect of different densities of adsorbates on mass intake, adsorption needs to be expressed in terms of volume intake. In fact, adsorbed volume has more direct relation to molecular sieving compared to adsorbed weight, since it indicates the pore volume

filled with an adsorbate at its particular concentration in gas phase, and hence pore accessibility. To calculate adsorption volumes, the state of adsorbates inside micropores and their densities need to be estimated. The common assumption [58] is that an adsorbed compound behaves as a highly compressed liquid with density equal to density of the corresponding bulk liquid at the temperature of adsorption. In our case, liquid densities at 120°C need to be determined.

Assumption that properties of adsorbate inside the pores resembles those of bulk liquid, needs to be taken with caution [59]. On the one hand, it is feasible for compounds with boiling points greater than the adsorption temperature (furfural, anisole, cyclohexanone) or close to adsorption temperature (water), and therefore table density values or equations of state can be used in calculations. On the other hand, for highly volatile compounds, such as acetaldehyde, acetone and THF, deviations in density of a liquid inside pores from its value in a bulk state may arise. To account for these deviations, Dubinin [59] proposed to find a density of a micropore content by linear interpolation between boiling point density and critical point density:

$$\rho_D = \rho_{bp} - \frac{\rho_{bp} - \rho_{cp}}{T_{cp} - T_{bp}} \times (T_{TEOM} - T_{bp}) \quad (4 - 11)$$

It is important to note that this method provides good accordance with experimental data, if the critical density value is calculated based on molar weight of the compound and Van der Waals (V-d-W) constant b as follows:

$$\rho_{cp} = \frac{M}{b} \quad (4 - 12)$$

Constant b can be found from critical temperature and pressure:

$$b = \frac{RT_{cp}}{8P_{cp}} \quad (4 - 13)$$

We calculated liquid densities of compounds in two ways – as linear interpolation between two density values, and by using PRSV Equation of State. Results are shown in Tables 4-5 and 4-6:

Table 4-5: Properties of adsorbates and calculated micropore liquid densities (Dubinin approach)

Compound	Boiling point, °C	Critical point, °C	Density at b.p., kg/m <sup>3</sup>	Critical density, kg/m <sup>3</sup>	Corrected density, kg/m <sup>3</sup>
Acetaldehyde	20	183	772	518	616.1
Acetone	56	235	745	528	667.2
THF	66	268	833	666	788.2
CO <sub>2</sub>	-78	31	1245	1028	1090

Table 4-6: Densities calculated from PRSV model versus densities estimated on the basis of Dubinin's approach

Compound	PRSV Density, kg/m <sup>3</sup>	Dubinin's corrected density, kg/m <sup>3</sup>
Acetaldehyde	618.2	616.1
Acetone	662.9	667.2
Anisole	893.9	-
Furfural	1021	-
THF	766.1	788.2
Cyclohexanone	845.6	-
Water	930.5	-

Based on calculations, densities obtained by two methods do not differ significantly except for THF. Following Dubinin's recommendations [59], densities of acetaldehyde, acetone,

and THF were calculated using the linear interpolation, whereas densities of anisole, furfural, and cyclohexanone were estimated by PRSV equation of state. The TEOM mass intake values were divided by corresponding densities, and the obtained adsorption volumes are plotted versus concentrations for the catalysts RuCMS800-2 and RuCMS1000-2 in Figures 4-14 and 4-15, respectively.

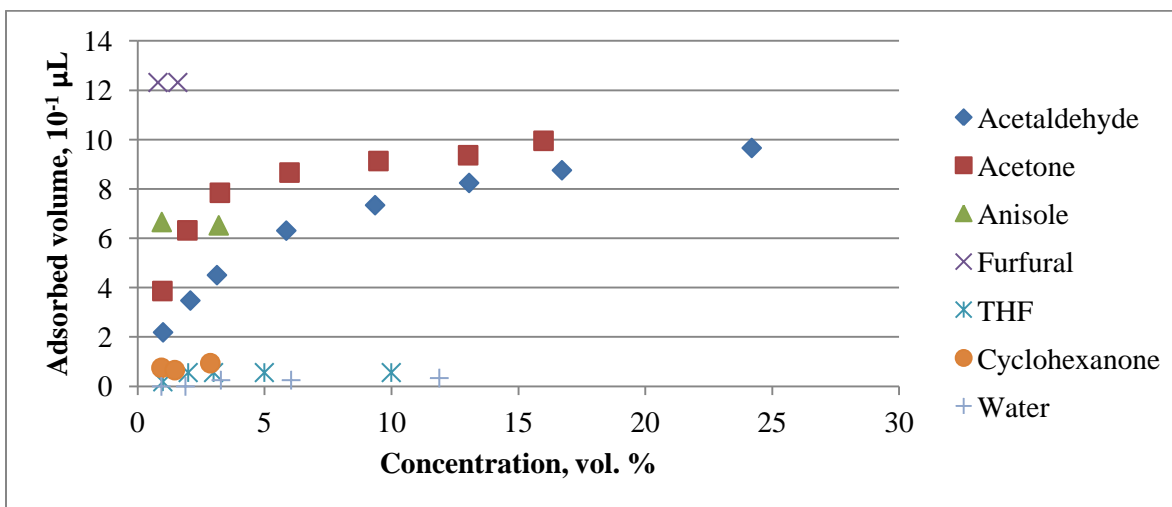


Figure 4-14: Adsorption isotherms for RuCMS800-2 (volume units)

The experimental TEOM data indicates that acetaldehyde, acetone, furfural, and anisole adsorb in relatively high amounts on RuCMS800-2 at various concentrations, in sharp contrast to adsorption of cyclohexanone and tetrahydrofuran. In addition, adsorption of water is negligible at low concentrations used, in agreement with literature data [27]. The extremely low water intake is attributed to low polarizability of water molecules and their propensity to form bulky clusters (H<sub>2</sub>O)<sub>5</sub>.

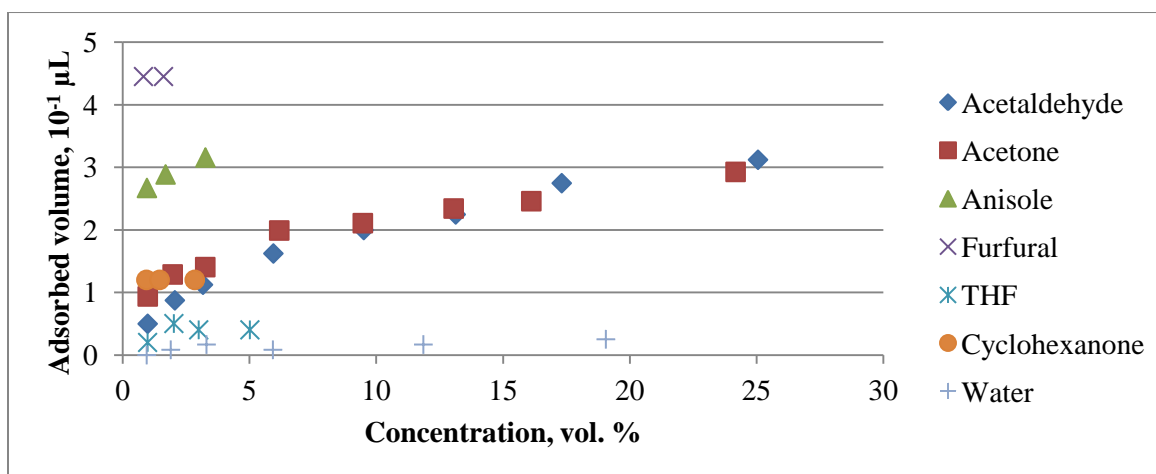


Figure 4-15: Adsorption isotherms for RuCMS1000-2 (volume units)

In order to provide a plausible explanation for observed adsorption trends in terms of the molecular sieve properties of the catalyst, we took two factors into account: differences in pore accessibility, which is a function of critical size of probe molecules; and differences in interaction between an adsorbate and carbon support. To estimate pore accessibility, a critical molecular size equal to a minimum dimension (thickness) of a molecule was assumed, since the micropores present in polyfurfuryl alcohol-derived molecular sieves possess slit-like structure as known from the literature [28]. To account for interactions between a probe molecule and a support, polarizabilities of adsorbate molecules were determined as the prevailing factor governing non-specific interaction between an adsorbate molecule and non-polar or slightly polar carbon support [27]. It was assumed that polarity of the carbon molecular sieve were negligible, since the carbonization temperature used during sample preparation were sufficient to remove the majority of carboxylic and hydroxylic groups that are known to account for specific interactions between a carbon sorbent and polar adsorbates [27].

Polarizabilities calculated with MARVIN software, minimum dimensions of molecules and adsorption capacities of RuCMS800-2 catalyst are shown in Table 4-7. Based on this, we conclude that adsorption of molecules with minimum dimensions of 3.4-4.1 Å was favored over species that possess minimum dimension greater than 5.3 Å.

Table 4-7. Polarizabilities, minimal dimensions, and adsorption capacities for various probe molecules

Adsorbate	Min dimension, Å	Polarizability	1% capacity for Ru-CMS-800, µL	3.2% capacity for Ru-CMS-800, µL
<b>Furfural</b>	<b>3.4</b>	<b>8.87</b>	<b>0.81</b>	-
<b>Anisole</b>	<b>4.09</b>	<b>11.81</b>	<b>0.43</b>	
<b>Acetone</b>	<b>4.09</b>	<b>6.4</b>	<b>0.25</b>	<b>0.5</b>
<b>Acetaldehyde</b>	<b>4.13</b>	<b>4.48</b>	<b>0.14</b>	<b>0.28</b>
Cyclohexanone	5.29	11.15	0.05	0.06
THF	5.38	8.14	0.01	0.04
Water	Clusters	1.51	0	0.01

To prove that it was molecular sieve effect that was responsible for an observed trend rather than differences in polarizability, we considered an anisole-cyclohexanone pair with similar polarizabilities. We would therefore expect similar adsorption properties in the absence of molecular sieve effect. However, the equilibrium adsorption of cyclohexanone at 1 mol. % concentration in the gas phase was almost an order of magnitude lower than that of anisole. Such a remarkable difference is clearly due to differences in minimum molecular dimensions of the molecules (4.1 Å for anisole and 5.3 Å for cyclohexanone) resulting in the molecular sieve effect by the support. Based on adsorption behavior, we conclude that the carbon molecular sieve support effectively functions as a 5Å-molecular sieve, in agreement with reported data on polyfurfuryl alcohol-derived carbon molecular sieves [37].

Differences in adsorption of adsorbates with a similar minimal dimension of 4.1 Å (acetaldehyde, acetone, anisole) were explained in terms of differences in polarizabilities. According to Table 2, polarizability increases from acetaldehyde to acetone and then anisole. Higher polarizability results in a stronger non-specific interaction between an adsorbate molecule and a carbon support, and possibly between the adsorbate molecules yielding more densely packed structure within micropores. Subsequently, adsorption capacity becomes greater for more polarizable molecules. Despite apparent structural and functional differences of adsorbates, polarizability is the only parameter that could explain such behavior. Carboxylic and hydroxylic functional groups that could account for specific interactions of a carbon surface are not stable at the temperature of 800 °C used at the carbonization stage of sieve preparation [27, 60]. Therefore, due to the lack of carboxylic and hydroxylic groups in the micropores of a carbon molecular sieve, specific molecular interactions between the adsorbate molecules and the support are not expected.

It is important to note that appropriate soaking temperature during the last catalyst preparation step is crucial for synthesis of a material possessing desirable molecular sieve properties. Increase in this temperature from 800 to 1000°C results in tremendous decrease in adsorption capacities and loss of molecular sieve adsorption selectivity of the catalyst (Figure 4-15).

#### **4.4. Determination of ruthenium content in RuCMS800-2 catalyst**

Ruthenium content in RuCMS800-2 was determined using ICP-AES spectrometer (Horiba Jobin Yvon JY 2000). The catalyst was dissolved in aqua regia using 23 ml acid dissolution bomb Parr 4749 with Teflon lining, capable to withstand pressures up to 1800 psi. 52.1 mg of the catalyst was loaded into the bomb along with aqua regia prepared from 6 ml of concentrated hydrochloric acid and 2 ml of nitric acid. Dissolution was performed at 200°C for 24 hours. As a result, the catalyst was completely dissolved in aqua regia. The solution was transferred into a volumetric flask and brought to the volume of 50 ml by dilution with water. Then it was analyzed by ICP along with five calibration solutions with ruthenium concentrations ranging from 2.855 µg/ml to 45.68 µg/ml. The solutions for calibration were prepared from the purchased ruthenium calibration standard with concentration of 1005 µg/ml. Calibration curve is shown in Appendix I. ICP showed that ruthenium concentration in the analyzed solution is 21.8 µg/ml. Thus, overall ruthenium amount in the catalyst sample is 1.0922 mg, equivalent to **ruthenium content of 2.1%**.

#### **4.5. Chemisorption Measurements**

To test the ability of the synthesized catalyst to catalyze hydrogenation reactions, we investigated accessibility of ruthenium nanoparticles by means of hydrogen chemisorption. Measurements were carried out using AutoChem 2910 apparatus. Prior to measurements, catalyst sample was treated at 200°C for 60 minutes in an argon flow to remove adsorbed water and air from the pores. After thermal treatment, the sample was cooled to 30 °C and underwent temperature-programmed reduction (TPR) in 10.3% H<sub>2</sub>-Ar flow. TPR is aimed to reduce



ruthenium oxides that may occur in the sample due to contact of the sample with air, as preliminary TPR results showed (see Section 3.3). The final TPR temperature was set equal to 120°C. The chosen temperature was sufficient to remove oxides from the sample, since it is known that reduction of ruthenium oxides typically occurs at lower temperatures – 80-100°C. For TPR, the sample was heated to 120°C at the rate of 5°/min, and the final temperature was maintained for 30 minutes. After cooling the sample, chemisorption analysis was performed at 30°C.

Chemisorption results for various samples are shown in Table 4-8. Chemisorption reveals that the amount of hydrogen adsorbed on RuCMS800-2 is low – 0.065 ml per 1 gram of the material. It corresponds to metallic dispersion of 1.4% and average Ru particle diameter of 96 nm. Since TEM analysis of RuCMS800-2 showed previously that ruthenium particles have diameters less than 3 nm (Section 4.2), it is evident that the majority of nanoparticles are inaccessible to hydrogen molecules. This result is in disagreement with published data for platinum nanoparticles encapsulated in PFA-derived CMS. In contrast to our results, 3-5 nm platinum nanoparticles adsorb amount of hydrogen equivalent to 15 nm average particle diameter [35].

To explain low values of hydrogen intake, we assumed that it is a result of existing restrictions in the pores that prevent hydrogen chemisorption. This hypothesis seemed to be reasonable, since it is known that ruthenium supported on carbon demonstrates lower H:Ru ratios(0.3-0.8) [61, 62] than pure metallic ruthenium (H:Ru = 1) [63], possibly due to contamination of particle surfaces by carbon hydrogen surface complexes that were formed on poorly organized carbon surfaces by hydrogen spillover and reverse diffusion to the metal surface during chemisorption [62]. In order to clean particle surface, it was suggested to perform TPR at temperatures up to 470°C [62].

Table 4-8: Chemisorption results

Sample	TPR final temperature	Temperature of chemisorption	Adsorbed volume of H <sub>2</sub> , ml/g	Ru particle diameter, nm	Metallic dispersion, %
RuCMS800-2	120	30	0.065	96	1.4
RuCMS800-2	470	30	0.069	92	1.5
RuCMS800-2	470	120	0.041	152	0.9
RuCMS800-1	470	30	0.018	324	0.4
RuCMS800-1 (after oxidation)	470	30	0.163	36.6*	3.7*
RuCMS800-2(2)	470	30	Negligible	-	-
RuCMS800-2(2) (after oxidation)	470	30	0.041	152*	0.9*
<b>RuCMS800-3</b>	<b>120</b>	<b>30</b>	<b>0.209</b>	<b>28.6*</b>	<b>4.7*</b>

\* - Ru content was assumed 2 wt. %

Prior to chemisorption, we heated the sample to 470°C at the heating rate of 10°/min in a H<sub>2</sub>-Ar atmosphere. The final temperature was maintained for 240 minutes. Then H<sub>2</sub>-Ar gas mixture flow was replaced by pure argon, and the sample was kept at 470°C for additional 120 minutes to desorb any remaining hydrogen. High temperature TPR, however, did not result in major improvements of chemisorption results – calculated average particle diameter is 92 nm.

In order to explain low chemisorption values, our next assumption was that it could be due to slow diffusion of hydrogen molecules within micropores. According to preliminary

hydrogenation experiments of guaiacol, Ru nanoparticles of RuCMS800-1 were apparently accessible to hydrogen at 180°C. To remove possible diffusion limitations, we performed H<sub>2</sub> chemisorption on RuCMS800-2 at 120°C. We found that the amount of adsorbed hydrogen at 120°C was even lower than at 30°C, possibly due to shift in adsorption equilibrium toward gas phase, in accordance with La Chatelier's principle.

For comparison, we performed similar H<sub>2</sub> chemisorption measurements for RuCMS800-1 catalyst that showed activity in hydrogenation reactions. Despite high hydrogenation activity, chemisorption measurement indicated that the average ruthenium particle diameter is 323 nm. Since hydrogenation and chemisorption studies were performed with the 6 month interval, such discrepancy in results can be due to catalyst aging under exposure to air. In support of aging hypothesis, RuCMS800-2(2) catalyst, which was prepared from a crosslinked polymer composite stored for 1 year, showed negligible hydrogen chemisorption in contrast to RuCMS800-2 synthesized from the same polymer composite, but one year earlier.

At this point we can conclude that accessibility of ruthenium nanoparticles to hydrogen molecules in synthesized CMS-based catalysts is low. Possible catalyst aging occurs upon catalyst exposure to air, further decreasing its hydrogen capacity.

It is known that accessibility of metallic nanoparticles encapsulated in CMS support can be improved by oxidative treatment at elevated temperatures [35]. To make ruthenium nanoparticles more accessible, we introduced additional oxidation step in chemisorption procedure. Prior to TPR at 470°C, the catalyst sample was kept in 1%O<sub>2</sub>-He flow for 60 minutes at 30°C to become saturated with oxygen. The sample was gradually heated at the rate of 2°/min to 200°C held for 30 minutes. The oxygen-containing flow was then replaced with the helium flow, and the sample was cooled to 30°C, followed by reduction and chemisorption steps. RuCMS800-1 sample was

tested, demonstrating an order of magnitude increase in hydrogen chemisorption after prior oxidative treatment. Similarly, RuCMS800-2(2) sample also shows increased accessibility of nanoparticles after oxidation (Table 4-8). Clearly, oxidative treatment is an effective method to make ruthenium nanoparticles more accessible to H<sub>2</sub>.

#### **4.6. Brief Remarks About the Third Generation of the Catalyst**

The third generation of the catalyst denoted as RuCMS900-3 demonstrates much better chemisorption characteristics, as well as shows improved pore size distribution.

In preparation method of the new generation of the catalyst, several changes were made. First of all, reduction stage was performed at 140-160°C instead of 180-200°C so that volatile reduction products – acetylacetone and furfural – remained in the liquid phase during a reflux. Second improvement was that at the polymerization step, oxalic acid was added in a powdered form rather than as an aqueous solution. It allowed us to completely eliminate formation of two-phase system and hence to create homogeneous conditions in the mixture during the synthesis. The third modification was elimination of the grinding step prior to carbonization, so that the polymer composite was not exposed to air before the final thermal treatment. During carbonization, temperature of a cross-linked CMS precursor sharply increased to 900°C and then maintained for 4 hours. After carbonization, the catalyst was ground to particles 64-106 μm in size.

We performed H<sub>2</sub> chemisorption on RuCMS800-3 catalyst sample at 30°C with preliminary reduction of the sample at 120°C. Obtained results suggest that the newly synthesized sample is capable of adsorbing the highest hydrogen volume among all tested

catalysts – 0.209 ml per 1 gram of a catalyst. This is equivalent to ruthenium particle size of 28.6 nm and dispersion of 4.7%, assuming ruthenium content 2 wt. %.

We should note that the average particle size was calculated based on assumption that H:Ru ratio is unity. However, as we pointed out above, ruthenium supported on carbon demonstrates H:Ru ratios below unity during hydrogen chemisorption (typically 0.3-0.5). Accounting for low H:Ru ratio, average particle size in RuCMS800-3 material would be 10-15 nm, in agreement with published chemisorption data on CMS-based catalyst with encapsulated platinum nanoparticles [35].

Despite average nanoparticle diameters calculated from chemisorption data are greater than those observed by TEM, this discrepancy has plausible explanation in terms of the proposed “berries-in-muffin” catalyst structure. Assuming ruthenium nanoparticles encapsulated in CMS porous framework, only part of the surface area of a particle would be exposed to empty space inside the pores, whereas remaining part would be in contact with carbon layers of the support. Limited particle surface availability for hydrogen adsorption results in decreased chemisorption values and hence in overestimated diameter values. Thus, the difference of particle diameters supports “berries-in-a-muffin” structure of the catalyst.

The third generation ruthenium CMS-based catalyst also has much more uniform pore size distribution compared to synthesized catalysts of the first two generations. CO<sub>2</sub> and N<sub>2</sub> adsorption data reveal that mesopores do not exist in the material and the majority of micropores lie in the range of 5-7Å (Figure 4-16; total CO<sub>2</sub> pore volume 0.207 cm<sup>3</sup>/g, surface area 666 m<sup>2</sup>/g; N<sub>2</sub> adsorption at 77 K is negligibly small).

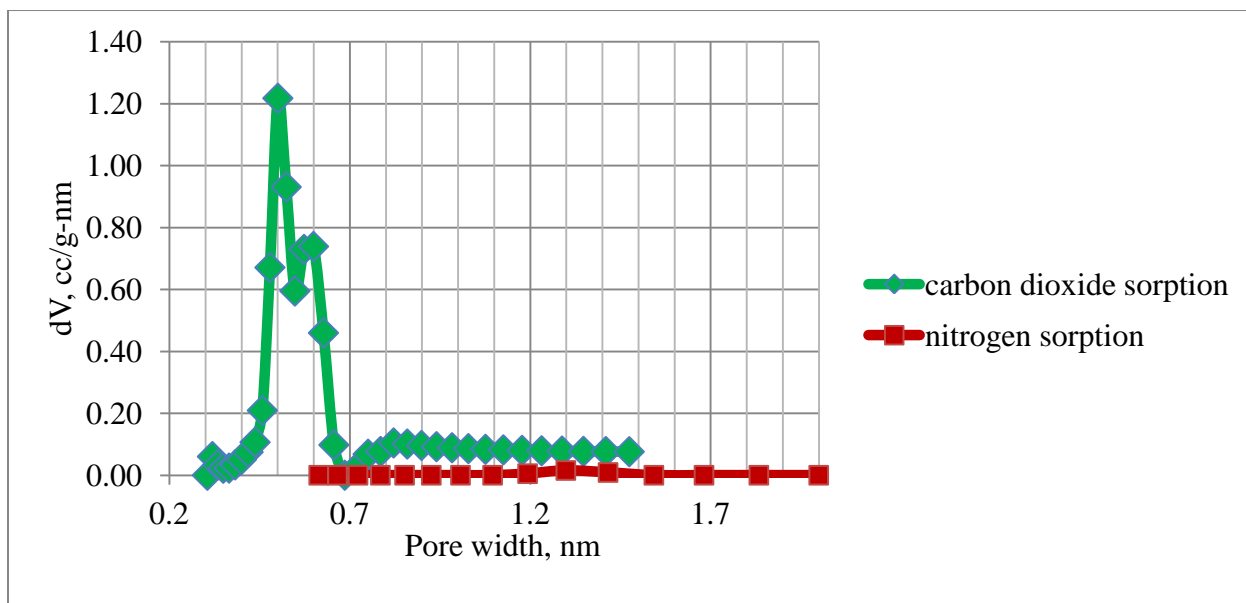


Figure 4-16: Pore size distribution of RuCMS900-3

## Chapter 5. Conclusions and Path Forward

This research resulted in several findings:

- Synthesized ruthenium-based CMS catalyst possesses desired properties: absence of mesopores; homogeneous pore size distribution with ultramicropores less than 8 Å size constituting 75% of micropore volume; uniformly distributed ruthenium nanoparticles of less than 3 nm in diameter within carbon framework;
- Prominent molecular sieve effect of the catalyst: catalyst pores with slit-like structure are accessible to molecules with minimum dimensions of 3.4-4.1 Å: furfural, acetaldehyde, acetone and anisole; water molecules as well as molecules of cyclohexanone and tetrahydrofuran (minimum dimension 5.3 Å) are unable to adsorb on catalyst pores effectively;
- Differences in adsorption of species with similar molecular sizes are explained in terms of differences in their polarizability;
- Effective H<sub>2</sub> chemisorption on the catalyst is a challenge that can be solved by using 3<sup>rd</sup> generation Ru-CMS catalyst and/or by oxidative treatment of the catalyst.

Based on the results, preliminary hypotheses can be made regarding catalyst structure and its behavior during chemical reactions. First, we note that despite the fact that cyclohexanone and tetrahydrofuran (having minimum dimensions of nearly 5.3 Å) do not adsorb effectively on the catalyst, CO<sub>2</sub> adsorption data suggest that 48 % of total pore volume lies above 5.3 Å and thus must be accessible to cyclohexanone and tetrahydrofuran. Since it seems this is not the case, we hypothesize that pores larger than 5 Å are surrounded by smaller pores and therefore inaccessible

to large molecules such as cyclohexanone. Based on this hypothesis, we propose the following scenarios to occur during chemical process:

1. If reactant molecules are  $>5 \text{ \AA}$ , they will not be able to enter majority of pores and therefore will not reach active metal surface and react. This may occur for pyrolytic lignin oligomers, carbohydrates, and water clusters, constituting  $>73 \text{ wt. \%}$  of pyrolysis oil (Table 1-1).
2. If reactant and product molecules are both  $<5 \text{ \AA}$ , reactants will enter pores easily and products will be easily removed. This is the case for light bio-oil oxygenates under hydrogenation conditions, such as hydroxyacetaldehyde (yields ethylene glycol) and hydroxyacetone (yields 1,2-propanediol), constituting up to  $16 \text{ wt. \%}$  of bio-oil [7]. In this scenario, small oxygenates can also be selectively reformed yielding hydrogen and  $\text{CO}_2$ .
3. If reactant molecules are  $<5 \text{ \AA}$  and product molecules are  $>5 \text{ \AA}$ , [as is expected for the hydrogenation of aromatic rings of small compounds such as anisole, phenols, and guaiacol constituting up to  $8 \text{ wt. \%}$  of bio-oil [7]], reactants will enter the pores, but only  $48 \text{ vol. \%}$  of micropores will be able to fit products of hydrogenation – cycloalkanes (minimum dimension of  $5.3 \text{ \AA}$ ). We hypothesize that the remaining  $52\%$  of pores will not participate in hydrogenation reactions providing product sieve selectivity. Since the pores bigger than  $5 \text{ \AA}$  are likely to be accessible only through pores less than  $5 \text{ \AA}$  based on differences in pore cutoff size and pore size distribution, there is a chance that some hydrogenation products will be unable to leave pores, resulting in pore blockage. Trapped cycloalkanes may also be eventually decomposed and hydrogenated to methane due to prominent methanation properties of ruthenium. Either case is unfavorable, and the catalyst must be improved in a way to hinder access of aromatic compounds to micropores, e.g., via oxidative treatment that would introduce oxygen-containing groups



on the surface, favoring adsorption of more polar compounds at the expense of aromatics [27].

Another challenge that must be addressed in designing optimal catalyst structure is restricted diffusion of reactants within ultramicropores that may severely reduce overall catalyst activity. One possible way to overcome this issue is to reduce sizes of micropore-containing segments of catalyst pellets by developing additional macro- and mesoporous structure. It was determined that addition of polyethylene glycols to initial mixture during preparation of a carbon molecular sieve from furfuryl alcohol would result in formation of mesopores at carbonization stage. These additional pores were shown to facilitate diffusion of nitrogen molecules at 77 K within micropores, which otherwise was extremely slow [50]. A possible alternative method of increasing mesopore and macropore volume is oxidative treatment of the sample; partial burning of chars was shown to increase meso- and macropore volume, while the volume of micropores remained constant [64].

As we concluded from comparison of chemisorption data, catalyst aging in air is a serious issue. Aging occurs, because during the carbonization stage of CMS synthesis, in which a polymer precursor is being treated at 800 °C in inert atmosphere, chemical bonds of heteroatoms with carbon atoms cleave, leaving free radicals on the surface of CMS. Upon exposure of CMS to air, those radicals result in irreversible chemisorption of oxygen molecules on the surface [65]. It has been shown that keeping the CMS membrane sample for several days in air result in decrease in membrane permeability [66]. It is evident that the similar aging mechanism in CMS-based ruthenium catalyst is likely to hinder diffusion of reactants and hydrogen to active metal sites, leading to decrease in hydrogen chemisorption and, consequently, in catalyst activity. To overcome this aging problem, the catalyst must be stored under inert atmosphere and/or modifications of final carbonization step must be made. It has been shown [67] that

carbonization under hydrogen rather than nitrogen results in partial aging inhibition due to partial passivation of active sites on the carbon surface. Moreover, passivation of active carbon sites is complete at 500 °C or even at 150 °C and 5.5 MPa in presence of platinum, which triggers hydrogen spillover from metal sites to CMS surface. Ruthenium in the CMS-based catalyst can play a role of platinum in catalyst stabilization, initiating hydrogen spillover and stabilizing CMS surface upon hydrogen treatment. Further research is necessary to determine the effectiveness of thrhydrogen treatment on catalyst stabilization.

Despite the foregoing limitations, the molecular sieve possesses one important property – its micropores are not accessible to water (Table 2). Consequently, it may act simultaneously as an adsorbent of organics from water-containing pyrolysis oils and as a hydrogenation catalyst, eliminating the need for water separation stage in pyrolysis oil upgrading process, thus making the overall process more effective. The use of the molecular sieve for reforming reactions is also possible, in which decomposition reactions yielding H<sub>2</sub> and CO may occur on active sites surrounded by ultramicropores, whereas subsequent water-gas shift reaction yielding additional amount of hydrogen will proceed at other reaction sites accessible to water, e.g., at ones located in mesopores.

We propose two possible ways of CMS-based catalyst usage in bio-oil upgrading process. First, CMS-based **reforming** catalyst can be placed right after pyrolysis unit before condensation of liquid products, so that light oxygenates can be reformed in gas phase. Advantage of this process modification is high temperature of the inlet flow favoring reforming reactions that usually occur above 300°C. To minimize residence time and thus to minimize side reactions of gas and coke formation, a CMS-based catalyst must be designed in such a way that the length of micropores surrounding active metal particles is very small to ensure sufficiently fast diffusion. Second possible technology of usage of CMS-based catalyst is stabilization of bio-oil by means

of mild liquid-phase **hydrogenation**. As it was pointed out above, ruthenium-based catalyst is active in hydrogenation of carbonyl compounds at temperatures as low as 80°C. Although use of regular ruthenium carbon-supported catalyst may give benefits for bio-oil stabilization, application of CMS-based ruthenium catalyst would hinder access of aromatic lignin molecules to active sites and prevent hydrogenation of aromatic rings, thus reducing hydrogen consumption. The possible drawback in this process alternative is simultaneous occurrence of aging reactions in bulk phase of bio-oil at elevated temperatures used in hydrogenation. Due to these reactions, bio-oil viscosity increase at 90°C is extremely high, reaching 300 cP/day [9]. In order to minimize negative effects of accelerated aging at elevated temperatures, “trade-off” in temperature and catalyst activity must be found. In other words, temperature must be sufficiently low for aging reactions to occur to the minimal extent, but sufficiently high to minimize residence time and provide the best catalyst performance.

## REFERENCES

1. Bhar, R. and B. Nikolova, *Oil prices and equity returns in the BRIC countries*. The World Economy, 2009. **32**(7): p. 1036-1054.
2. Taibi, E., D. Gielen, and M. Bazilian, *The potential for renewable energy in industrial applications*. Renewable and Sustainable Energy Reviews, 2011.
3. McKendry, P., *Energy production from biomass (part 1): overview of biomass*. Bioresource technology, 2002. **83**(1): p. 37-46.
4. Schröder, K.P. and R. Cannon Smith, *Distant future of the Sun and Earth revisited*. Monthly Notices of the Royal Astronomical Society, 2008. **386**(1): p. 155-163.
5. Naik, S., et al., *Production of first and second generation biofuels: A comprehensive review*. Renewable and Sustainable Energy Reviews, 2010. **14**(2): p. 578-597.
6. Devi, L., K.J. Ptasinski, and F.J.J.G. Janssen, *A review of the primary measures for tar elimination in biomass gasification processes*. Biomass and Bioenergy, 2003. **24**(2): p. 125-140.
7. Azeez, A.M., et al., *Fast Pyrolysis of African and European Lignocellulosic Biomasses Using Py-GC/MS and Fluidized Bed Reactor*. Energy & Fuels, 2010. **24**: p. 2078-2085.
8. Mullen, C.A., et al., *Bio-oil and bio-char production from corn cobs and stover by fast pyrolysis*. Biomass and Bioenergy, 2010. **34**(1): p. 67-74.
9. Diebold, J.P., I. Thermalchemie, and N.R.E. Laboratory, *A review of the chemical and physical mechanisms of the storage stability of fast pyrolysis bio-oils*2000: National Renewable Energy Laboratory Golden, CO.
10. Song, Q.H., et al., *Effective phase separation of biomass pyrolysis oils by adding aqueous salt solutions*. Energy & Fuels, 2009. **23**(6): p. 3307-3312.
11. Venderbosch, R., et al., *Stabilization of biomass-derived pyrolysis oils*. Journal of Chemical Technology and Biotechnology, 2010. **85**(5): p. 674-686.
12. Ingram, L., et al., *Pyrolysis of wood and bark in an auger reactor: Physical properties and chemical analysis of the produced bio-oils*. Energy & Fuels, 2007. **22**(1): p. 614-625.
13. Mohan, D., C.U. Pittman Jr, and P.H. Steele, *Pyrolysis of wood/biomass for bio-oil: a critical review*. Energy & Fuels, 2006. **20**(3): p. 848-889.
14. Speight, J.G., *The Chemistry and Technology of Petroleum*1999: Marcel Dekker.
15. Czernik, S. and A. Bridgwater, *Overview of applications of biomass fast pyrolysis oil*. Energy & Fuels, 2004. **18**(2): p. 590-598.
16. Elliott, D.C., *Historical developments in hydroprocessing bio-oils*. Energy & Fuels, 2007. **21**(3): p. 1792-1815.
17. Kim, T.S., et al., *The effect of storage duration on bio-oil properties*. Journal of Analytical and Applied Pyrolysis, 2012.
18. Wang, D., D. Montane, and E. Chornet, *Catalytic steam reforming of biomass-derived oxygenates: acetic acid and hydroxyacetaldehyde*. Applied Catalysis A: General, 1996. **143**(2): p. 245-270.
19. Pompeo, F., G. Santori, and N.N. Nichio, *Hydrogen and/or syngas from steam reforming of glycerol. Study of platinum catalysts*. International Journal of Hydrogen Energy, 2010. **35**(17): p. 8912-8920.
20. Hu, X. and G. Lu, *Investigation of the steam reforming of a series of model compounds derived from bio-oil for hydrogen production*. Applied Catalysis B: Environmental, 2009. **88**(3-4): p. 376-385.
21. Hu, X. and G. Lu, *Investigation of the effects of molecular structure on oxygenated hydrocarbon steam re-forming*. Energy & Fuels, 2009. **23**(2): p. 926-933.

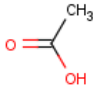
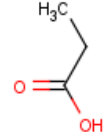
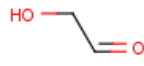
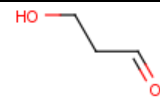
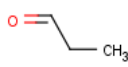
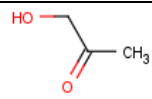
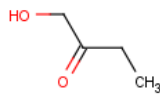
22. Gutierrez, A., et al., *Hydrodeoxygenation of guaiacol on noble metal catalysts*. Catalysis today, 2009. **147**(3-4): p. 239-246.
23. Perego, C. and A. Bosetti, *Biomass to fuels: The role of zeolite and mesoporous materials*. Microporous and Mesoporous Materials, 2011. **144**(1): p. 28-39.
24. Gayubo, A.G., et al., *Transformation of oxygenate components of biomass pyrolysis oil on a HZSM-5 zeolite. II. Aldehydes, ketones, and acids*. Industrial & engineering chemistry research, 2004. **43**(11): p. 2619-2626.
25. Vitolo, S., et al., *Catalytic upgrading of pyrolytic oils over HZSM-5 zeolite: behaviour of the catalyst when used in repeated upgrading-regenerating cycles*. Fuel, 2001. **80**(1): p. 17-26.
26. Wildschut, J., et al., *Hydrotreatment of fast pyrolysis oil using heterogeneous noble-metal catalysts*. Industrial & engineering chemistry research, 2009. **48**(23): p. 10324-10334.
27. Yang, R.T. and J. Wiley, *Adsorbents: fundamentals and applications*. 2003.
28. Foley, H.C., *Carbogenic molecular sieves: synthesis, properties and applications*. Microporous Materials, 1995. **4**(6): p. 407-433.
29. Webster, C.E., R.S. Drago, and M.C. Zerner, *Molecular dimensions for adsorptives*. Journal of the American Chemical Society, 1998. **120**(22): p. 5509-5516.
30. Tsai, W.T., et al., *Polycyclic aromatic hydrocarbons (PAHs) in bio-crudes from induction-heating pyrolysis of biomass wastes*. Bioresource technology, 2007. **98**(5): p. 1133-1137.
31. Fratini, E., et al., *SANS analysis of the microstructural evolution during the aging of pyrolysis oils from biomass*. Langmuir, 2006. **22**(1): p. 306-312.
32. Kaneko, K., *Specific intermolecular structures of gases confined in carbon nanospace*. Carbon, 2000. **38**(2): p. 287-303.
33. Fitzer, E. and W. Schäfer, *The effect of crosslinking on the formation of glasslike carbons from thermosetting resins*. Carbon, 1970. **8**(3): p. 353-364.
34. Koresh, J.E. and A. Sofer, *Molecular sieve carbon permselective membrane. Part I. Presentation of a new device for gas mixture separation*. Separation Science and Technology, 1983. **18**(8): p. 723-734.
35. Chen, H., et al., *Effect of hydrogen spillover on the hydrogenation of 1-hexene over diluted carbon molecular sieve supported Pt catalyst*. Catalysis today, 2007. **125**(3-4): p. 256-262.
36. Trimm, D. and B. Cooper, *The preparation of selective carbon molecular sieve catalysts*. J. Chem. Soc. D, 1970(8): p. 477-478.
37. Schmitt, J. and P. Walker, *Carbon molecular sieve supports for metal catalysts-II. Selective hydrogenation of hydrocarbons over platinum supported on polyfurfuryl alcohol carbon*. Carbon, 1972. **10**(1): p. 87-92.
38. Rajagopalan, R., et al., *Molecular sieving platinum nanoparticle catalysts kinetically frozen in nanoporous carbon*. Chemical communications, 2004(21): p. 2498-2499.
39. Kluson, P. and L. Cervený, *Selective hydrogenation over ruthenium catalysts*. Applied Catalysis A: General, 1995. **128**(1): p. 13-31.
40. Gagnon, J. and S. Kaliaguine, *Catalytic hydrotreatment of vacuum pyrolysis oils from wood*. Industrial & engineering chemistry research, 1988. **27**(10): p. 1783-1788.
41. Willis, A.L., et al., *Metal acetylacetonates as general precursors for the synthesis of early transition metal oxide nanomaterials*. Journal of Nanomaterials, 2007. **2011**.
42. Moreno-Castilla, C., et al., *Carbon as a support for catalysts--III glassy carbon as a support for iron*. Carbon, 1980. **18**(4): p. 271-276.

43. Wang, H. and J. Yao, *Use of poly (furfuryl alcohol) in the fabrication of nanostructured carbons and nanocomposites*. Industrial & engineering chemistry research, 2006. **45**(19): p. 6393-6404.
44. Mariwala, R.K. and H.C. Foley, *Evolution of ultramicroporous adsorptive structure in poly (furfuryl alcohol)-derived carbogenic molecular sieves*. Industrial & engineering chemistry research, 1994. **33**(3): p. 607-615.
45. Reimer, L., *Transmission Electron Microscopy*. Springer series in Optical Sciences (Springer-Verlag, 1993), third edn.
46. *Powder Tech Note 40*, Quantachrome Instruments.
47. *Porous Material Primers*, Quantachrome Instruments.
48. Hu, X., et al., *CO<sub>2</sub>-Filling Capacity and Selectivity of Carbon Nanopores: Synthesis, Texture and Pore-Size Distribution from Quenched-Solid Density Functional Theory (QSDFT)*. Environmental science & technology, 2011.
49. Gong, K., et al., *Tapered element oscillating microbalance (TEOM) studies of isobutane, n-butane and propane sorption in  $\beta$ - and  $\gamma$ -zeolites*. AIChE Journal, 2010. **56**(5): p. 1285-1296.
50. Lafyatis, D.S., J. Tung, and H.C. Foley, *Poly (furfuryl alcohol)-derived carbon molecular sieves: dependence of adsorptive properties on carbonization temperature, time, and poly (ethylene glycol) additives*. Industrial & engineering chemistry research, 1991. **30**(5): p. 865-873.
51. Higgins, J., et al., *Theoretical study of thermal decomposition mechanism of oxalic acid*. The Journal of Physical Chemistry A, 1997. **101**(14): p. 2702-2708.
52. Huang, S.Y., S.M. Chang, and C. Yeh, *Characterization of surface composition of platinum and ruthenium nanoalloys dispersed on active carbon*. The Journal of Physical Chemistry B, 2006. **110**(1): p. 234-239.
53. Huber, G.W., et al., *Aqueous-Phase Hydrogenation of Acetic Acid over Transition Metal Catalysts*. ChemSusChem, 2010. **2**: p. 1420-1424.
54. Su, F., et al., *Sandwiched ruthenium/carbon nanostructures for highly active heterogeneous hydrogenation*. Advanced Functional Materials, 2007. **17**(12): p. 1926-1931.
55. Li, N., et al., *Renewable gasoline from aqueous phase hydrodeoxygenation of aqueous sugar solutions prepared by hydrolysis of maple wood*. Green Chem., 2011. **13**(1): p. 91-101.
56. Domingo-Garcia, M., et al., *Determination of the micropore texture of some glassy carbons using molecular probes*. Langmuir, 1997. **13**(5): p. 1218-1224.
57. *A Property Methods and Calculations*, in *HYSYS 2004.2. Simulation Basis.*, AspenTech.
58. Huber, U., F. Stoeckli, and J.P. Houriet, *A generalization of the Dubinin-Radushkevich equation for the filling of heterogeneous micropore systems in strongly activated carbons*. Journal of Colloid and Interface Science, 1978. **67**(2): p. 195-203.
59. Dubinin, M., *The potential theory of adsorption of gases and vapors for adsorbents with energetically nonuniform surfaces*. Chemical Reviews, 1960. **60**(2): p. 235-241.
60. Giroux, L., J.P. Charland, and J. MacPhee, *Application of thermogravimetric Fourier transform infrared spectroscopy (TG-FTIR) to the analysis of oxygen functional groups in coal*. Energy & Fuels, 2006. **20**(5): p. 1988-1996.
61. Plomp, A.J., et al., *Particle size effects for carbon nanofiber supported platinum and ruthenium catalysts for the selective hydrogenation of cinnamaldehyde*. Applied Catalysis A: General, 2008. **351**(1): p. 9-15.
62. Kowalczyk, Z., et al., *An alkali-promoted ruthenium catalyst for the synthesis of ammonia, supported on thermally modified active carbon*. Catalysis Letters, 1997. **45**(1): p. 65-72.
63. Betta, R.A.D., *Measurement of ruthenium metal surface area by chemisorption*. Journal of Catalysis, 1974. **34**(1): p. 57-60.

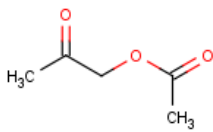
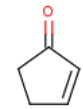
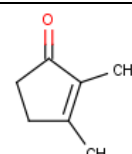
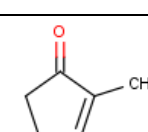
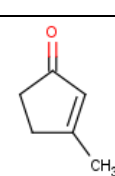
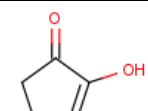
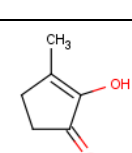
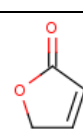
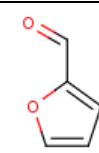
64. Aarna, I. and E.M. Suuberg. *Changes in reactive surface area and porosity during char oxidation*. 1998. Elsevier.
65. Menéndez, J.A., et al., *On the modification and characterization of chemical surface properties of activated carbon: in the search of carbons with stable basic properties*. Langmuir, 1996. **12**(18): p. 4404-4410.
66. Menendez, I. and A.B. Fuertes, *Aging of carbon membranes under different environments*. Carbon, 2001. **39**(5): p. 733-740.
67. Lagorsse, S., F. Magalhaes, and A. Mendes, *Aging study of carbon molecular sieve membranes*. Journal of Membrane Science, 2008. **310**(1): p. 494-502.

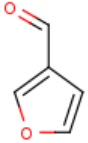
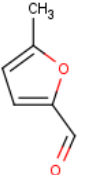
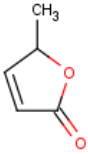
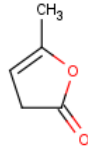
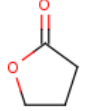
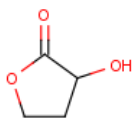
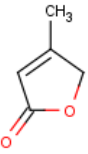
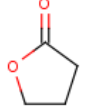
## APPENDIX A

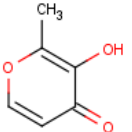
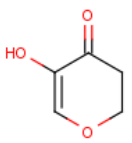
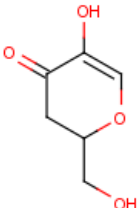
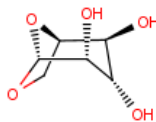
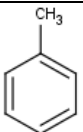
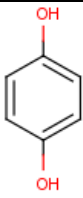
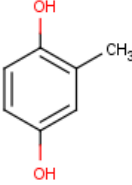
### Composition of corn cob-derived bio-oil [7]

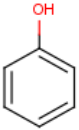
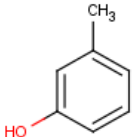
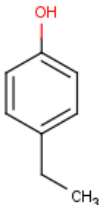
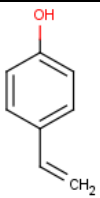
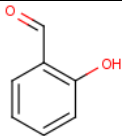
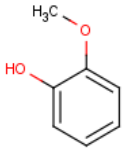
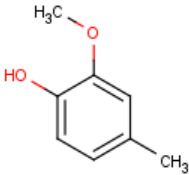
Compound	Structure	Determinant of thickness	Minimum dimension (Å)	Content in corn cob bio-oil
Acids				
acetic acid		Methyl group	4.1	8.5
propionic acid		Methyl group	4.1	0.6
Non-aromatic aldehydes				
Acetaldehyde, hydroxy-		Methyl group	4.1	5.1
propionaldehyde, 3-hydroxy		Methyl group	4.1	0.9
butandial or propanal		Methyl group	4.1	1.4
Non-aromatic ketones				
Hydroxyacetone		Methyl group	4.1	4.7
butanone, 1-hydroxy-2-		Methyl group	4.1	1.3

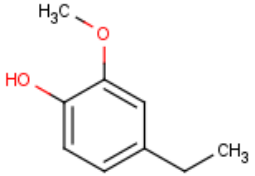
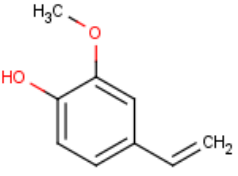
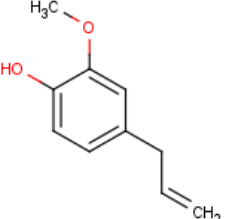
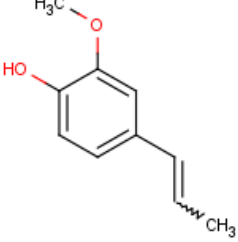
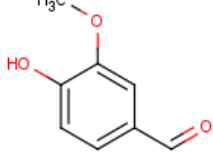
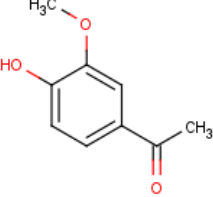


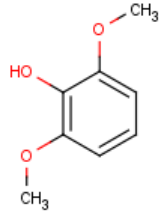
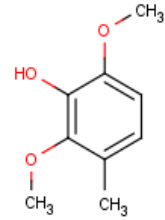
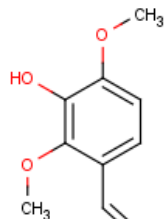
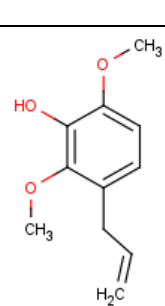
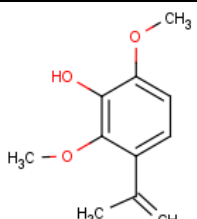
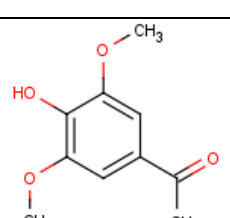
propanone, acetyloxy-2-		Methyl group	4.1	0.3
cyclopentene-1-one, 2-		Methyl group	4.1	0.4
cyclopentene-1-one, 2,3-dimethyl-2-		Methyl group	4.1	0.1
cyclopentene-1-one, 2-methyl-2-		Methyl group	4.1	0.2
cyclopentene-1-one, 3-methyl-2-		Methyl group	4.1	0.1
cyclopentene-1-one, 2-hydroxy-2-		Methyl group	4.1	1.9
cyclopentene-3-one, 2-hydroxy-1- methyl-1-		Methyl group	4.1	1.3
Furans				
furanone, 2(5H)-		Methyl group	4.1	0.6
furaldehyde, 2-		$\pi$ -system	3.4	1.0

furaldehyde, 3-		$\pi$ -system	3.4	0.1
furaldehyde, 5-methyl-2-		Methyl group	4.1	0.1
furan-2-one, 5-methyl-, (5H)-		Methyl group	4.1	0.1
furan-x-on, dihydro-x-methyl-		Methyl group	4.1	0.2
butyrolactone, $\gamma$ -		Methyl group	4.1	0.2
butyrolactone, 2-hydroxy-, $\gamma$ -		Methyl group	4.1	0.5
furan-2-one, 4-methyl-(5H)-		Methyl group	4.1	0.1
Lactone derivative		Methyl group	4.1	0.5

Pyrans				
Maltol		Methyl group	4.1	0.3
pyran-4-one, 3-hydroxy-5,6-dihydro-, (4H)-		Methyl group	4.1	0.9
pyran-4-one, 2-hydroxymethyl-5-hydroxy-2,3-dihydro-, (4H)-		Methyl group	4.1	0.1
Sugars		-	>5	3.4
Toluene		Methyl group	4.1	0.1
Catechols				
Hydroquinone		$\pi$ -system	3.4	0.2
benzenediol, methyl-		Methyl group	4.1	0.1

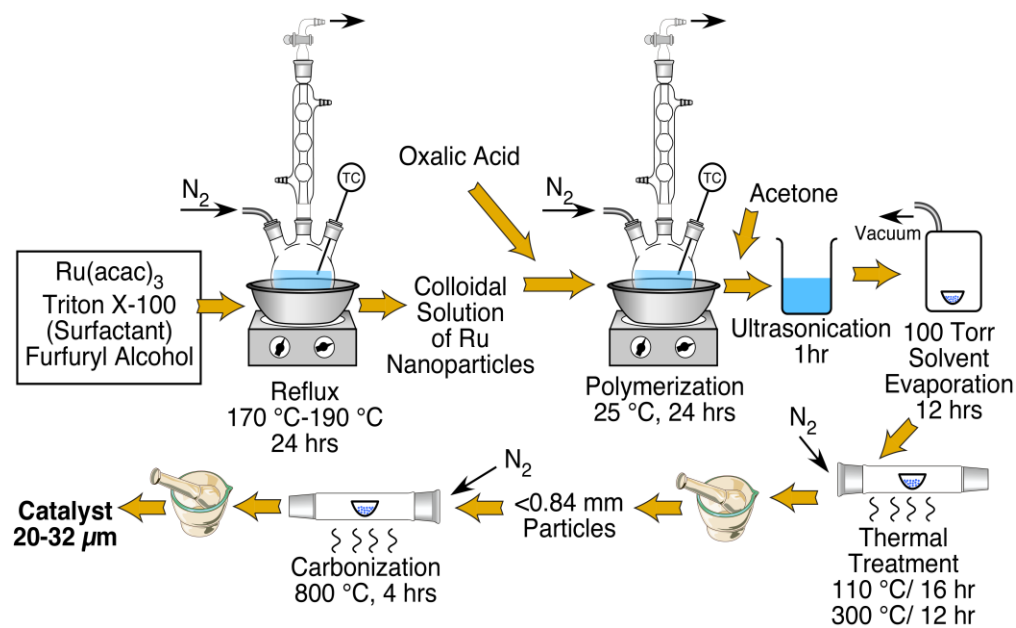
Lignin-derived phenols				
Phenol		$\pi$ -system	3.4	0.3
Cresols		Methyl group	4.1	0.3
phenol, 4-ethyl-		Methyl group	4.1	0.3
phenol, 4-vinyl-		$\pi$ -system	3.4	2.5
benzaldehyde, hydroxy-		$\pi$ -system	3.4	0.2
Guaiacols				
Guaiacol		Methyl group	4.1	0.5
guaiacol, 4-methyl-		Methyl group	4.1	0.2

guaiacol, 4-ethyl-		Methyl group	4.1	0.2
guaiacol, 4-vinyl-		Methyl group	4.1	1.7
Eugenol		Methyl group	4.1	0.1
Isoeugenol		Methyl group	4.1	0.3
Vanillin		Methyl group	4.1	0.3
Acetoguaiacone		Methyl group	4.1	0.1

Syringols				
Syringol		Methyl group	4.1	0.3
syringol, 4-methyl-		Methyl group	4.1	0.1
syringol, 4-vinyl-		Methyl group	4.1	0.2
syringol, 4-allyl-		Methyl group	4.1	0.1
syringol, 4-(1-propenyl)-		Methyl group	4.1	0.3
Acetosyringone		Methyl group	4.1	0.1

## APPENDIX B

### Catalyst Preparation Scheme



## APPENDIX C

### Details of Hydrogenation Experiments

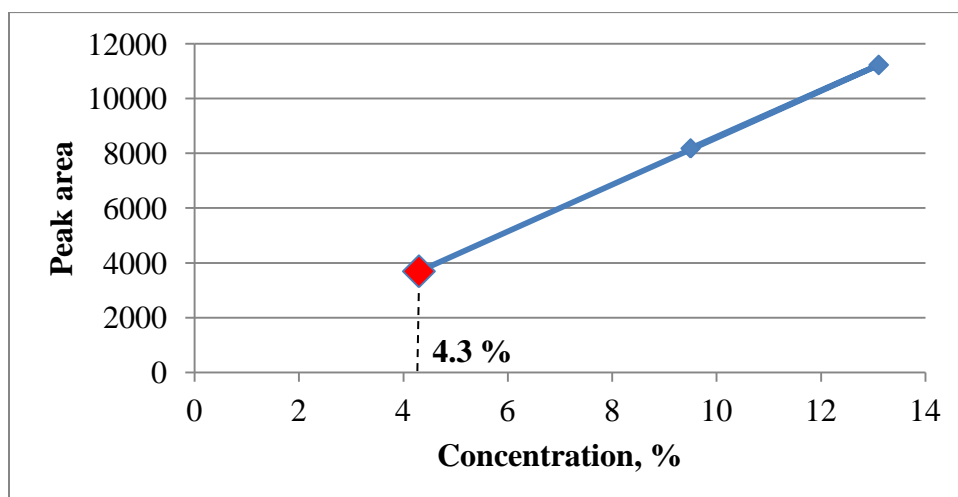


Figure C-1: Acetic acid calibration plot

From Figure C-1 it was found that concentration of acetic acid in the solution is 4.3 wt. %. If we remember that the initial volume of acetic acid solution loaded into the reactor was roughly 22 ml, and we used 9 ml of distilled water for washing, final concentration of unreacted acetic acid in the reactor is  $4.3 \times \frac{22+9}{22} = 6.1 \%$  (here, high accuracy of calculations was not required for preliminary hydrogenation experiments), corresponding to conversion of  $\frac{9.3-6.1}{9.3} \times 100\% = 34\%$ .

The chromatogram of products of acetic acid hydrogenation is shown in Figure C-2:

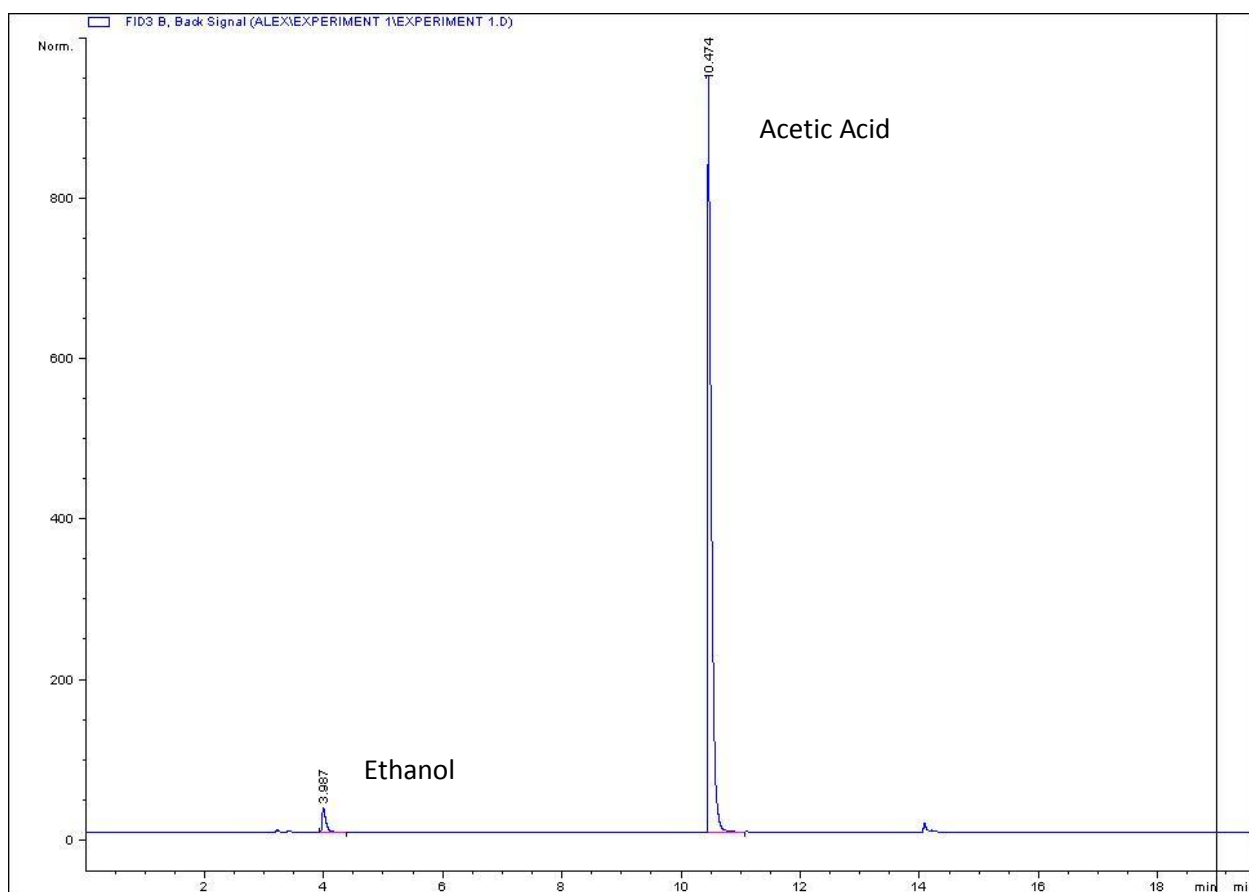


Figure C-2: Chromatogram of products of acetic acid hydrogenation on RuCMS800-1 catalyst



## APPENDIX D

### Acetaldehyde:

$$F_{total}^d = 100 \text{ cc/min}$$

$$T_{sat}^0 = -11.8 \text{ }^\circ\text{C}$$

$$P_{sat}^0 = 25.01 \text{ kPa}$$

$C_{TEOM}^d, \%$	$F_c^d, \text{ cc/min}$	$F_{He, total}^d, \text{ cc/min}$	$F_{s-out}^d, \text{ cc/min}$	$F_{s-in}^d, \text{ cc/min}$	$F_{dil}^d, \text{ cc/min}$
0.96	0.96	99.04	3.9	<b>3</b>	<b>96</b>
2	2	98	8.1	<b>6</b>	<b>92</b>
3.2	3.2	96.8	13.0	<b>10</b>	<b>87</b>
6	6	94	24.3	<b>18</b>	<b>76</b>
9.5	9.5	90.5	38.5	<b>29</b>	<b>62</b>
13.1	13.1	86.9	53.1	<b>40</b>	<b>47</b>
16.4	16.4	83.6	66.4	<b>50</b>	<b>34</b>
24.7	24.7	75.3	100	<b>75</b>	<b>0</b>

$C_{TEOM}^d, \%$	$F_{s-in}^s, \text{ cc/min}$	$F_{dil}^s, \text{ cc/min}$	$T_{sat}^a, \text{ K}$	$P_{sat}^a, \text{ kPa}$	$C_{sat}^a, \%$	$F_c^a, \text{ cc/min}$	$F_{total}^a, \text{ cc/min}$	$C_{TEOM}^a, \%$
0.96	<b>3</b>	<b>96</b>	-11.4	25.51	25.2	1.0	100	1.0
2	<b>6</b>	<b>92</b>	-10.7	26.4	26.0	2.1	100	2.1
3.2	<b>9</b>	<b>88</b>	-10.9	26.15	25.8	3.1	100	3.1
6	<b>17</b>	<b>77</b>	-11.1	25.89	25.5	5.8	100	5.8
9.5	<b>28</b>	<b>63</b>	-11.2	25.76	25.4	9.6	101	9.5
13.1	<b>38</b>	<b>48</b>	-11.1	25.89	25.6	13.0	99	13.2
16.4	<b>50</b>	<b>33</b>	-11.2	25.76	25.4	17.1	100	17.0
24.7	<b>75</b>	<b>0</b>	-12	24.76	24.4	24.3	99	24.4

### Acetone:

$$F_{total}^d = 100 \text{ cc/min}$$

$$T_{sat}^0 = 19.8 \text{ }^\circ\text{C}$$

$$P_{sat}^0 = 24.44 \text{ kPa}$$

$C_{TEOM}^d$ , %	$F_c^d$ , cc/min	$F_{He,total}^d$ , cc/min	$F_{s-out}^d$ , cc/min	$F_{s-in}^d$ , cc/min	$F_{dil}^d$ , cc/min
0.96	0.96	99.0	4.0	3.0	96.0
2	2	98.0	8.3	6.3	91.7
3.2	3.2	96.8	13.3	10.1	86.7
6	6	94.0	24.9	18.9	75.1
9.5	9.5	90.5	39.4	29.9	60.6
13.1	13.1	86.9	54.3	41.2	45.7

$C_{TEOM}^d$ , %	$F_{s-in}^s$ , cc/min	$F_{dil}^s$ , cc/min	$T_{sat}^a$ , K	$P_{sat}^a$ , kPa	$C_{sat}^a$ , %	$F_c^a$ , cc/min	$F_{total}^a$ , cc/min	$C_{TEOM}^a$ , %
0.96	3.0	96.0	20.2	25.0	24.7	1.0	100.0	1.0
2	6.0	92.0	20.2	25.0	24.7	2.0	100.0	2.0
3.2	10.0	87.0	20.1	24.9	24.6	3.3	100.3	3.2
6	18.0	76.0	19.9	24.7	24.4	5.8	99.8	5.8
9.5	30.0	61.0	19.8	24.6	24.2	9.6	100.6	9.5
13.1	41.0	46.0	19.7	24.4	24.1	13.0	100.0	13.0

**Anisole:**

$$F_{total}^d = 100 \text{ cc/min}$$

$$T_{sat}^0 = 58.7 \text{ }^\circ\text{C}$$

$$P_{sat}^0 = 3.24 \text{ kPa}$$

$C_{TEOM}^d$ , %	$F_c^d$ , cc/min	$F_{He,total}^d$ , cc/min	$F_{s-out}^d$ , cc/min	$F_{s-in}^d$ , cc/min	$F_{dil}^d$ , cc/min
1.0	1.0	99.0	29.6	<b>28.7</b>	<b>70.4</b>
1.7	1.7	98.3	51.7	<b>50.0</b>	<b>48.3</b>
3.2	3.2	96.8	100.0	<b>96.8</b>	<b>0.0</b>

$C_{TEOM}^d$ , %	$F_{s-in}^s$ , cc/min	$F_{dil}^s$ , cc/min	$T_{sat}^a$ , K	$P_{sat}^a$ , kPa	$C_{sat}^a$ , %	$F_c^a$ , cc/min	$F_{total}^a$ , cc/min	$C_{TEOM}^a$ , %
1.0	<b>29.0</b>	<b>71.0</b>	59.0	3.3	3.2	1.0	101.0	1.0
1.7	<b>50.0</b>	<b>48.0</b>	59.0	3.3	3.2	1.7	99.7	1.7
3.2	<b>97.0</b>	<b>0.0</b>	59.0	3.3	3.2	3.2	100.2	3.2

**Furfural:**

$$F_{total}^d = 100 \text{ cc/min}$$

$$T_{sat}^0 = 59.7 \text{ }^\circ\text{C}$$

$$P_{sat}^0 = 1.61 \text{ kPa}$$

$C_{TEOM}^d$ , %	$F_c^d$ , cc/min	$F_{He,total}^d$ , cc/min	$F_{s-out}^d$ , cc/min	$F_{s-in}^d$ , cc/min	$F_{dil}^d$ , cc/min
0.8	0.8	99.2	50.8	<b>50.0</b>	<b>49.2</b>
1.6	1.6	98.4	100.0	<b>98.4</b>	<b>0.0</b>

$C_{TEOM}^d$ , %	$F_{s-in}^s$ , cc/min	$F_{dil}^s$ , cc/min	$T_{sat}^a$ , K	$P_{sat}^a$ , kPa	$C_{sat}^a$ , %	$F_c^a$ , cc/min	$F_{total}^a$ , cc/min	$C_{TEOM}^a$ , %
0.8	<b>50.0</b>	<b>49.0</b>	59.5	1.6	0.016	0.8	99.8	<b>0.8</b>
1.6	<b>98.0</b>	<b>0.0</b>	59.5	1.6	0.016	1.6	99.6	<b>1.6</b>

**Cyclohexanone:**

$$F_{total}^d = 100 \text{ cc/min}$$

$$T_{sat}^0 = 59.1 \text{ }^\circ\text{C}$$

$$P_{sat}^0 = 2.91 \text{ kPa}$$

$C_{TEOM}^d$ , %	$F_c^d$ , cc/min	$F_{He,total}^d$ , cc/min	$F_{s-out}^d$ , cc/min	$F_{s-in}^d$ , cc/min	$F_{dil}^d$ , cc/min
1.0	1.0	99.0	33.4	<b>32.5</b>	<b>66.6</b>
1.5	1.5	98.5	51.5	<b>50.0</b>	<b>48.5</b>
2.9	2.9	97.1	100.0	<b>97.1</b>	<b>0.0</b>

$C_{TEOM}^d$ %	$F_{s-in}^s$ , cc/min	$F_{dil}^s$ , cc/min	$T_{sat}^a$ , K	$P_{sat}^a$ , kPa	$C_{sat}^a$ , %	$F_c^a$ , cc/min	$F_{total}^a$ , cc/min	$C_{TEOM}^a$ , %
1.0	32.0	67.0	59.1	2.9	2.9	0.9	99.9	<b>0.9</b>
1.5	50.0	49.0	59.1	2.9	2.9	1.5	100.5	<b>1.5</b>
2.9	97.0	0.0	59.1	2.9	2.9	2.9	99.9	<b>2.9</b>

**Water:**

$$F_{total}^d = 100 \text{ cc/min}$$

$$T_{sat}^0 = 59.2 \text{ }^\circ\text{C}$$

$$P_{sat}^0 = 19.49 \text{ kPa}$$

$C_{TEOM}^d$ , %	$F_c^d$ , cc/min	$F_{He,total}^d$ , cc/min	$F_{s-out}^d$ , cc/min	$F_{s-in}^d$ , cc/min	$F_{dil}^d$ , cc/min
1.0	1.0	99.0	5.0	<b>4.0</b>	<b>95.0</b>
2.0	2.0	98.0	10.4	<b>8.4</b>	<b>89.6</b>
3.2	3.2	96.8	16.6	<b>13.4</b>	<b>83.4</b>
6.0	6.0	94.0	31.2	<b>25.2</b>	<b>68.8</b>

$C_{TEOM}^d$ %	$F_{s-in}^s$ , cc/min	$F_{dil}^s$ , cc/min	$T_{sat}^a$ , $^\circ\text{C}$	$P_{sat}^a$ , kPa	$C_{sat}^a$ , %	$F_c^a$ , cc/min	$F_{total}^a$ , cc/min	$C_{TEOM}^a$ , %
1.0	<b>4.0</b>	<b>95.0</b>	59.0	19.3	19.1	0.9	99.9	<b>0.9</b>
2.0	<b>8.0</b>	<b>90.0</b>	59.0	19.3	19.1	1.9	99.9	<b>1.9</b>
3.2	<b>14.0</b>	<b>83.0</b>	58.9	19.2	19.0	3.3	100.3	<b>3.3</b>
6.0	<b>26.0</b>	<b>68.0</b>	59.2	19.5	19.2	6.2	100.2	<b>6.2</b>

Note that in some cases desired and set flow rates differ by 1-2 points. It is because all desired concentrations were calculated simultaneously as a function of current temperature in the saturator, calculated values changed when temperature changed.

According to Figure 4-10, MFC4 controller was used for carrier gas passing through the saturator, and MFC3 controlled the flow rate of diluent. to reach the highest concentrations of compounds in a gas phase, however, which are equal to saturation concentrations in the

saturation, MFC4 controller could not be used, since the maximum flow rate it could give was 50 cc/min. For this reason, to obtain maximum concentration equivalent to vapor pressure, diluent flow was directed to saturator and MFC3 controller with maximum limit of 500 cc/min was used to control the flow rate.

## APPENDIX E

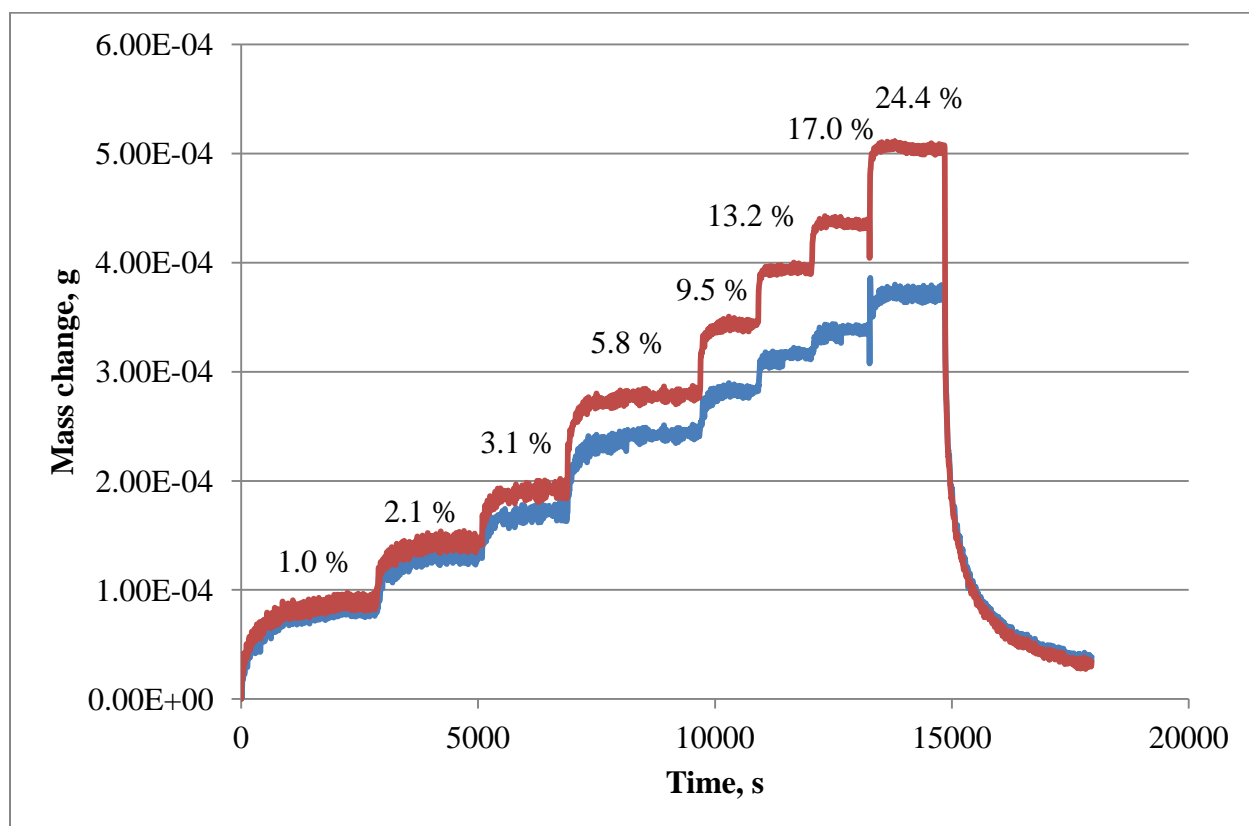


Figure E-1: Example of TEOM raw data obtained for sorption of acetaldehyde on RuCMS800-2 at concentrations 1-24.4 vol. %; red line – original data, blue line – adsorption on quartz is subtracted

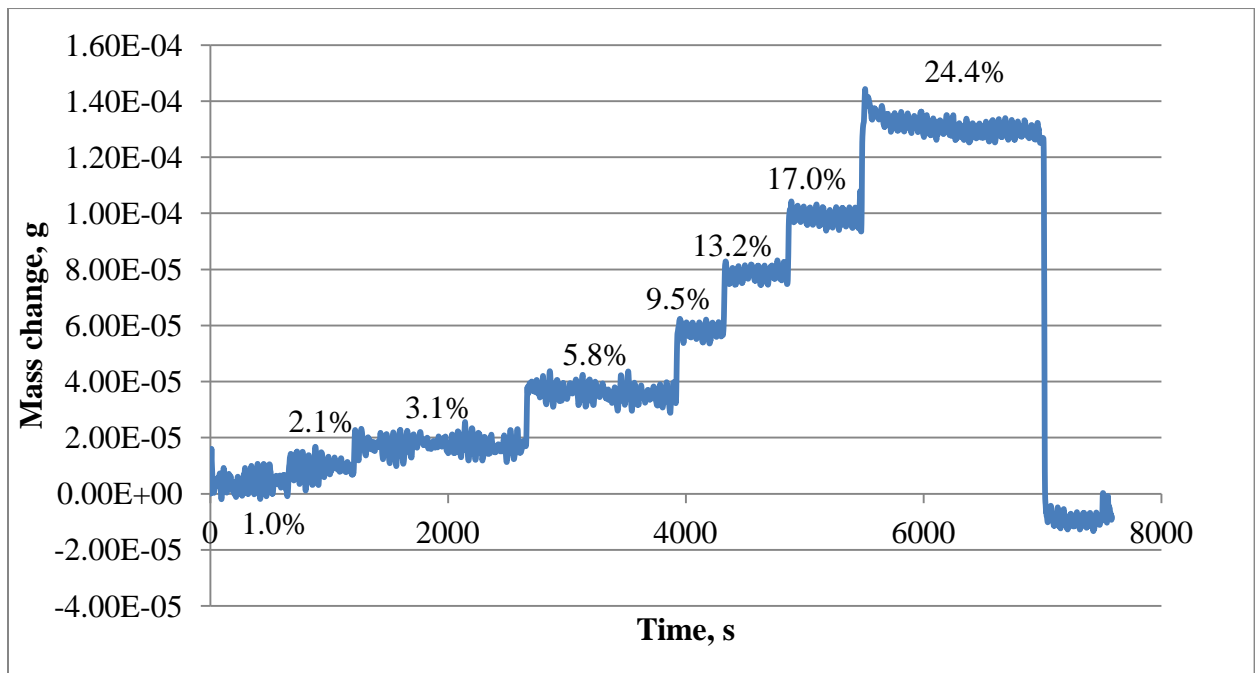
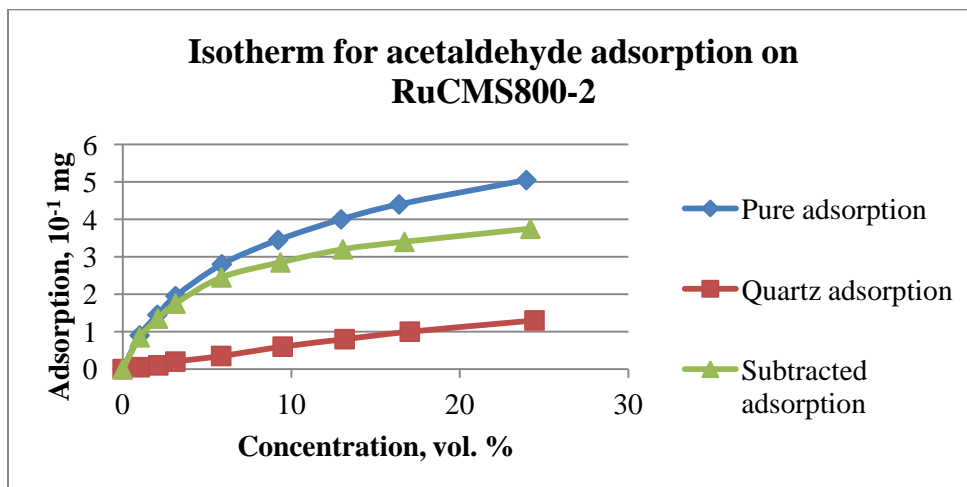
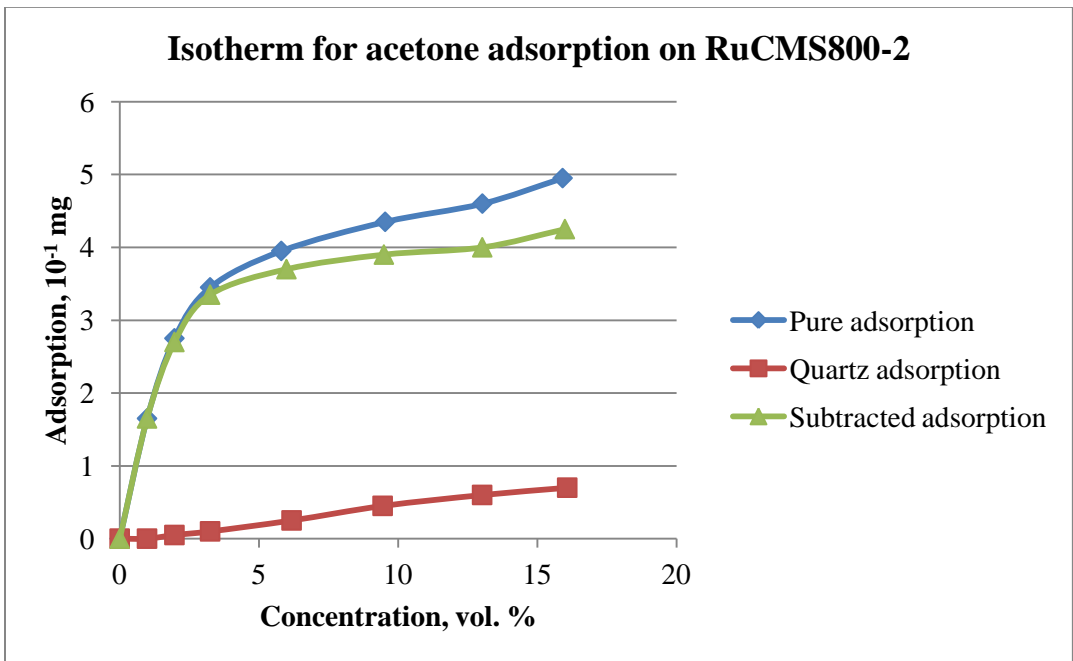
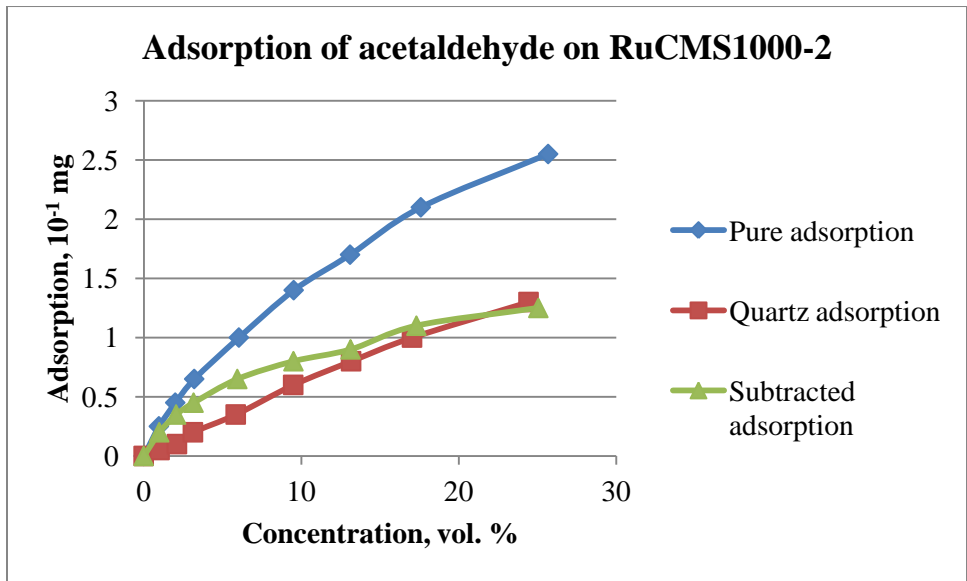
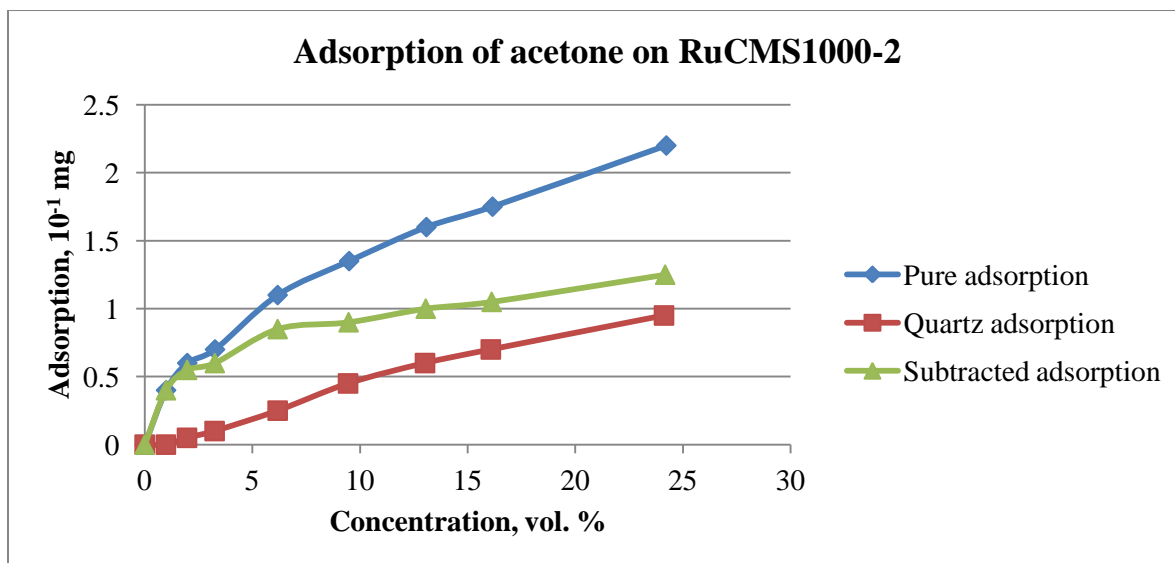


Figure E-2: Example of TEOM raw data obtained for sorption of acetaldehyde on quartz at concentrations 1-24.4 vol. %

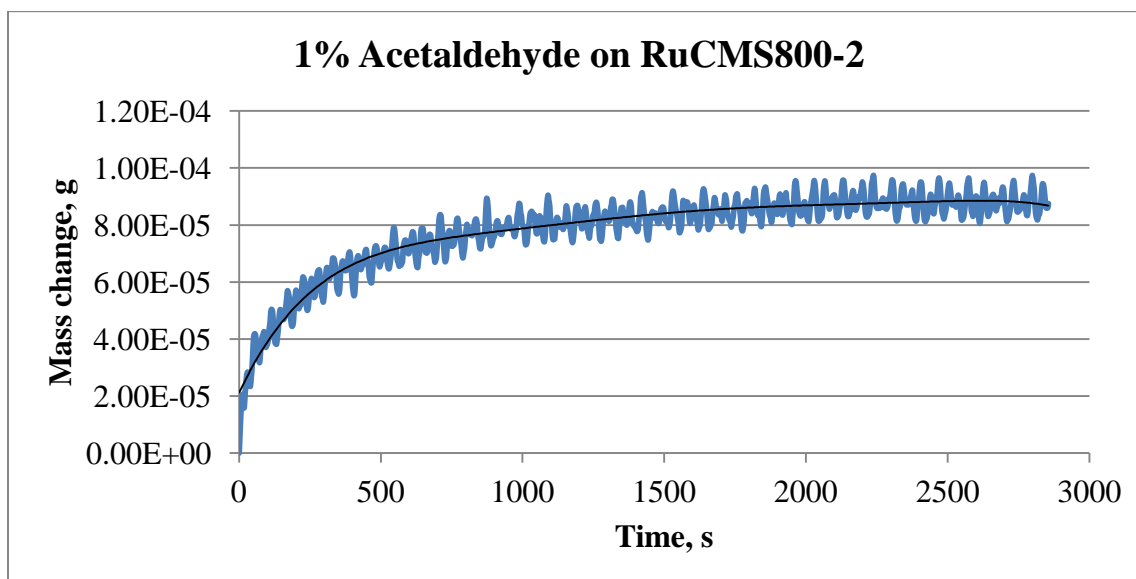
### APPENDIX F



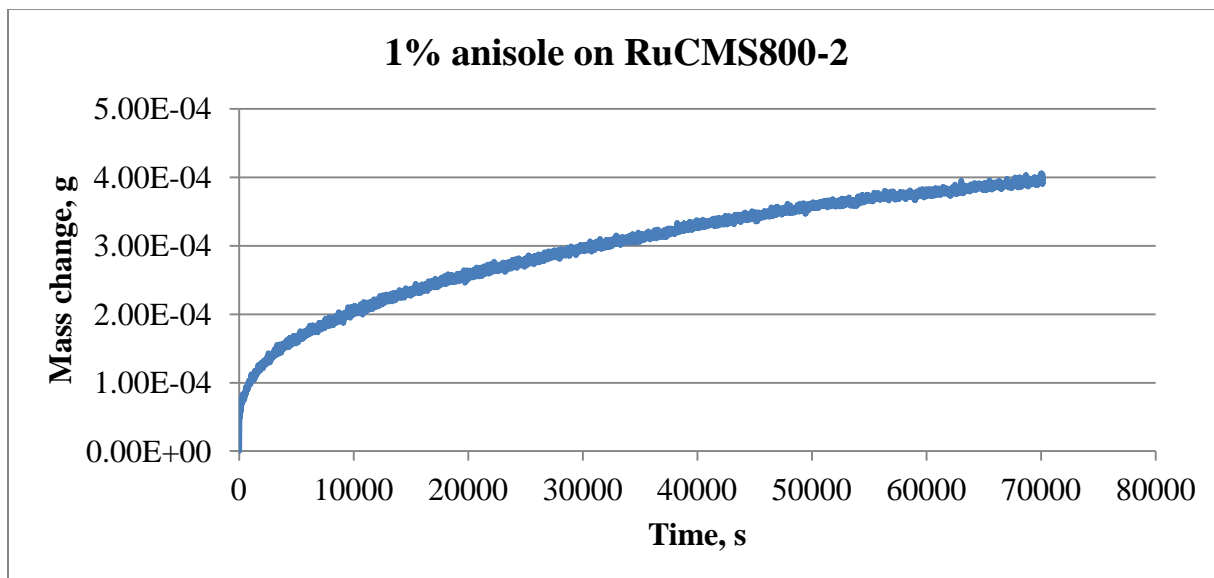
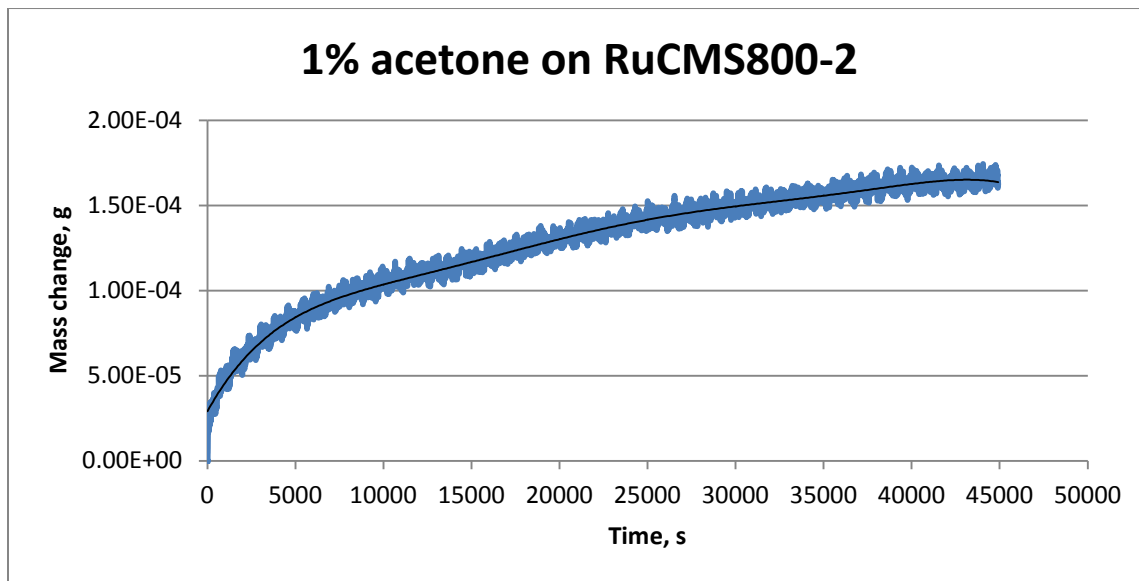


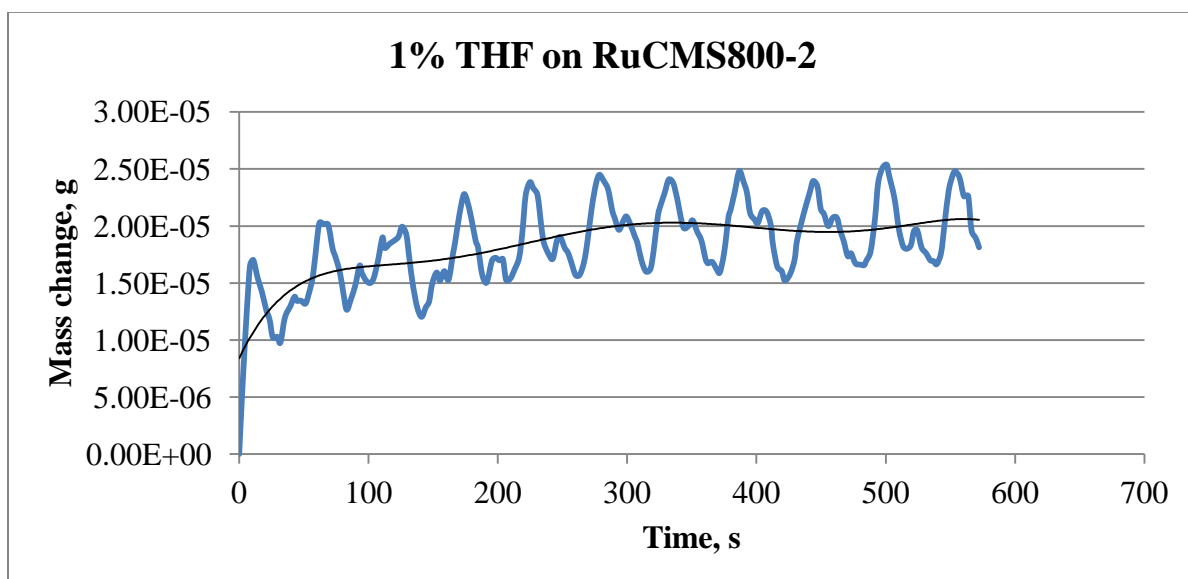
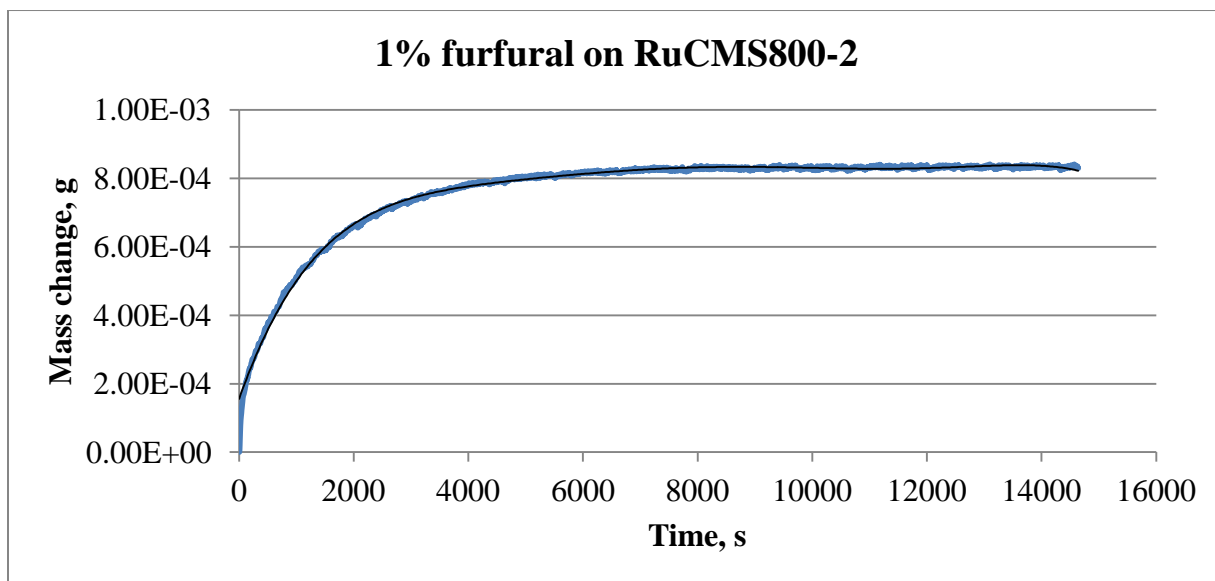


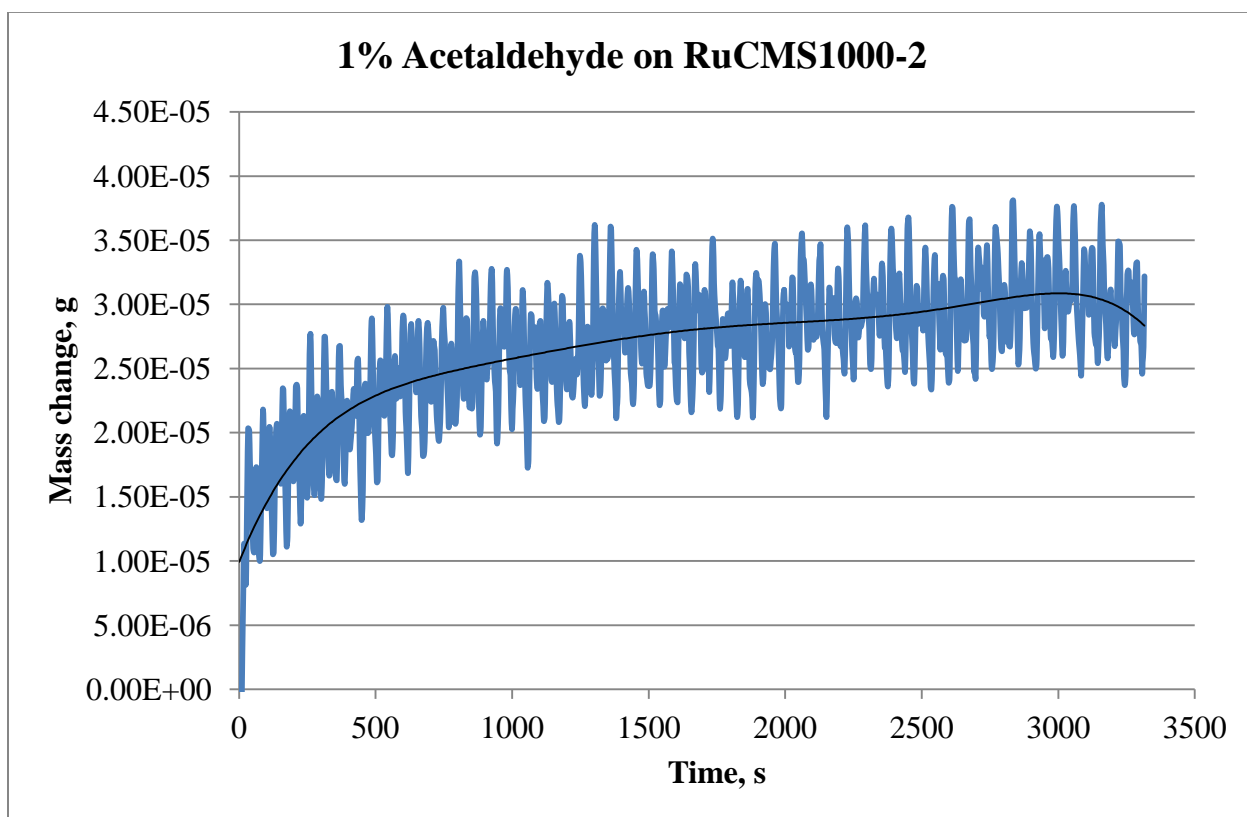
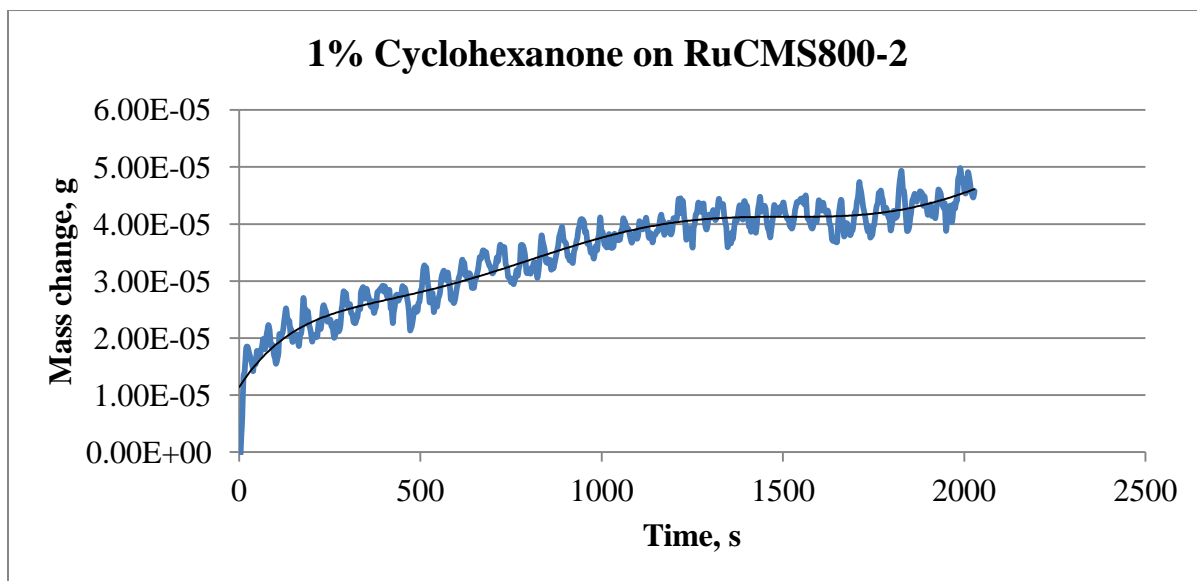
### APPENDIX G

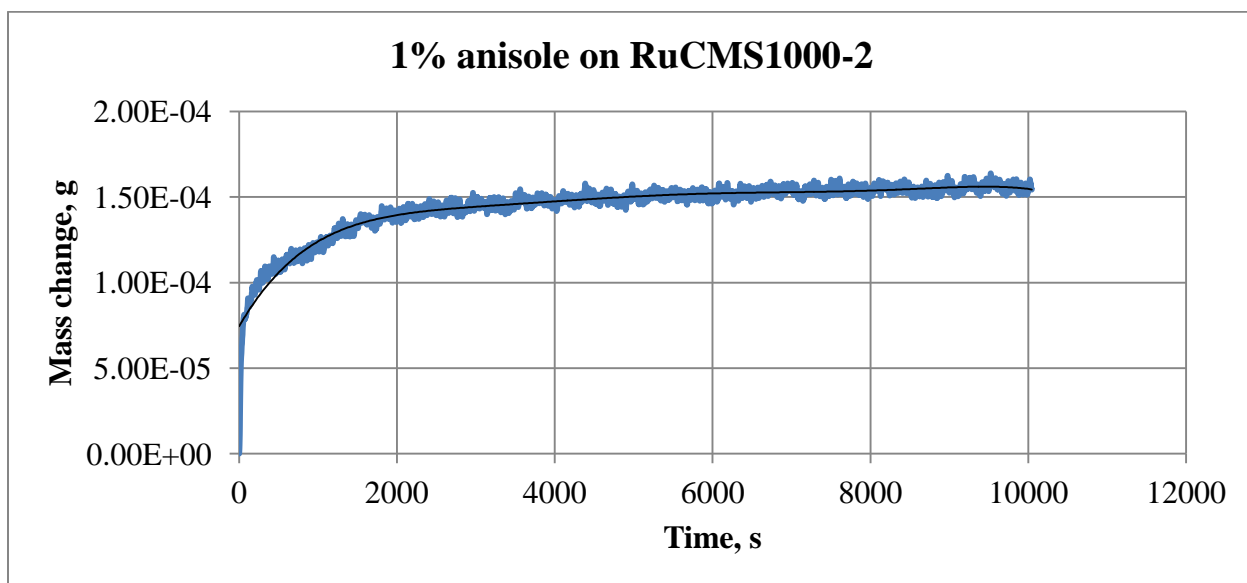
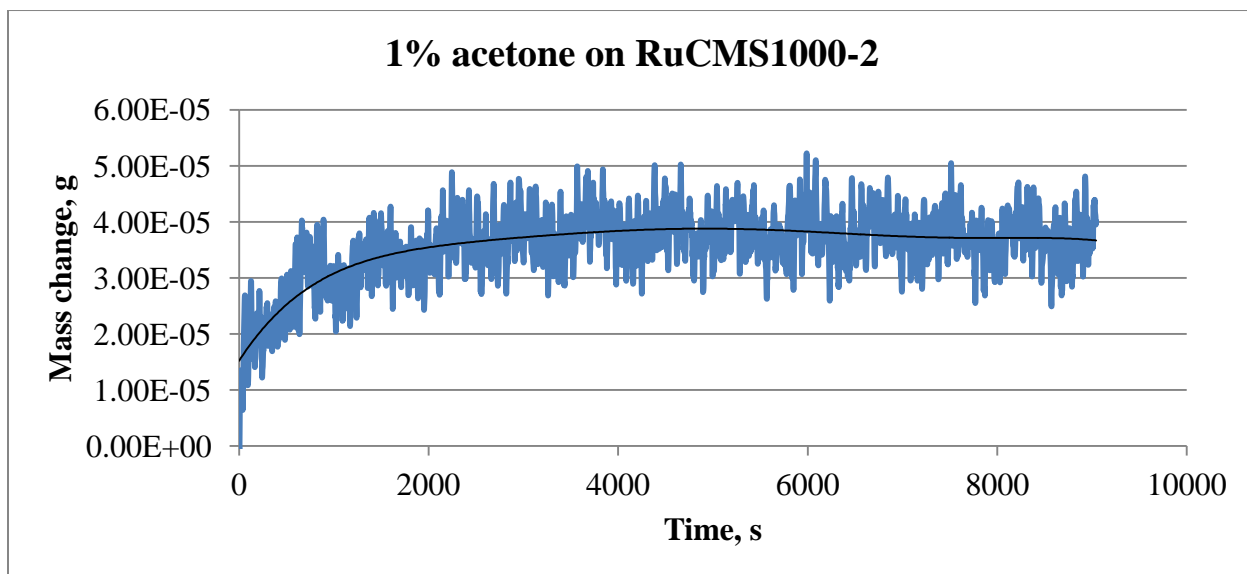


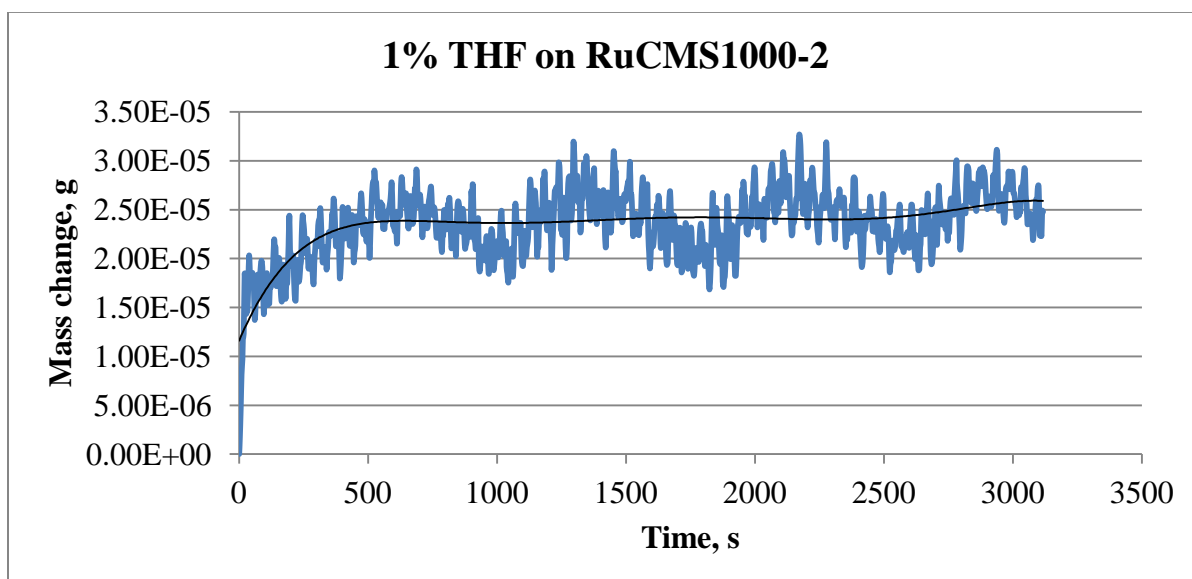
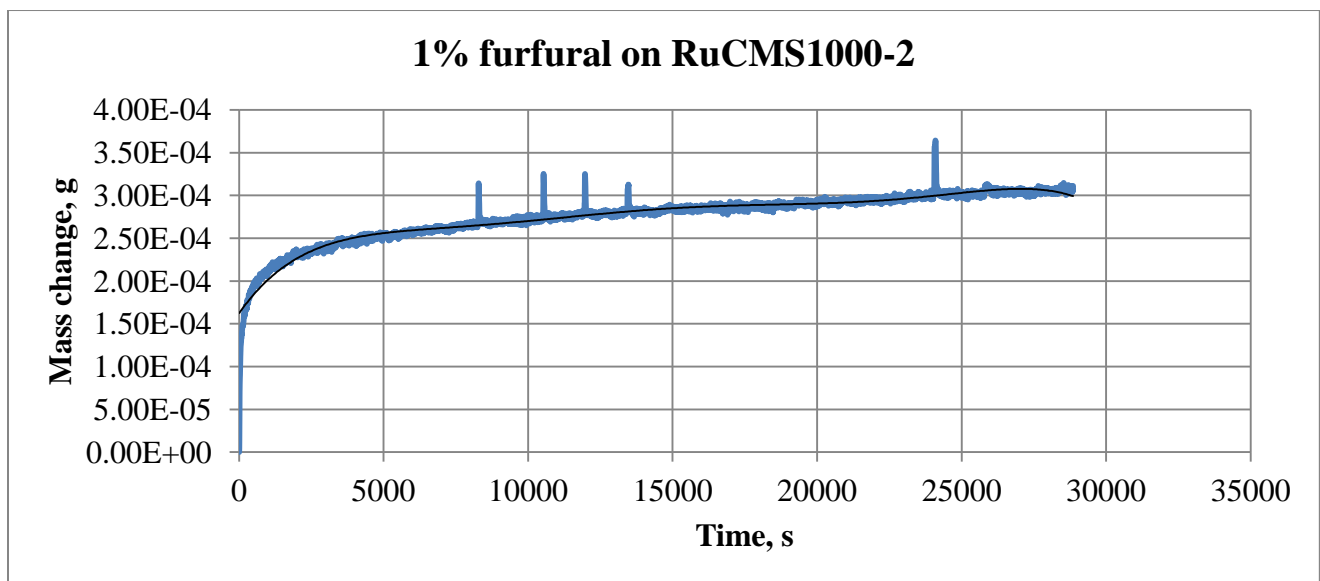


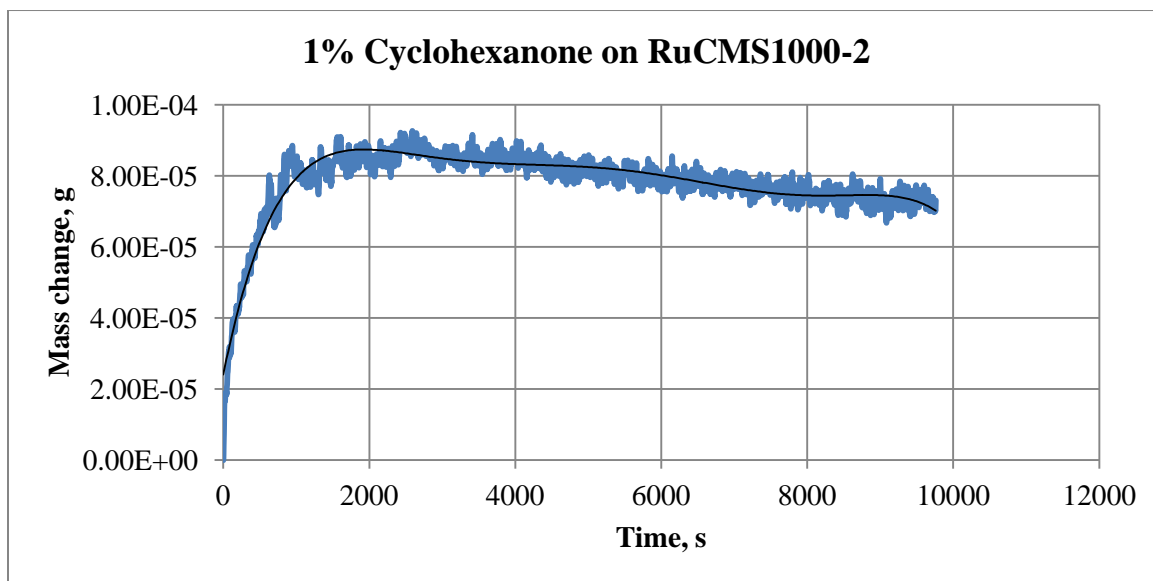












## APPENDIX H

### Sample loadings in TEOM studies, mg

Adsorbate	RuCMS800-2	RuCMS1000-2
Acetaldehyde	6.3	6.5
Acetone	6.4	6.4
Anisole	6.6	6.2
Furfural	6.6	6.6
THF	6.3	6.4
Cyclohexanone	6.8	6.3
Water	6.4	6.4

## APPENDIX I

### ICP Calibration Curve for Ruthenium

